HETEROJUNCTION-ASSISTED IMPACT IONIZATION AND OTHER FREE CARRIER DYNAMICS IN Si, ZnS/Si, AND ZnSe/Si

by

KARL JET MEITZNER

A DISSERTATION

Presented to the Department of Chemistry and Biochemistry
and the Graduate School of the University of Oregon
in partial fulfillment of the requirements
for the degree of
Doctor of Philosophy

June 2015

DISSERTATION APPROVAL PAGE

Student: Karl Jet Meitzner

Title: Heterojunction-Assisted Impact Ionization and Other Free Carrier Dynamics in Si, ZnS/Si, and ZnSe/Si

This dissertation has been accepted and approved in partial fulfillment of the requirements for the Doctor of Philosophy degree in the Department of Chemistry and Biochemistry by:

Mark Lonergan	Chair
Geraldine Richmond	Advisor
Shannon Boettcher	Core Member
Stephen Kevan	Institutional Representative

and

Scott L. Pratt	Dean of the Graduate School

Original approval signatures are on file with the University of Oregon Graduate School.

Degree awarded June 2015.

DISSERTATION ABSTRACT

Karl Jet Meitzner

Doctor of Philosophy

Department of Chemistry and Biochemistry

June 2015

Title: Heterojunction-Assisted Impact Ionization and Other Free Carrier Dynamics in Si, ZnS/Si, and ZnSe/Si

With increasing global energy demand and diminishing fossil fuel supplies, the development of clean and affordable renewable energy technology is more important than ever. Photovoltaic devices harvest the sun's energy to produce electricity and produce very little pollution compared to nonrenewable sources. In order to make these devices affordable, however, technological advances are required.

In this dissertation a novel photovoltaic device architecture that is designed to enhance sunlight-to-electricity conversion efficiency of photovoltaic devices is proposed and demonstrated. The increase in efficiency arises due to enhancement of the internal quantum efficiency of photoexcitation in the semiconductor absorber. In other words, the probability that the absorption of a single photon will produce two or more electron-hole pairs, instead of just one, is increased. This occurs through the process of impact ionization, by which a highly excited charge carrier (via absorption of a high energy photon) relaxes by excitation of a second electron-hole pair. The result is an increased photocurrent, and efficiency, of the photovoltaic device.

Using thin films of ZnS on Si substrates, we demonstrate that the probability of impact ionization is enhanced at the (unbiased) heterojunction between these layers. The magnitude of enhancement depends on material properties, including crystallinity of the ZnS film as well as concentration of oxygen (impurity) at the interface. Thin films of ZnSe on Si substrates do not exhibit heterojunction-assisted impact ionization, but they do display promising characteristics that make them an intriguing system for future work. The same is true for ZnS/Si materials fabricated by O_2-free chemical bath deposition.

For the analysis of plain Si as well as ZnS/Si and ZnSe/Si heterostructures, we employ a novel pump-probe transient transmission and reflection spectroscopy technique. A method is demonstrated for using this technique to quantify internal quantum efficiency as well as interface recombination velocity in each of these materials. In bulk silicon, a free carrier absorption cross section that depends on free carrier concentration (above 10^{18} cm^{-3}) is observed, and the relationship is quantified.

This dissertation includes unpublished and previously published co-authored material.

CURRICULUM VITAE

NAME OF AUTHOR: Karl Jet Meitzner

GRADUATE AND UNDERGRADUATE SCHOOLS ATTENDED:

University of Oregon, Eugene
University of Wisconsin, Eau Claire

DEGREES AWARDED:

Doctor of Philosophy in Chemistry, 2015, University of Oregon
Master of Science, 2012, University of Oregon
Bachelor of Science in Chemistry, 2010, University of Wisconsin – Eau Claire

AREAS OF SPECIAL INTEREST:

Semiconductor Processing and Device Physics
Photovoltaics
Lasers and Optical Systems

PUBLICATIONS:

Meitzner, K. J., Tillotson, B. M., Siedschlag, A. T., Moore, F. G., Kevan, Stephen D., Richmond, G. L. Morphology and Growth Behavior of O_2-free Chemical Bath Deposited ZnS Thin Films. Submitted to Thin Solid Films, first review.

Bartholow, T. G., Sanford, B. L., Cao, B., Schmit, H. L., Johnson, J. M., Meitzner, K. J., Bhattacharyya, S., Musier-Forsyth, K., Hati, S. (2014). Strictly Conserved Lysine of Prolyl-tRNA Synthetase Editing Domain Facilitates Binding and Positioning of Misacylated tRNAPro. Biochemistry **53**(6): 1059-1068.

Meitzner, K. J., Moore, F. G., Tillotson, B. M., Kevan, Stephen D., and Richmond, G. L. (2013). Time-resolved measurement of free carrier absorption, diffusivity, and internal quantum efficiency in silicon. Applied Physics Letters **103**(9): 092101.

Miller, D. W., Hugger, P., Meitzner, K. J., Warren, C. W., Rockett, A., Kevan S. D., Cohen, J. D. (2013). A contactless photoconductance technique for the identification of impact ionization. Photovoltaic Specialists Conference (PVSC), 2013 IEEE 39th.

ACKNOWLEDGEMENTS

I owe a great deal of thanks to all the people who’ve helped get me to graduate school as well as those who’ve made my time here productive and fun. First and foremost, I’d like to thank Professor Geri Richmond for the opportunity to be here and perform this research. She delivers mentorship with warmth and kindness, and truly cares about the success of her graduate students. I’d like to thank my fellow graduate students (and postdocs) in the Richmond lab – Laura, Brandon, Andrew, Pat, Regina, Bri, Sumi, Nick, Jenny, Clive, and many past members – for creating a fun, dynamic, collaborative environment to work in. Special thanks to Pat Blower for teaching me most of what I know about laser systems, and to Larry Scatena for teaching me the rest. Thanks to Mark Lonergan for being an amazing teacher and fostering my interest and curiosity in the topics explored in this dissertation. Thanks to Shannon Boettcher for initiating my graduate school experience and teaching me what it’s like to be a graduate student in chemistry. Thanks to Stephen Kevan for unwavering guidance through these scientific endeavors.

This work would not be what it is without Dr. Frederick Moore, who was an integral part of my entire graduate school experience. Fred’s mentorship not only drove this research forward, but taught me how to think and act like a scientist. The influences of our conversations and his other contributions permeate every page of this dissertation.

Thanks to my near and extended family, for being always supportive and helping me find this challenging and rewarding path. To my parents, Louise and Karl Meitzner, and sister, Sunshine Meitzner, thank you for being always there making me feel that I’m never alone.

Others that have helped me get here include my high school chemistry/physics teacher, Joanne Zosel, who first made chemistry interesting and fun. My organic and inorganic professors in college, Dr. David Lewis and Dr. Jason Halfen, furthered my interest in chemistry and are a big part of why I'm here. Sanchita Hati taught me to do research as an undergraduate, and encouraged me to come to graduate school.

Finally, I'd like to thank all of the friends that I haven't yet mentioned. To the crew in Bend – Alex, Pat, Aaron, and Jackie – thanks for giving me a weekend/holiday destination for some high-quality rest and relaxation. Thanks to my friend and golfing buddy, Bryan Nell, for persevering with me through the enraging yet fulfilling experiences of weekend golf. Thanks to Matt Hammers and the numerous others, including my lab-mates, who've made life in Eugene great.

I'm thankful to these people and experiences because they've led me not only to graduate school, but also to my amazing girlfriend Mary Collins. Every experience in the last 4 years has been brightened by her presence.

TABLE OF CONTENTS

APPENDICES

LIST OF FIGURES

Figure Page

Figure Page

LIST OF TABLES

CHAPTER I

INTRODUCTION

Background

The way we adapt, in the next 50-100 years, to increasing energy demands concurrent with diminishing fossil fuel supplies will impact the global climate, pollution levels, and energy security of our future. Though each of these challenges requires attention, a synergistic solution with primary focus on climate-control policies could be most effective [1, 2].

Central to climate-control policies is the reduction of electricity derived from fossil fuels, with a corresponding increase in production by renewable energy sources. This would result in decarbonization, or a decrease in carbon-containing greenhouse gas emissions, which is necessary to mitigate the increase in mean global surface temperature [3, 4]. It would also decrease air pollution and reduce pollution-related health problems worldwide [5]. Additionally it would result in a higher percentage of domestically derived energy and in higher diversity of energy sources, which would improve energy security [6]. Though implementation of technologies with reduced carbon emissions would be expensive, projections show that the cost of doing so would be largely offset by a corresponding reduction in costs that would otherwise be associated with independently reducing pollution levels and increasing energy security [1].

Photovoltaic devices (PVs) provide a source of renewable energy, and have the potential to fulfill our global energy demands in the future. The purpose of PVs is in principle similar to photosynthesis in plants: absorb sunlight and convert it into a useful form of energy. While plants store this energy in the chemical bonds of sugar molecules, PVs produce direct current electricity. Thus we have, in principle, a renewable energy technology that can produce electricity for as long as the sun shines.

The sunlight striking the surface of the Earth in one hour contains enough energy to supply our global energy demands for an entire year [7]. Though an unrealistic scenario, statistics like this have motivated many theoretical and experimental studies regarding the potential of PVs to support our energy demands in the future. Assuming a PV panel efficiency of 14.3% and 5 hours/day of direct sunlight (1000 W/m^2), a PV area of 158 mi x 158 mi would be sufficient to meet the global electricity demand (using 2004 statistics) [8]. Even small increases in cell efficiency (many of which have already been made since 2004) dramatically reduce this area requirement and make it a feasible future scenario. Taking into account the economic and regulatory environment in 2013, the European Photovoltaic Industry Association predicted that 10 – 15% of the electricity demand of the European Union would be supplied by PVs by 2030 [9].

PV technology provides many advantages over fossil fuels for energy production. PVs are responsible for 10x fewer greenhouse gas emissions, per kWh of energy produced, than fossil fuels [10]. Thus, from climate-control and pollution mitigation standpoints, they are a very attractive alternative. They are also portable, allowing them to be placed around the globe and provide electricity locally. Indeed, their portability has provided them unique applications as early as the 1950s, when they were used primarily on telecommunication satellites. Throughout the mid-1900s, low efficiency and high cost of manufacturing limited PVs to applications in secluded locations where other energy sources were unavailable, such as satellites, buoy lights, telephone and microwave repeater stations, and water pumps in developing countries. More recently, increased efficiency and lower manufacturing costs have encouraged their use in community settings, but further progress is necessary.

In order to achieve a higher efficiency-to-cost ratio, innovative technologies that increase efficiency and/or reduce manufacturing costs are required. Due to the high material cost of silicon (up to 60% of the cost of a finished solar cell), thin film solar cells (so-called 2nd generation PVs) have the potential to significantly reduce material costs [11]. Alternatively, methods of increasing the efficiency of current PV technologies could increase the efficiency-to-cost ratio without requiring a new manufacturing infrastructure.

The design of high-efficiency PV device technology requires understanding of free carrier dynamics on an ultrafast time-scale. In Si solar cells, which occupy over 80% of the global PV market, about 47% of incident power is lost as heat subsequent to absorption of photons with energy greater than the bandgap ($E_{hv} > E_g$) [11, 12]. These photons produce electron-hole pairs with excess energy ("hot" carriers) $E_{hv} - E_g = E_x$ which is typically dissipated to the lattice via phonon scattering (heat production) within a few hundred femtoseconds [13, 14]. Alternatively, if the excess energy E_x is equal to or greater than the bandgap energy, carrier-carrier scattering can generate a second electron-hole pair by impact ionization (II) [15]. While II occurs to a small extent in bulk Si, it only contributes, at most, 0.5% to the efficiency of a silicon solar cell [16]. In this dissertation we propose and demonstrate a method for increasing the probability of II, which could in turn enhance the efficiency of a PV device.

Scope and Approach

In this dissertation we propose and demonstrate a photovoltaic device architecture that is simple in design and can, in principle, be applied to many existing PV technologies to increase their efficiencies. For example, when applied to a silicon solar cell, the maximum theoretical efficiency increases from 31% to 42% [17, 18] . The increase arises due to enhancement of the internal quantum efficiency (IQE) of photocarrier generation in the PV absorber. In other words, the probability that the absorption of a single photon will produce two or more electron-hole pairs, instead of just one, is increased. This occurs through the process of impact ionization, whereby one photogenerated charge carrier (either electron or hole) releases its excess energy by excitation of a second electron-hole pair [15, 19]. The result is an increased photocurrent, and thus an increased efficiency, for the PV device.

The principles of our approach are presented in Figure 1. The system consists of a nanostructure (in this case a thin film) of a large bandgap semiconductor (called the harvester), and a lower bandgap bulk PV material (called the host), which in this case is Si. The process is as follows: (1) incident photons with sufficient energy are absorbed and produce an electron-hole pair in the harvester, (2) due to a built-in electric field, the electron (or hole) is swept into the host and traverses a band discontinuity at the harvester/host interface, and (3) the energy gained from traversing the band discontinuity (ΔE_{CB}) enhances the probability that impact ionization will occur, thus producing an

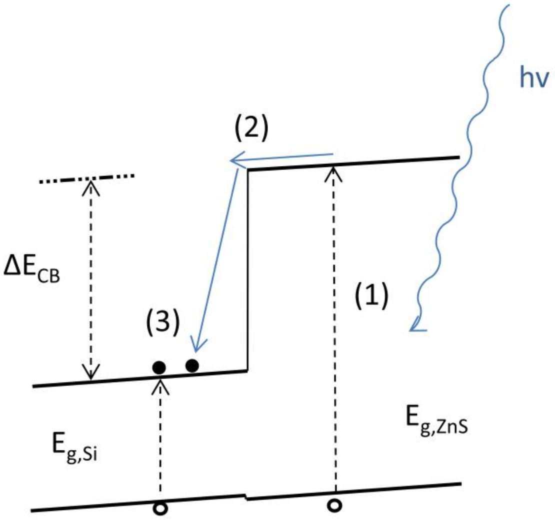

Figure 1. Principles of operation. A high energy photon is absorbed in the harvester (1), where it excites one electron-hole pair. The electron moves into the host (2) and excites an additional electron-hole pair by impact ionization (3).

additional electron-hole pair. The demonstration of this process, which we refer to as heterojunction-assisted impact ionization (HAII), has been the objective motivating the work presented in this dissertation.

The investigations presented herein focus on characterization of the electronic properties of various semiconductor materials that were expected to exhibit HAII. For this purpose we have designed and implemented an innovative pump-probe transient transmission/reflection laser technique which is capable of quantifying free carrier absorption, recombination, and IQE in semiconductor materials, including heterostructures. Theoretical aspects and experimental considerations of this technique are presented in Chapter II, which includes co-authored material with Frederick G. Moore, Brock M. Tillotson, Stephen D. Kevan, and Geraldine L. Richmond.

The materials investigated are thin films of ZnS or ZnSe on silicon substrates. These materials are well-studied, with a wide variety of existing applications, and are ideal candidates for this work due to their interfacial electronic properties when deposited on silicon. Some details of the synthesis and structural characterization of these materials are presented in Chapter III, which includes material that will be published with co-authors Christopher Reidy, Stephen D. Kevan, and Geraldine L. Richmond. Before discussing the electronic properties of these heterostructures in Chapter V, we present an analysis of plain silicon in Chapter IV, which includes previously published material with co-authors Frederick G. Moore, Brock M. Tillotson, Stephen D. Kevan, and Geraldine L. Richmond. There, we demonstrate the utility of the transient absorption/reflection laser technique, as well as characterize some novel aspects of free carrier absorption and IQE in silicon. Of particular note is our quantification of free carrier absorption cross section as a function of photogenerated carrier concentration. These studies provide a foundation for the following analysis of ZnS/Si and ZnSe/Si materials in Chapter V, which includes material that will be published with co-authors Christopher Reidy, Stephen D. Kevan, and Geraldine L. Richmond.

The majority of thin films in this study have been deposited using methods which evaporate the thin-film material onto the substrate in a high-vacuum atmosphere. These methods allow a high degree of control over the deposition conditions and produce high quality films, but are energy intensive due to high temperatures and vacuum conditions. Therefore we describe, in Chapter VI, the deposition of ZnS thin films onto silicon substrates using the O_2-free chemical bath deposition (OFCBD) method. This method is attractive due to low energy requirements (occurring near room temperature and atmospheric pressure) and simplicity of the experimental setup. Moreover, it is capable of coating large surface areas with optically smooth thin films [20] of high crystallinity.

Some material in this chapter will be published with co-authors Frederick G. Moore, Brock M. Tillotson, Amanda Siedschlag, Stephen D. Kevan, and Geraldine L. Richmond.

CHAPTER II

PUMP-PROBE TRANSIENT TRANSMISSION & REFLECTION SPECTROSCOPY: THEORETICAL AND EXPERIMENTAL CONSIDERATIONS

The principles and experimental considerations of pump-probe transient transmission & reflection spectroscopy are presented in this chapter. Though transient transmission and reflection spectroscopies are individually well-known in the literature, the combination of these methods and accompanying models and analysis were designed specifically for the analysis of heterojunction semiconductor material systems exhibiting HAII. Thus, the chapter begins with a discussion of the principles of operation of this technique. The method of data analysis is then described. Finally, the experimental setup is described including specifications of the laser system and a schematic of the sample area. Frederick G. Moore was an invaluable collaborator throughout the development of this technique. This chapter includes previously published material with co-authors Brock M. Tillotson, Frederick G. Moore, Stephen D. Kevan, and Geraldine L. Richmond.

Theoretical Considerations

In general, pump-probe transient transmission and/or reflection techniques allow the experimenter to monitor free carrier dynamics in a semiconductor of interest. Compared to other techniques (e.g. photoconductivity, two-photon photoemission, photoluminescence), pump-probe is most attractive due to pulse-width limited time resolution (in this case 100-200 fs), ease of control over carrier injection level, and access to both bulk and surface phenomena [21-24]. Characterization of free carrier dynamics (e.g. impact ionization, diffusion velocity, absorption cross section, surface and/or bulk recombination lifetime) gives valuable information about the semiconductor that can be used to optimize device parameters and performance. In this work we have been interested in promoting impact ionization at semiconductor heterojunctions while minimizing interfacial recombination. Thus, the experimental technique was designed specifically to monitor the probability of free carrier impact ionization as well as recombination rates in both single- and multi-component semiconductors for photovoltaic applications. We have also quantified the free carrier absorption cross section (σ_{FCA}) as a function of photogenerated free carrier concentration in silicon.

The principle of operation of the ultrafast pump-probe transient transmission and reflection spectroscopy technique is as follows. Free carriers are generated by an optical pulse, called the pump pulse, which has photon energy greater than the semiconductor bandgap energy. This pulse is absorbed in the semiconductor and promotes electrons from the valence band into the conduction band (i.e. creates electron-hole pairs) with a concentration profile that is highest at the front surface and decays exponentially moving into the material. The penetration depth of this light into the semiconductor is described by the absorption coefficient, α, which depends on photon energy as well as the band structure of the semiconductor. Once promoted into the conduction band, the electron as well as the hole is referred to as a free carrier, because it is effectively unbound by Coulomb attraction and therefore free to diffuse and/or drift in the semiconductor. A second pulse with photon energy smaller than the semiconductor bandgap energy, called the probe pulse, arrives after some time delay (Δt) relative to the pump pulse, and is both reflected off and transmitted through the semiconductor. As described below, we measure both the reflectivity and transmission of this probe pulse in order to quantify the free carrier absorption of the transmitted portion.

The method employed is a combination of transient transmission and reflection spectroscopy techniques that, when combined (performed simultaneously), allow an accurate quantification of free carrier absorption. This is in contrast to many similar techniques reported in the literature, where either transmission or reflection spectroscopy is performed in isolation. In the following two paragraphs, the principles of operation, strengths, and limitations of these two techniques are discussed. Following this discussion, the advantages of performing them simultaneously become apparent.

A pump-probe transient reflectivity experiment probes free carriers that are within a distance *d* of the surface ($d=\lambda/4\pi|n|$, where λ is the wavelength of reflected light and n is the complex index of refraction) by monitoring the free-carrier-induced change in reflectivity of a probe beam [13]. The presence of free carriers affects the refractive index (n) of the semiconductor, as described by the Drude model [25]

$$\Delta n = -\frac{Ne^2}{2\varepsilon_0 n_b m^* \omega^2} \tag{1}$$

where N is the injected carrier density, e is the elementary charge, ε_0 is the initial dielectric constant, $n_b = \sqrt{\varepsilon_b/\varepsilon_0}$ is the background dielectric constant, m* is the effective carrier mass, and ω is the angular optical frequency. It follows that photoexcitation results in an increase in N and a corresponding decrease in n. The relationship between n and reflectance (R) is given by the Fresnel Equations

$$r_{\parallel} = \frac{n_t cos\theta_i - n_i cos\theta_t}{n_i cos\theta_t + n_t cos\theta_i} \tag{2}$$

$$r_{\perp} = \frac{n_i cos\theta_i - n_t cos\theta_t}{n_i cos\theta_i + n_t cos\theta_t} \tag{3}$$

and the relationships

$$R_{\parallel} = r_{\parallel}^2 \tag{4}$$

$$R_{\perp} = r_{\perp}^2 \tag{5}$$

where $r_{\parallel}$ and $r_{\perp}$ are the amplitude reflection coefficients for parallel and perpendicularly polarized light, respectively, and the subscripts *i* and *t* refer to incident and transmitted [26]. In the experiments presented in this dissertation, the angles of incidence and transmission are such that the decrease in n corresponds to a decrease in R. In addition to learning about the free carrier concentration in the near-surface region, these experiments can also be used to monitor carrier dynamics such as ultrafast cooling [13], surface recombination [27], and diffusion rates [28].

A pump-probe transient transmission experiment typically quantifies the free carrier absorption of a probe beam in order to monitor the free carrier concentration within a semiconductor. The absorption of light by free carriers is described by the Drude model [25]

$$\alpha_{FC} = \frac{Ne^2}{\varepsilon_0 n_b m^* \omega^2 \tau c} \tag{6}$$

where τ is the carrier momentum relaxation time and the subscript FC refers to free carriers. It follows that free carrier absorption increases with increasing carrier concentration and decreasing frequency of light. Light with photon energy lower than the semiconductor bandgap is typically used so that the measured absorption by free carriers (intraband absorption) is not convoluted by interband absorption. In addition to monitoring free carrier concentration, this technique can also be used to monitor carrier dynamics including diffusion [29, 30], surface recombination [31], and bulk recombination [24].

Performing these techniques in parallel offers many advantages. First, by monitoring free carrier absorption, one probes free carrier dynamics through the full depth of the sample. Measuring reflectivity simultaneously, free carrier dynamics in the near-surface region can be de-coupled from those in the bulk. Second, FCA cannot be accurately calculated by measuring transmission alone. Because the reflectivity of the sample changes upon photoexcitation, the amount of light transmitted into and through the sample changes as well. Failing to take this into account, the measured FCA would be lower than the true value (for a decrease in R), and the calculated FCC would be too low as well. This is especially important to consider when using excitation wavelengths with photon energies significantly higher than the semiconductor bandgap energy, because in general the absorption coefficient of light increases with increasing photon energy. This means that for high photon energies a significant portion of the free carriers are generated near to the front surface, and the change in reflectivity is significant relative to the amount of free carrier absorption. This is indeed the scenario in this work, and thus we measure both reflectivity and transmission in order to accurately quantify free carrier absorption.

The first step in learning about free carrier dynamics is calculating the free carrier concentration (FCC) from the experimentally measured free carrier absorption. The quantity of free carrier absorption of the probe pulse is given by $I_{FCA} = -\Delta R - \Delta T$, where $\Delta R = R_{pumped} - R_{unpumped}$, $\Delta T = T_{pumped} - T_{unpumped}$, and the subscripts *pumped* and *unpumped* refer to whether or not the sample has been perturbed by a pump pulse. In calculating FCC from measurements of ΔR and ΔT, the figure of interest is $\frac{I_o}{I_o - I_{FCA}}$ where I_o is the transmitted probe pulse energy in the absence of a pump pulse (baseline signal). This quantity is inserted into the Beer-Lambert relationship to calculate the free carrier sheet concentration (FCSC)

$$N_{\square} = \frac{\ln\left(\frac{I_o}{I_o - I_{FCA}}\right)}{\sigma_{FCA}} \qquad (7)$$

where σ_{FCA} is the free carrier absorption cross section. $N_{\square}$ represents the number of free carriers per unit area of the substrate surface, and is equal to the volume carrier concentration (N) integrated though the depth of the sample

$$N_{\square} = \int_0^x N(x)dx. \qquad (8)$$

This analysis provides a spectrum of FSCS versus probe delay time (Δt), which undergoes further analysis as described in future chapters.

Experimental Setup

A schematic of the experimental setup is shown in Figure 2. Pulses are generated by a mode-locked Ti:Sapphire laser (Spectra-Physics Tsunami) pumped by a continuous-wave Nd:YVO_4 laser (Spectra-Physics Millennia Prime) at 532 nm. The resultant 800 nm, 800 mW, 80 MHz pulses then seed a Ti:Sapphire amplifier (Spectra-Physics Spitfire Pro XP) pumped by a 527 nm pulsed Nd:YLF laser (Spectra-Physics Empower) to produce ~110 fs, 800 nm pulses at 1 kHz. From the output of 3 W, two portions of 800 mW are split off and used for pump and probe beams. The 800 mW probe beam is directed to an optical parametric amplifier (OPA) where a BBO crystal provides tunability from 1150-1550 nm. It then travels a variable path length which provides up to 3.5ns of delay time, relative to the pump pulse, in 8.7 fs steps. Both the transmission and reflection of the probe pulses are normalized using a probe reference detector (D4) to increase the signal to noise ratio. The 800 mW pump beam is directed to an OPA that provides continuous tunability between 300 nm and 800 nm. This beam can also undergo third harmonic generation (THG) to produce 267 nm pulses. Before reaching the sample, the pump beam is chopped to 500 Hz, which is half the pulse frequency of the probe beam. A portion of each pump pulse is collected by detector D3 (Thorlabs DET210) and used for excitation energy normalization.

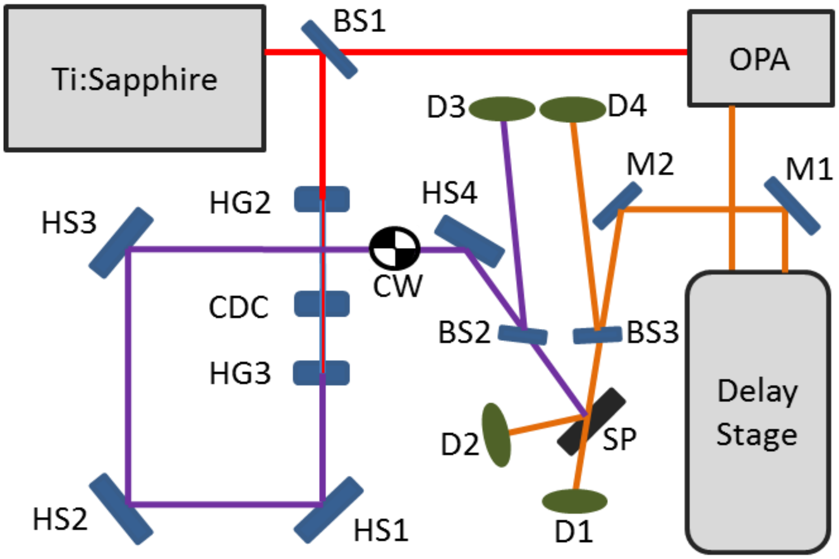

Figure 2. Experimental setup. The rectangle labeled Ti:Sapphire includes the laser systems that produce the fundamental 800 nm, 110 fs pulses at 1 kHz. BS beam splitter; OPA optical parametric amplifier; HG2 2nd harmonic generation BBO crystal; HG3 3rd harmonic generation BBO crystal; CDC calcite delay compensator; HS harmonic separator; M mirror; D detector; SP sample; CW chopper wheel.

A schematic of the sample area is shown in Figure 3. The sample in these studies consists of either a silicon wafer or a silicon substrate with ZnS or ZnSe film. It is held in a rotating mount, at an angle of 57° to the probe beam, which is near the Brewster angle (of silicon) to minimize internal reflections. The transmission, reflection, and probe reference signals are collected by InGaAs amplified photodetectors (Thorlabs DET10C). The photodetector outputs are quantified by Stanford Instruments SR250 Gated Integrators, which transmit the signals to a computer running LabVIEW.

The pump and probe beams are overlapped at the sample position. In some of the following analyses, it is necessary to have an effectively constant FCSC across the probed region. To accomplish this, the probe beam is focused to a size significantly smaller than that of the pump beam. Therefore, the probe beam overlaps with only the

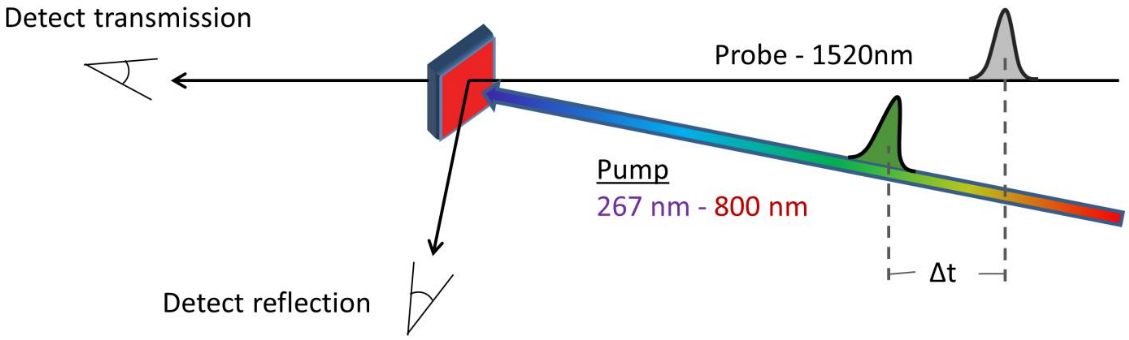

Figure 3. Schematic of the pump and probe beams in the sample area. The pump beam is continuously tunable from 300 to 800 nm (267 nm is also attainable through THG of 800 nm). Both the reflection and transmission of the 1520 nm probe beam are collected.

center of the pump beam, where the energy distribution can be approximated as constant. In these studies, the Gaussian beam width of the pump beam was always at least 7x larger than that of the probe beam.

CHAPTER III

SAMPLE PREPARATION AND CHARACTERIZATION

The fabrication and characterization of sample materials is presented in this chapter. First, the identity and preparation of silicon samples is presented. These samples are the substrate material for ZnS and ZnSe films (analyzed in Chapter V), and are analyzed in Chapter V. The ZnS samples studied in Chapter V were all deposited by pulsed laser deposition (PLD). Thus, we review the principle of operation of PLD, and provide some characterization of the samples. ZnSe samples were deposited with a proprietary technique, and therefore the preparation and characterization of these samples will be presented with limited detail. ZnS/Si and ZnSe/Si samples were fabricated and characterized by collaborators at Oregon State University (Christopher Reidy, in Dr. Janet Tate's lab group) and nLIGHT corporation (Jason Patterson and Reuven Ballaban), respectively. This chapter includes material that will be published with co-authors Frederick G. Moore, Christopher F. Reidy, Stephen D. Kevan, and Geraldine L. Richmond.

Si Samples

The silicon samples used in this study are double-side polished, FZ-grown <100> or <111> Si wafers of high purity (undoped, $R > 5000\Omega cm$). To prepare the wafers for analysis, they were (1) cut to an appropriate size, (2) cleaned of organic and metal contaminants, (3) stripped of the oxide layer, (4) cleaned of ionic contaminants, and (5) oxidized to passivate the Si surface with SiO_2.

The silicon wafers were first cut, using a diamond scribe, to sizes of approximately 1.5 cm^2. Residual Si particulates from the cutting process were removed by ultra-sonication in ultrapure H_2O. They were then subjected to the RCA standard cleaning solutions 1 and 2, and an HF etching solution, all of which are designed to remove contaminants. The first cleaning solution is known as RCA standard clean 1 (SC-1) and is a mixture of H_2O, H_2O_2, and NH_4OH in a volume ratio of 5:1:1. This solution is designed to remove organic contamination by oxidative breakdown and dissolution. It is also effective to remove a variety of metals including group IB and IIB metals as well as gold, silver, copper, nickel, cadmium, zinc, cobalt, and chromium. The second cleaning solution is known as RCA standard clean 2 (SC-2) and is a mixture of H_2O, H_2O_2, and HCl in a volume ratio of 6:1:1. This solution is designed to remove a variety of ions including alkali ions and Al^{3+}, Fe^{3+}, and Mg^{2+} [32]. The silicon wafers were submerged in each of SC-1 and SC-2 for 10 minutes at 75-80°C.

During cleaning with the SC-1 solution, an oxide layer is formed on the silicon surface which can trap metal impurities [33]. Therefore, following the RC-1 cleaning step, an HF etch was performed to remove the oxide (SiO_2) layer. The wafers were submerged in a solution of buffered oxide etch (BOE; 40% NH_4F in H_2O and 49% HF in H_2O mixed with a volume ratio of 20:1) for approximately two minutes, followed by rinsing in ultra-pure water and drying with N_2 gas.

After the SC-2 clean, the wafers were oxidized to form a passivating layer of SiO_2.This was done primarily to minimize Si surface recombination, but a secondary benefit is that the oxide layer incorporates any remaining impurities. The oxidation was performed in a tube furnace under the following conditions: 1100°C, 3.5 SCFH of O_2 gas, and 0.033 mL/min of H_2O (l) for 5 minutes. Oxide thicknesses were measured to be approximately 50 nm using a J. A. Woollam Co. EC-270 spectroscopic ellipsometer.

ZnS/Si Samples

The ZnS/Si samples analyzed most extensively were all deposited by pulsed laser deposition (PLD). The principles of this method are as follows [34]. The material to be deposited as a thin film is placed in a vacuum chamber along with a substrate material. A high-energy-density pulsed laser is used to evaporate (ablate) the target material and it deposits on the substrate, which is heated to an appropriate temperature (approximately 400°C for ZnS/Si).

The PLD-fabricated samples studied in this dissertation were analyzed via transmission electron microscopy with integrated energy dispersive x-ray spectroscopy (EDX, to measure elemental composition). TEM images, and fast fourier transforms (FFTs) of the images, for three ZnS films deposited on Si(100) are shown in Figure 4, Figure 5, and Figure 6, corresponding to samples named ai, aii, and aiii, respectively (see Table 1). Sample ai is clearly polycrystalline, as evidenced by the rings in the FFT of the ZnS. The brightness at the interface could either be indicative of interfacial oxygen or just a change in image contrast due to the interface (no EDX was performed on this sample). The arrangement of atoms in the bright region appears ordered and identical to the silicon bulk, suggesting that the brightness is not due to an oxide layer (which would be amorphous). Based on this and the evidence in Chapter V, we conclude that very little to no interfacial oxygen is present at this interface. Sample aii begins with epitaxial growth, and then becomes polycrystalline with grain boundaries perpendicular to the interface.

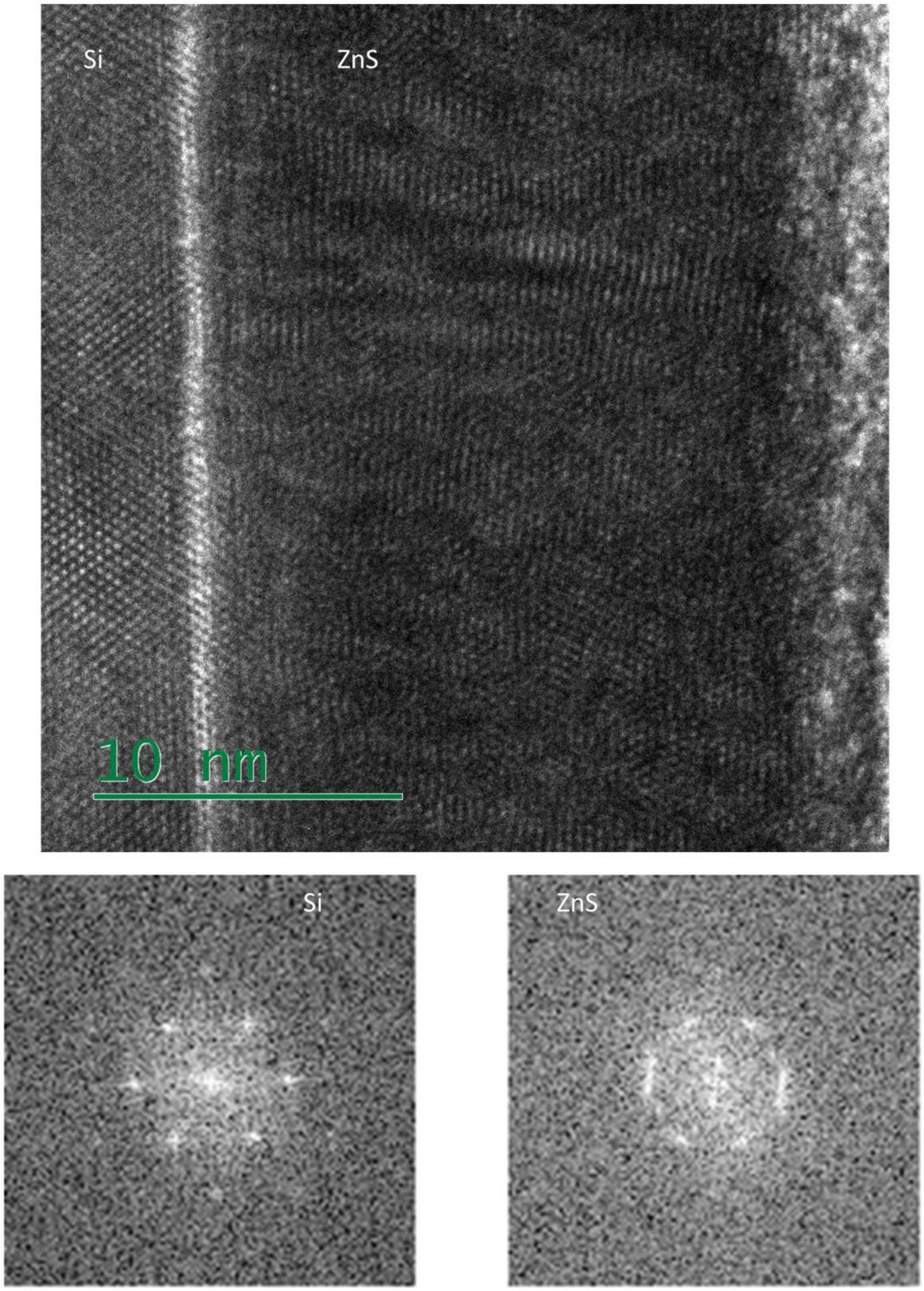

Figure 4. TEM image (top) and FFT calculations (bottom) of Si (left) and ZnS (right) for sample ai. The ring-like structure in the FFT of ZnS indicates polycrystallinity.

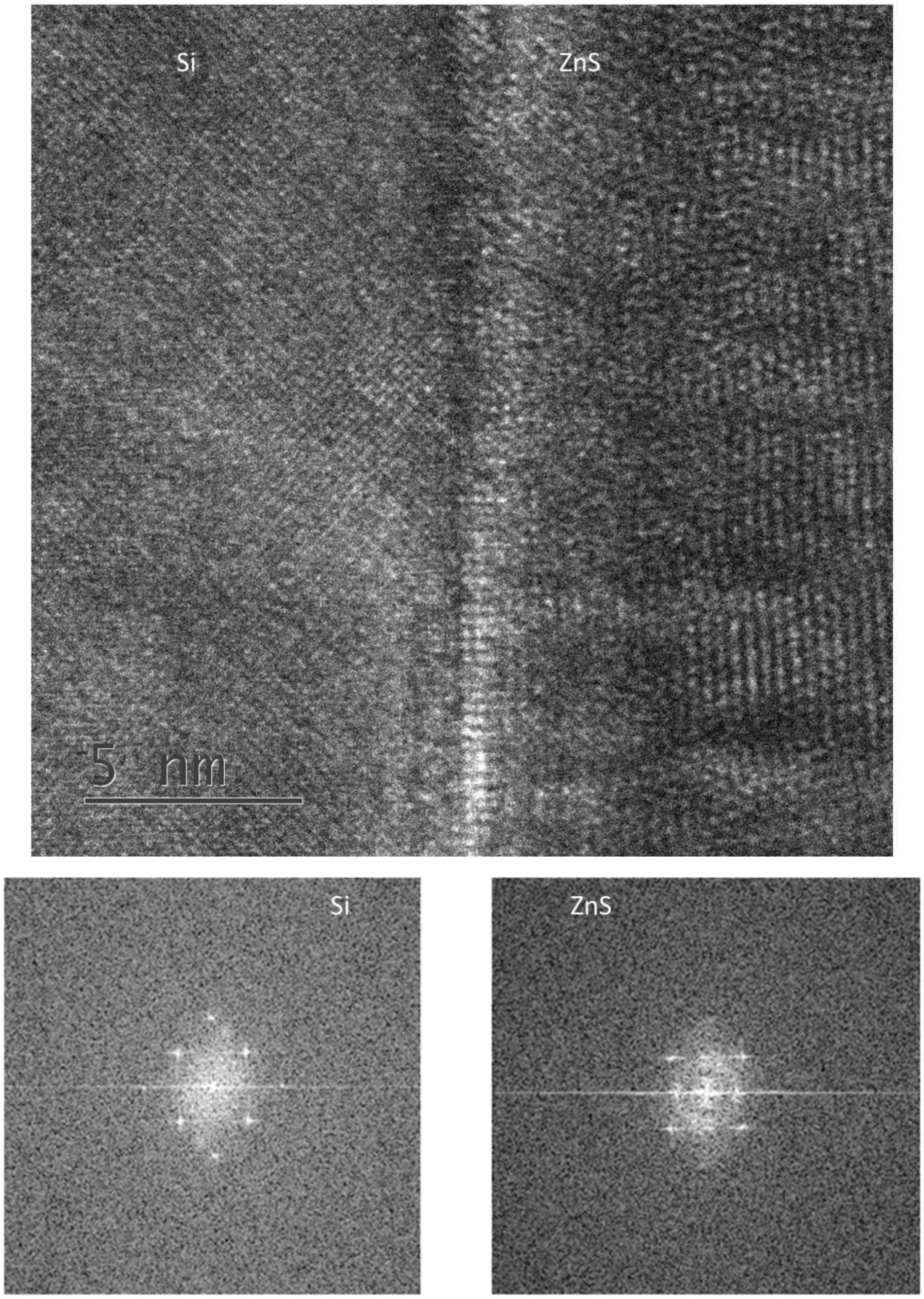

Figure 5. TEM image (top) and FFT calculations (bottom) of Si (left) and ZnS (right) for sample aii. The sharp dots in the FFT of ZnS indicate preferred crystal orientation.

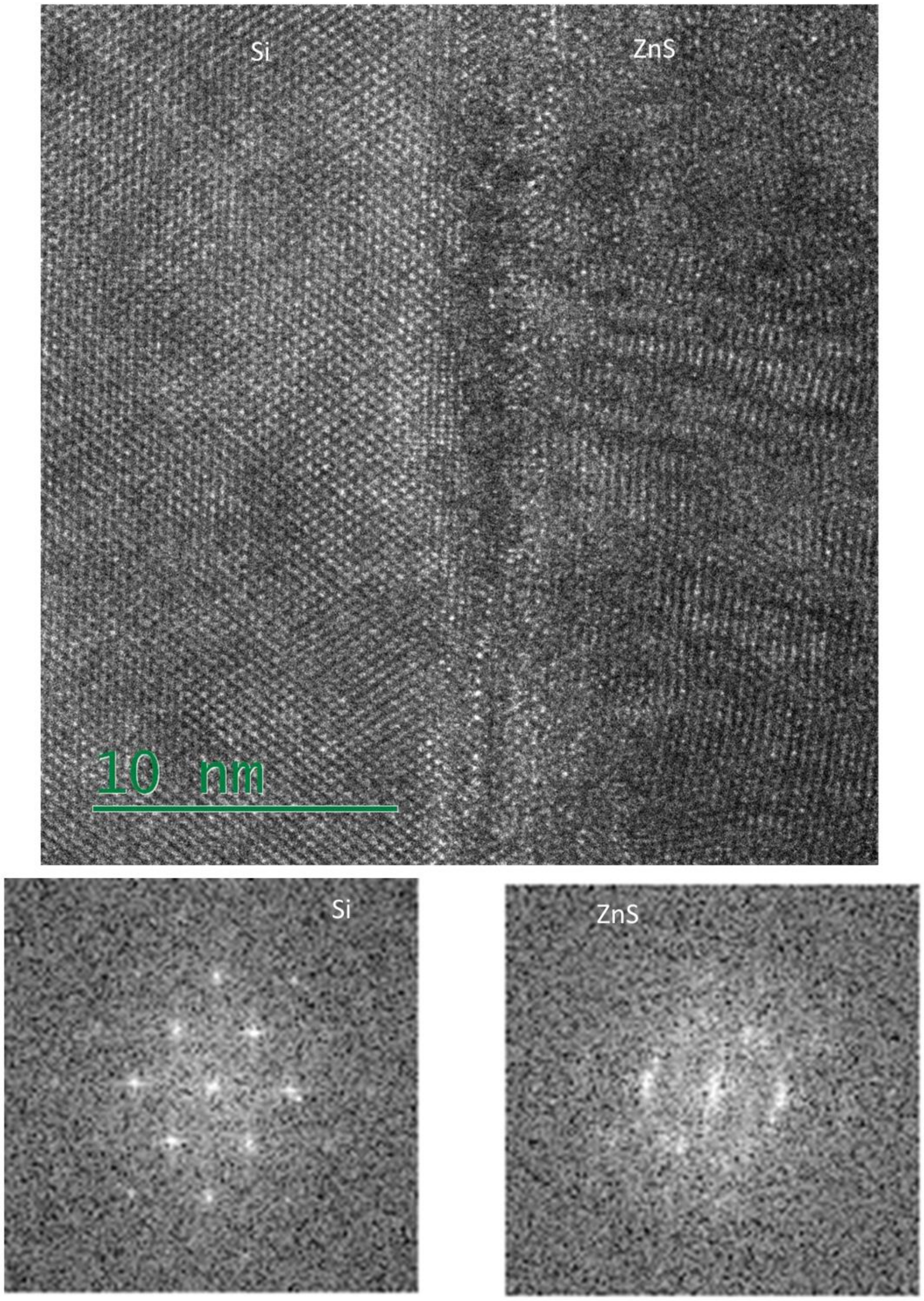

Figure 6. TEM image (top) and FFT calculations (bottom) of Si (left) and ZnS (right) for sample aiii.

The sharp dots in the FFT of ZnS, which align with the Si, indicate a preferred ZnS crystal orientation that matches the Si substrate. EDX on this sample indicated no interfacial oxygen, and an interface width of 3 nm. Sample aiii begins with epitaxial growth, intermixed with disordered regions, and then becomes polycrystalline with a limited degree of preferred orientation. EDX on this sample indicated 4 atomic percent of oxygen at the interface, and an interface width of 8 nm. TEM images and convergent beam electron diffraction (CBED) diffractograms for samples bi, bii, and biii are shown in Figure 7, Figure 8, and Figure 9, respectively. Sample bi is polycrystalline with no preferred crystal orientation. Sample bii was grown epitaxially and the film is a single crystal of ZnS. The pattern of spots in the CBED image indicates a single crystal film throughout the thickness of the sample. EDX on this sample indicated no interfacial oxygen, and an interface depth of 2 nm. The TEM image for sample biii shows evidence of an interfacial oxide layer (bright and amorphous), and the ZnS appears polycrystalline. The CBED diffractogram, which was acquired from a different region of the sample, suggests that the film is single-crystal. EDX confirmed the presence of interfacial oxygen (12 atomic percent), and indicated an interface depth of 4 nm. These results are summarized in Table 1 in Chapter V, where they are also correlated to interface recombination velocities, interfacial defect densities, and probabilities of HAII.

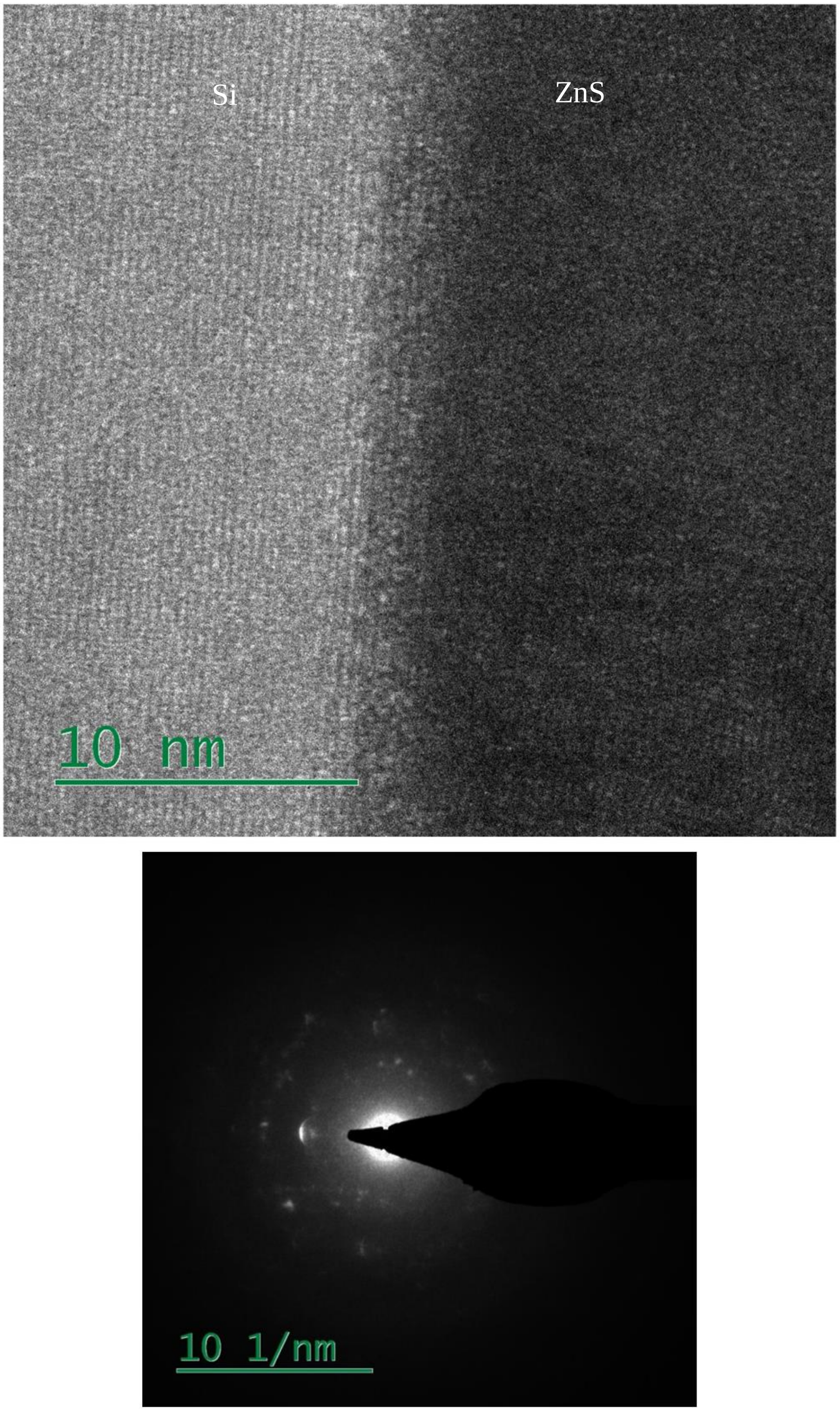

Figure 7. TEM image (top) and CBED diffractogram of the ZnS film (bottom) for sample bi.

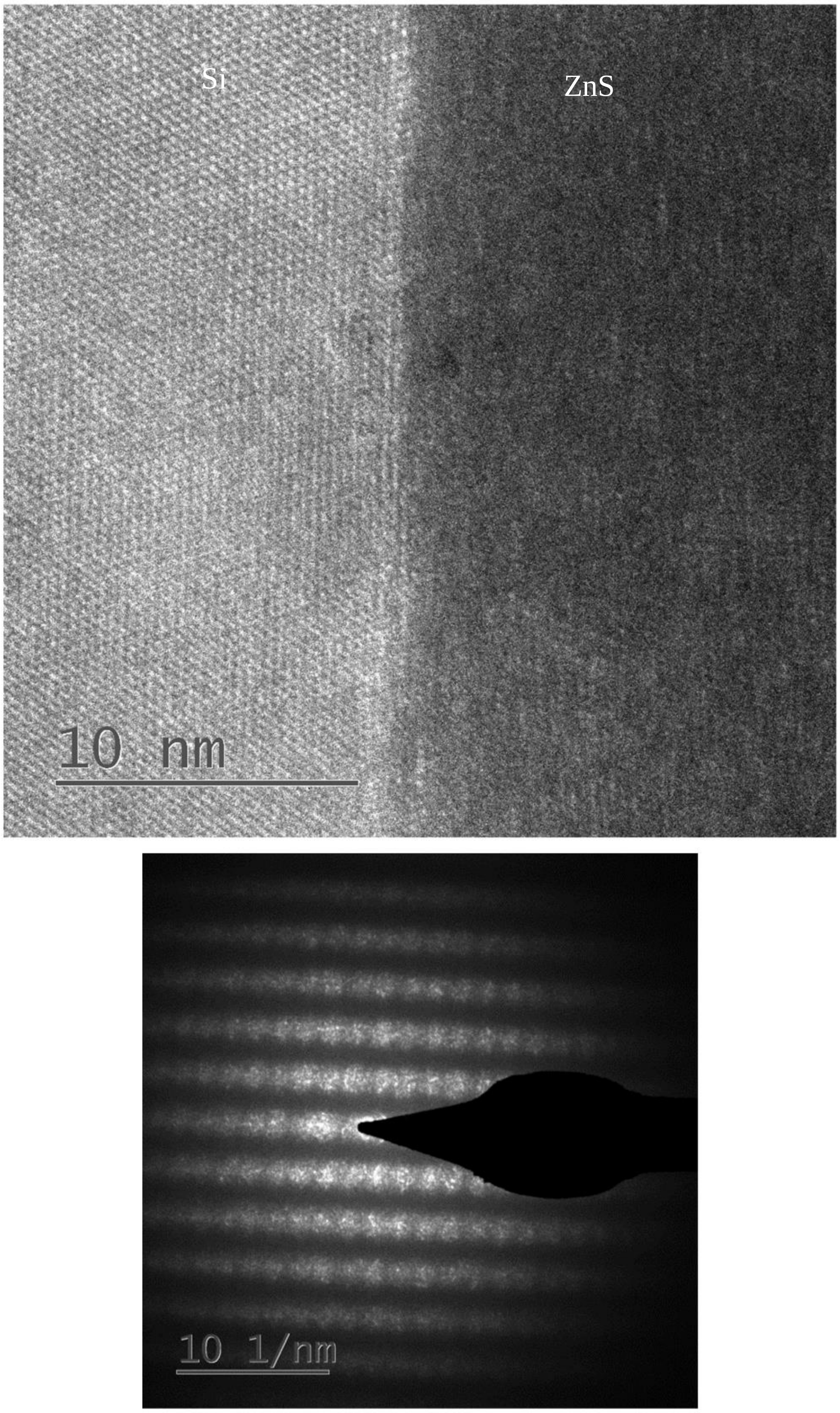

Figure 8. TEM image (top) and CBED diffractogram of the ZnS film (bottom) for sample bii.

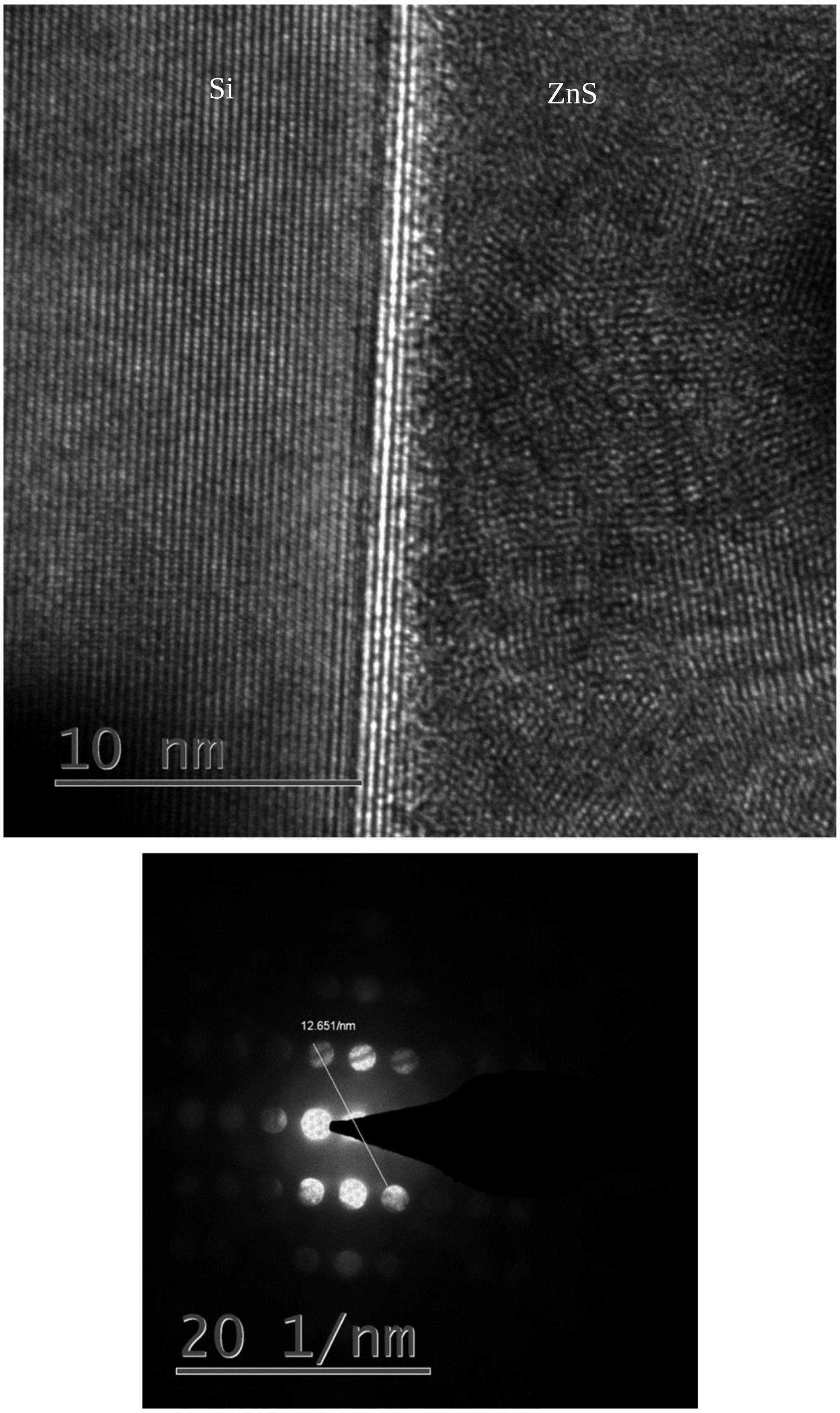

Figure 9. TEM image (top) and CBED diffractogram of the ZnS film (bottom) for sample biii.

ZnSe/Si Samples

ZnSe/Si samples were deposited nLIGHT corporation in Vancouver, WA, with a proprietary technique. The deposition occurred via evaporation under ultra-high-vacuum conditions and at a substrate temperature of approximately 150°C. 20 nm films were deposited on the same Si(100) and Si(111) substrates (with native oxide removed) as used for ZnS film substrates. The resulting films were polycrystalline due to the lattice mismatch with silicon.

CHAPTER IV

FREE CARRIER DYNAMICS IN SILICON

An analysis of free carrier dynamics in silicon is described in this chapter. Using the technique described in Chapter II, the internal quantum efficiency in silicon is measured for three excitation wavelengths. Due to the high absorption coefficient for 400 nm and 267 nm excitation light, high carrier concentrations (>10^{18} cm^{-3}) are generated, and cause an artificial enhancement in IQE due to an enhanced free carrier absorption cross section (σ_{FCA}). By varying the excitation intensity with 400 nm, the relationship between σ_{FCA} and free carrier concentration is quantified. A variation of this model is used to help interpret the results of heterostructure materials in Chapter V. Frederick G. Moore was an invaluable collaborator throughout development of this work including data acquisition, analysis, interpretation, and modeling (to determine $\sigma_{FCA}(N)$). This chapter includes material with co-authors Frederick G. Moore, Brock M. Tillotson, Stephen D. Kevan, and Geraldine L. Richmond, published as Meitzner, K. J., Moore, F. G., Tillotson, B. M., Kevan, Stephen D., and Richmond, G. L. (2013). Time-resolved measurement of free carrier absorption, diffusivity, and internal quantum efficiency in silicon. Appl. Phys. Lett. **103**(9): 092101.

Interpreting the Spectra

The raw data acquired from the laser experiment are in the form $\Delta R = R_{pumped} - R_{unpumped}$ and $\Delta T = T_{pumped} - T_{unpumped}$, as previously described. The pump pulse generates free carriers which, in general, cause a decrease in both reflectivity and transmission of the probe pulse. This is demonstrated in Figure 10, which shows ΔR and ΔT for a <100> silicon sample with 800 nm excitation. The absorption depth for 800 nm is quite long (7 µm; this is the longest absorption depth used) and thus the change in reflectivity is small ($-1.7*10^{-3}$) relative to the change in transmission ($-8.2*10^{-3}$). That is, the number of free carriers within 35 nm of the surface is small compared to the total number of free carriers. Even in this case, however, the change in reflectivity is not trivial when quantifying the free carrier absorption ($I_{FCA} = -\Delta R - \Delta T$). ΔR in this example accounts for 17% of I_{FCA}, and this percentage increases monotonically with decreasing excitation wavelength.

Figure 11 and Figure 12 show ΔR and ΔT for 400 nm and 267 nm excitation, respectively (same Si sample). The magnitude of ΔR, relative to ΔT, clearly increases with decreasing excitation wavelength (especially at short Δt). The decrease in ΔR produces a simultaneous increase in ΔT because a decrease in reflected light yields an increase in transmitted light. This effect is convoluted by free carrier absorption of the transmitted signal, which acts to decrease ΔT. That is, the transmission signal is affected by two phenomena: reflectivity and free carrier absorption. This is most easily observed with 267 nm excitation, where ΔT actually becomes positive (between 1 and 10 ps) due to the large decrease in reflectivity, even though free carrier absorption is occurring (Figure 12). With time, free carriers diffuse into the bulk, ΔR decreases, and ΔT becomes dominated by FCA.

ΔR and ΔT in Figure 10, Figure 11, and Figure 12 all flatten and approach a constant y-value before the end of the spectra (Δt=3000 ps). ΔR flattens due to free carrier diffusion away from the surface region and into the bulk of the wafer. This occurs

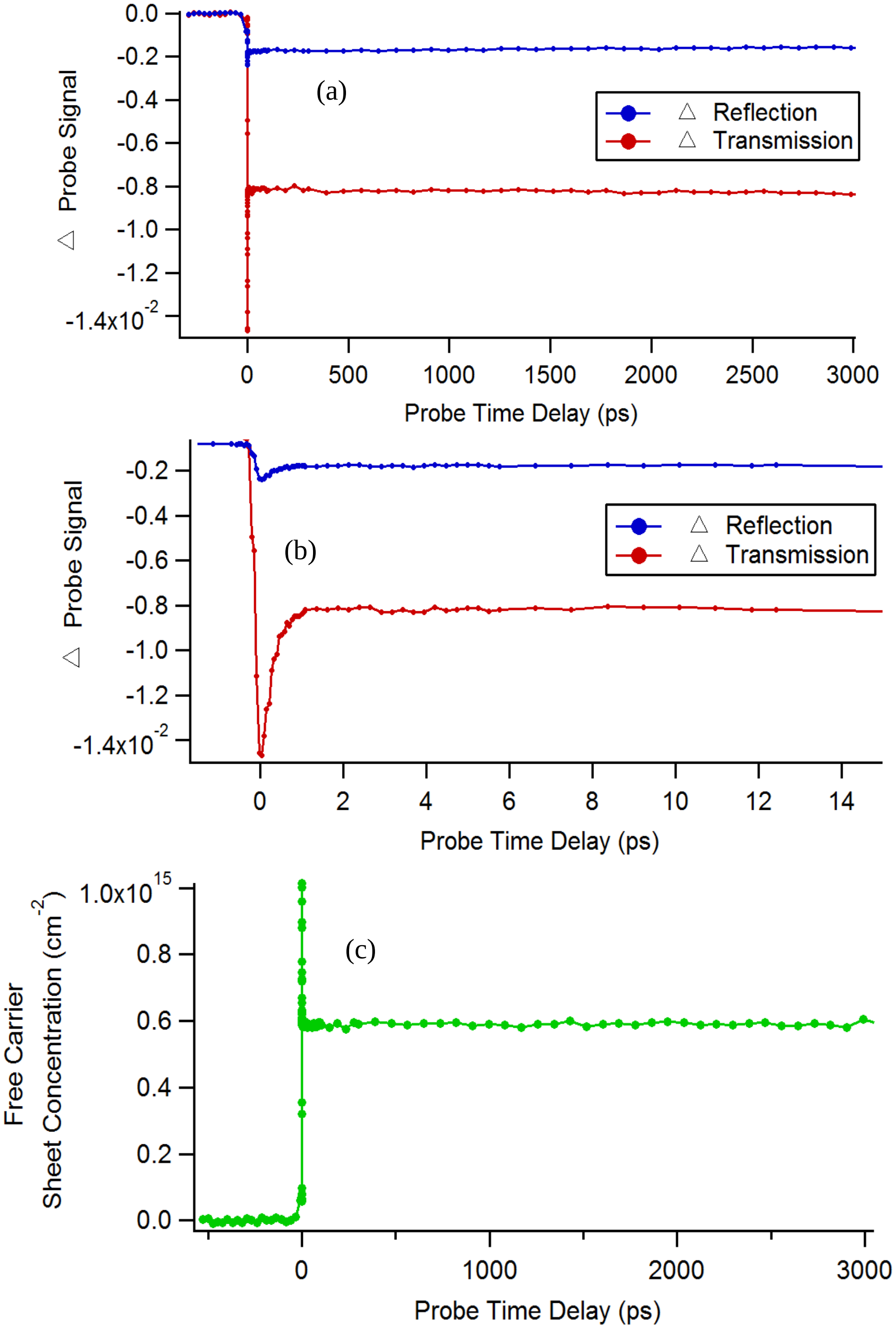

Figure 10. (a) Full and (b) zoomed spectra of the change in reflectivity and transmission of a <100> Si sample with 800 nm excitation. (c) shows the free carrier sheet concentration calculated using eq. (7).

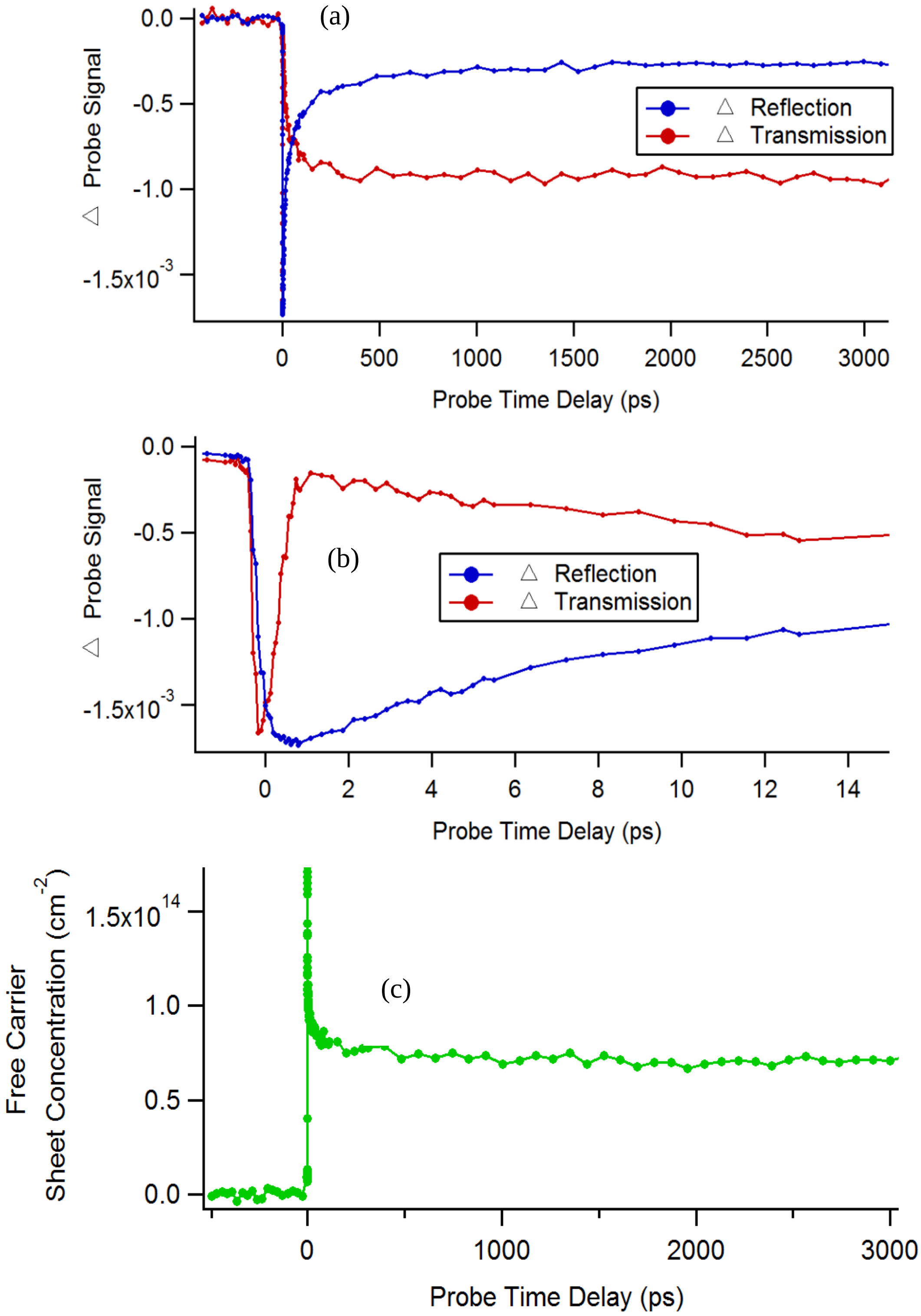

Figure 11. (a) Full and (b) zoomed spectra of the change in reflectivity and transmission of a <100> Si sample with 400 nm excitation. (c) shows the free carrier sheet concentration.

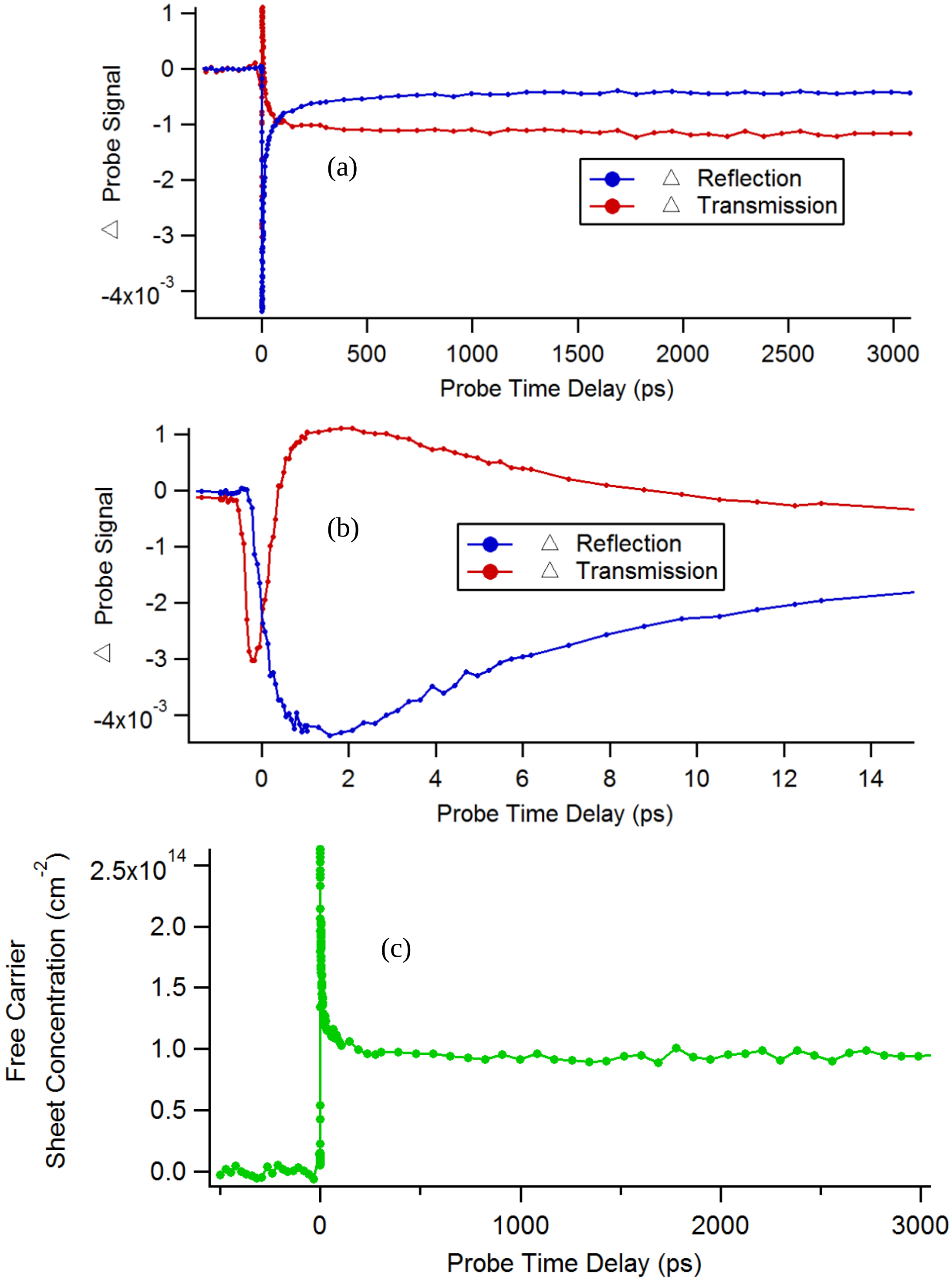

Figure 12. (a) Full and (b) zoomed spectra of the change in reflectivity and transmission of a <100> Si sample with 267 nm excitation. (c) shows the free carrier sheet concentration.

on a relatively fast timescale because the probed depth (35 nm) is on the order of the absorption depths for 400 and 267 nm light (160 nm and 3.7 nm [35], respectively). Thus, the gradient in free carrier concentration within the probed depth is high, and the rate of diffusion from this region is fast. The ΔR trace for 800 nm is flat throughout the probed time because the gradient in FCC is low in the probed region. That is, the absorption depth of 800 nm light (7 µm) is much longer than the probed depth.

From ΔR and ΔT, the FCSC can be calculated using eq. (7). The value for σ_{FCA} was found to be $(1.69 \pm 0.03)*10^{-17}$ cm^2, and will be discussed in more detail below. The FCSCs for 800 nm, 400 nm, and 267 nm excitation on Si are shown in Figure 10c, Figure 11c, and Figure 12c, respectively. The peak at Δt=0 in each of these spectra is due to non-degenerate two-photon absorption of the pump and probe beams, which occurs while they are temporally and spatially overlapped. The intensity of this peak scales with pump beam energy intensity, and the width of the peak depends on the pulse durations. The latter effect can be seen in Figure 13, which shows the Δt=0 peak for four different excitation wavelengths. The narrowest peak observed is for 800 nm excitation, which is the fundamental beam with approximately 110 fs FWHM pulse duration. The peaks for 400 nm and 420 nm excitation are significantly broader, which reflects their longer pulse durations. The 400 nm pulse is stretched to approximately 200 fs during second harmonic generation (SHG) of the 800 nm beam. The 420 nm pulse is generated through optical parametric amplification and is stretched to approximately the same duration. Finally, the peak for 267 nm is broadest due to temporal broadening during third harmonic generation (THG) of the 800 nm beam. The probe pulse is produced by optical parametric amplification and has a duration of approximately 200 fs. In each case, the pulse (pump or probe) with the longer duration defines the time resolution of the experiment.

After the peak at Δt=0, the FCSC trace for 800 nm excitation (Figure 10c) is flat for the duration of the spectrum. This is because the bulk free carrier lifetime in high quality Si is long (approx.10 μs) relative to the timescale of this experiment (3 ns), and therefore the free carrier concentration is effectively constant. Recombination at the Si/SiO$_2$ interface is also negligible (below the noise level of these experiments), owing to the high passivation quality of the thermal oxide layer. The FCSC traces for 400 nm and 267 nm have an apparent decay in FCSC at short Δt (beginning at 0.5 ps and ending by ~1000 ps) before they flatten and approach a constant value of FCSC. As described in

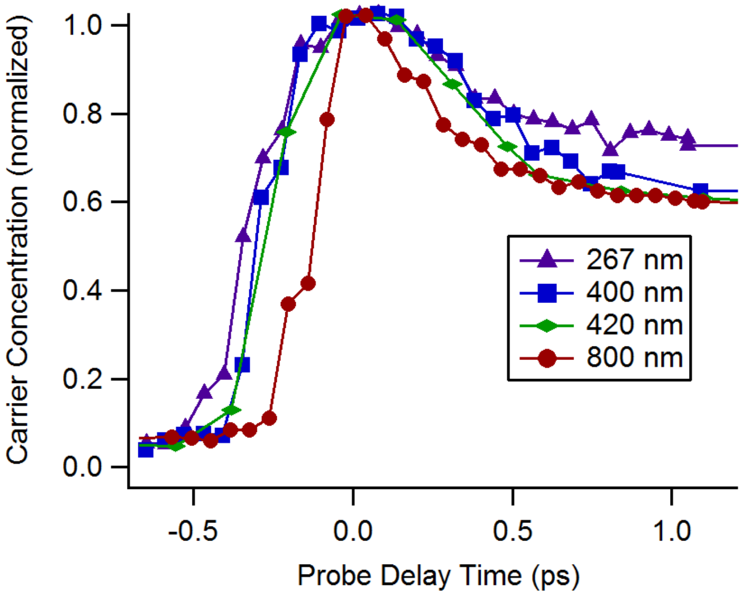

Figure 13. Zoomed in to the peak at Δt=0 for four different excitation wavelengths. The peak width changes with excitation wavelength pulse duration.

detail below, this apparent decay is due not to recombination, but to the time dependence of σ_{FCA} (see eq. (7)).

Internal Quantum Efficiency

Theoretical Considerations

Of particular technological interest is the quantum efficiency of photocarrier generation, or internal quantum efficiency (IQE). This quantity refers to the number of electron-hole pairs generated per photon absorbed in the semiconductor:

$$IQE = \frac{\#\, of\ electron/hole\ pairs}{\#\, of\ photons\ absorbed} \tag{9}$$

In silicon, photons with energy greater than the bandgap energy can be absorbed and produce an electron-hole pair with excess energy (so-called *hot carriers*). This excess energy (E_x) is defined as the difference in energy between the initially excited state of the electron (hole) and the conduction band minimum (valence band maximum). In most cases, this energy is dissipated to the lattice by electron-phonon and hole-phonon scattering (heat generation) within a few hundred femtoseconds [14], and the IQE is equal to unity. For photon energies equal to or greater than twice the bandgap energy ($E_{hv} \geq 2E_g$), however, the electron or hole can gain excess energy that is equal to or greater than the bandgap energy ($E_x \geq E_g$). In these cases, this excess energy can instead be released by excitation of a second electron-hole pair, and the IQE is equal to two. This process is known as impact ionization in bulk semiconductors, such as the ones studied here, and as multiple-exciton generation (MEG) in nanoparticles.

The probability of impact ionization in silicon is very low for most photons in the solar spectrum. A seminal theoretical study by Wolf et al. in 1998 [16] found that impact ionization only accounts for about 0.5% of the maximum theoretical efficiency of a silicon solar cell (31%). The primary reason for such low rates of impact ionization in silicon is that, following the absorption of a high energy photon ($E_{hv} \geq 2E_g$), the excess energy (E_x) is not given exclusively to a single charge carrier but is distributed between the electron and the hole, often leaving neither with sufficient energy to impact ionize [16]. For the absorption of a photon with energy equal to twice the bandgap energy, only two transitions allow impact ionization to occur, while a continuum of transitions result in heat generation due to distribution of E_x between the electron and hole. The probability with which different transitions actually occur depends on the band structure of the semiconductor.

A photon energy $>3E_g$ ensures that at least one charge carrier receives an excess energy greater than the bandgap energy, and is the threshold for the onset of impact ionization in silicon. That is, impact ionization occurs with low probability (<1%) for photon energies below about 3.3 eV, or 375 nm. Above 3.3 eV, the IQE increases gradually up to approximately 1.3 ± 0.1 at 5.0 eV (248 nm) [16]. In reference to the solar spectrum, the shortest wavelength that reaches the Earth's surface is about 290 nm (4.3 eV) [36], which has an IQE in silicon of about 1.15. This illustrates that impact ionization occurs with low probability, even when E_x is equal to or greater than the bandgap energy.

To investigate the relationship between E_x and impact ionization rates in more detail, electrons or holes have been isolated and studied in a system where E_x derives from an applied bias instead of photoexcitation. Anderson et al. found the threshold energies for impact ionization by electrons and holes in silicon to be 1.1 eV and 1.8 eV [37], respectively. Beyond those thresholds, the rates increase with E_x [38, 39]. It follows that in order to promote impact ionization, it is crucial that one charge carrier, preferably the electron, gets the majority of E_x. While it has been proposed that the free carrier excess energy distribution (FCEED) in some semiconductors can be optimized for a given photon energy (to achieve an asymmetric energy distribution) [16], the FCEED changes with photon energy and thus a high overall probability of impact ionization has remained elusive.

Experimental

In order to calculate IQEs in silicon using the technique described in Chapter II, the calculated FCSC is normalized to the absorbed excitation photon flux (AEPL) in the probed region. The AEPL is calculated under the approximation that the probe beam overlaps with only the very center of the pump beam. Because the beam width of the pump beam is at least 7x larger than that of the probe beam, the change in energy density across the probed region is small, and the AEPL is approximately constant (Figure 14). The AEPL is calculated using the total pump pulse energy and the spatial profile of the beam, which is measured using the razor edge method. An example of a spatial beam profile is shown in Figure 15. Using the Gaussian fit parameters, the energy density at the center of the beam is calculated and used for the normalization (Eq. (9). Because the sample is rotated horizontally such that the angle of incidence for the pump pulse is 49°, the actual beam size in the horizontal direction is elongated by a factor of approximately 1.5. The pump beam reflectivity of each sample is measured at the correct angle of incidence and used to help calculate the absorbed excitation photon flux.

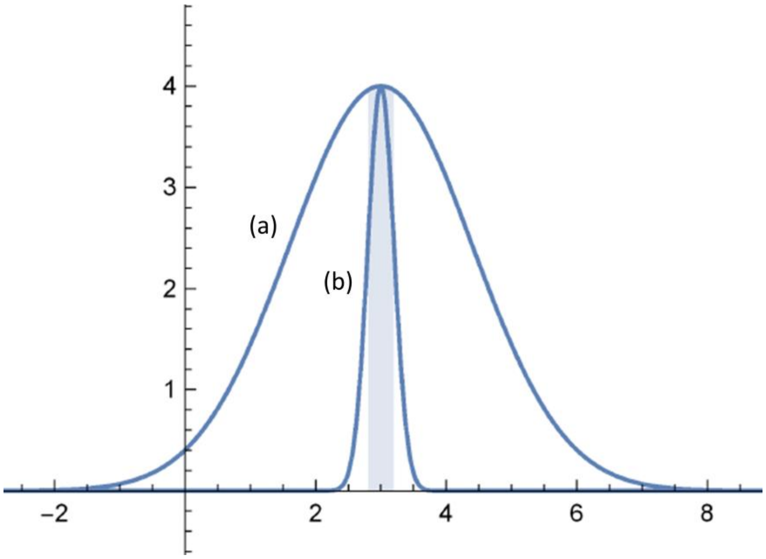

Figure 14. Gaussian beam profiles of (a) the pump and (b) the probe when the pump is 7x larger than the probe. The shaded region corresponds to the Gaussian beam width of the probe beam.

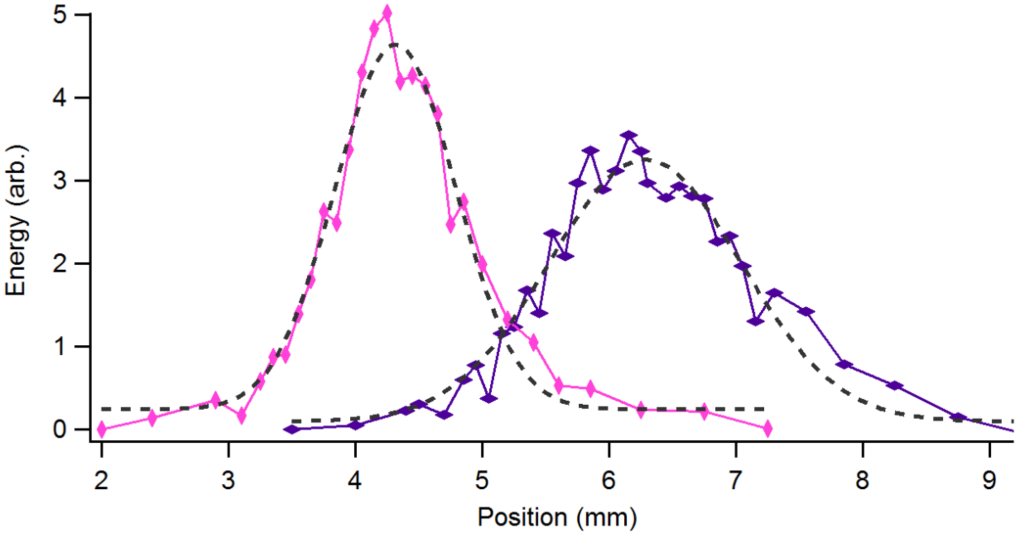

Figure 15. Horizontal (horizontal diamonds) and vertical (vertical diamonds) spatial profile of the 267 nm pump beam. Dotted lines are Gaussian fits.

The IQE of photocarrier generation in silicon is shown in Figure 16 for 800 nm, 400 nm, and 267 nm excitation. The free parameter in the calculation of IQE was σ_{FCA}. Following the normalization described above, the value of σ_{FCA} was assigned a value such at the IQE for 800 nm was equal to unity (this photon energy is too low to cause impact ionization). As shown in Figure 16, this trace is flat for the entire duration of the spectrum due to negligible losses to surface and bulk recombination. This produced the value of σ_{FCA} = $1.69*10^{-17}$ cm^2, which was used in Equation (7) for all data analysis. The value of σ_{FCA} is not documented for the probe wavelength of 1520 nm, but the value determined here is in good agreement with literature values when taking into account the well-known λ scaling behavior [24, 40-42].

The traces for 400 nm and 267 nm excitation show an apparent decay in IQE (beginning at 1 ps and finishing by 2000 ps) which, as demonstrated below, is due to the dependence of σ_{FCA} on N. The result of this effect is that the traces decay and approach a constant value of IQE, which they reach by about 2000 ps. Therefore, the IQE has been extracted as the asymptotic value of each trace at long times ($\Delta t>2000$ ps). The values of IQE for 800, 400, and 267 nm excitation are 1.00, 1.00, and 1.25, respectively. The range of IQE values extracted from scans under nominally identical experimental conditions is within the range ± 0.02.

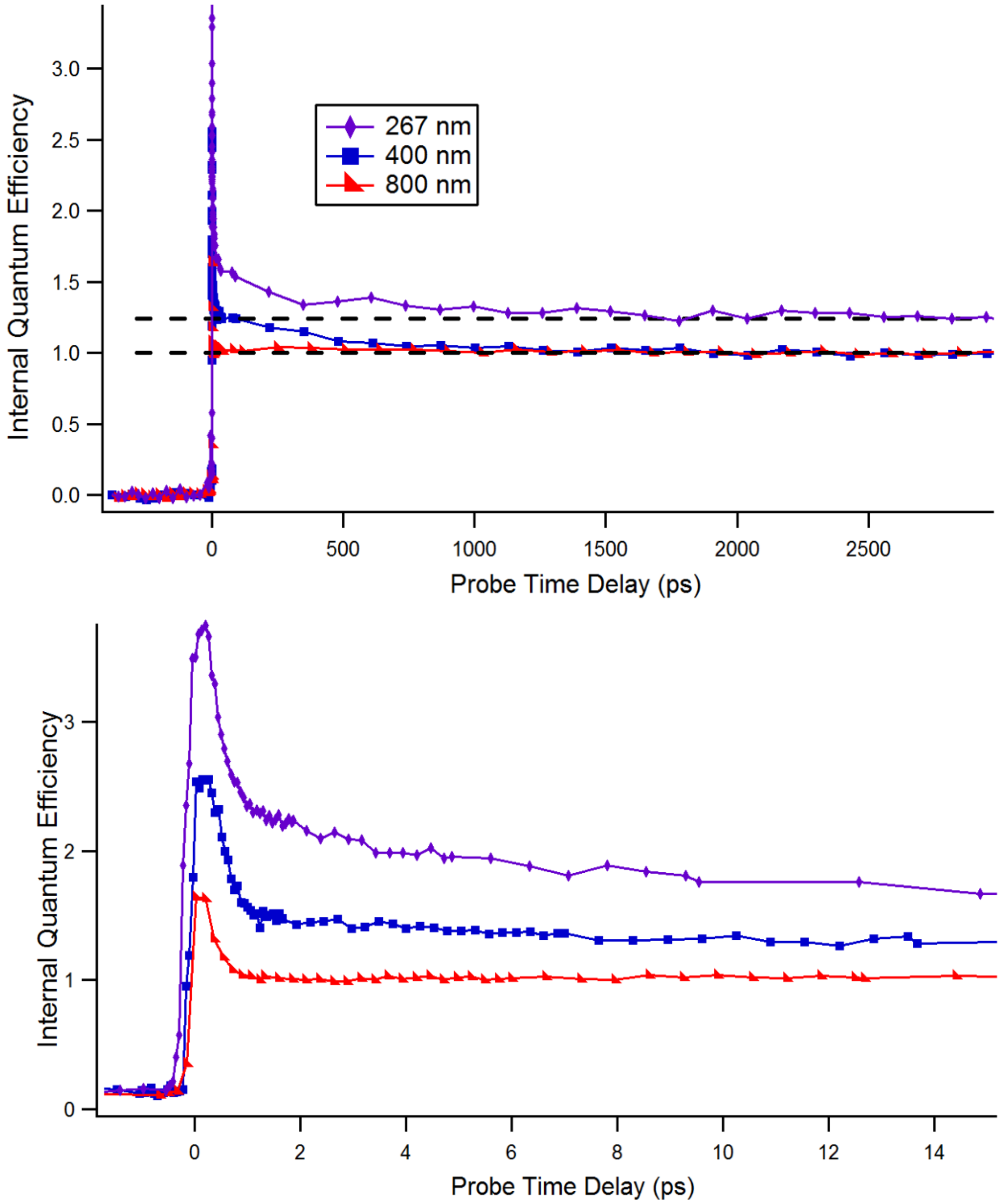

Figure 16. Internal quantum efficiency of photocarrier generation in silicon for three excitation wavelengths. The bottom spectrum is zoomed in to short probe time delay.

The values of IQE determined here are consistent with those previously obtained by measurements of reflectance and short circuit current on illuminated solar cell devices. Though these other techniques suffer losses associated with collection efficiency, it is well known that the IQEs for 800 nm and 400 nm are equal to unity [43, 44]. For photon energies exceeding 3.25 eV, however, there is some discrepancy in the reported values, which range from 1.1 to 1.3 for 267 nm excitation [16]. In many cases, this is attributed to differences in doping or a free carrier collection efficiency that depends on excitation wavelength [43, 44]. Our values of IQE for each wavelength are near (or at) the upper limit of previously reported ranges because our technique does not suffer from the collection efficiency losses associated with those measurements.

Time-Dependent Absorption Cross Section

To further investigate the decays in the traces for 267 nm and 400 nm in Figure 16, the experiment was repeated with 400 nm at multiple excitation intensities. Figure 17 shows spectra for 400 nm excitation on thermally oxidized Si(100) with three different excitation intensities. For clarity, the data are truncated to show only $\Delta t > 0$. In each case, the signal is enhanced at short times (IQE > 1 for $\Delta t < 500$ ps) and decays to an IQE of 1.0 by 2500 ps. With increasing excitation intensity, the magnitude of IQE at short times increases, but in each case the trace still decays to an IQE value of 1. This verifies that the decay is due not to recombination (which would lower the IQE) but to a value of σ_{FCA} that depends on excitation intensity.

There are two reasons that we expect σ_{FCA} to increase with excitation intensity. First, each 400 nm photon that is absorbed in Si releases an excess energy of ($E_{hv} - E_g = E_x$) 2.0 eV to the lattice via phonon scattering. This elevates the lattice temperature by an

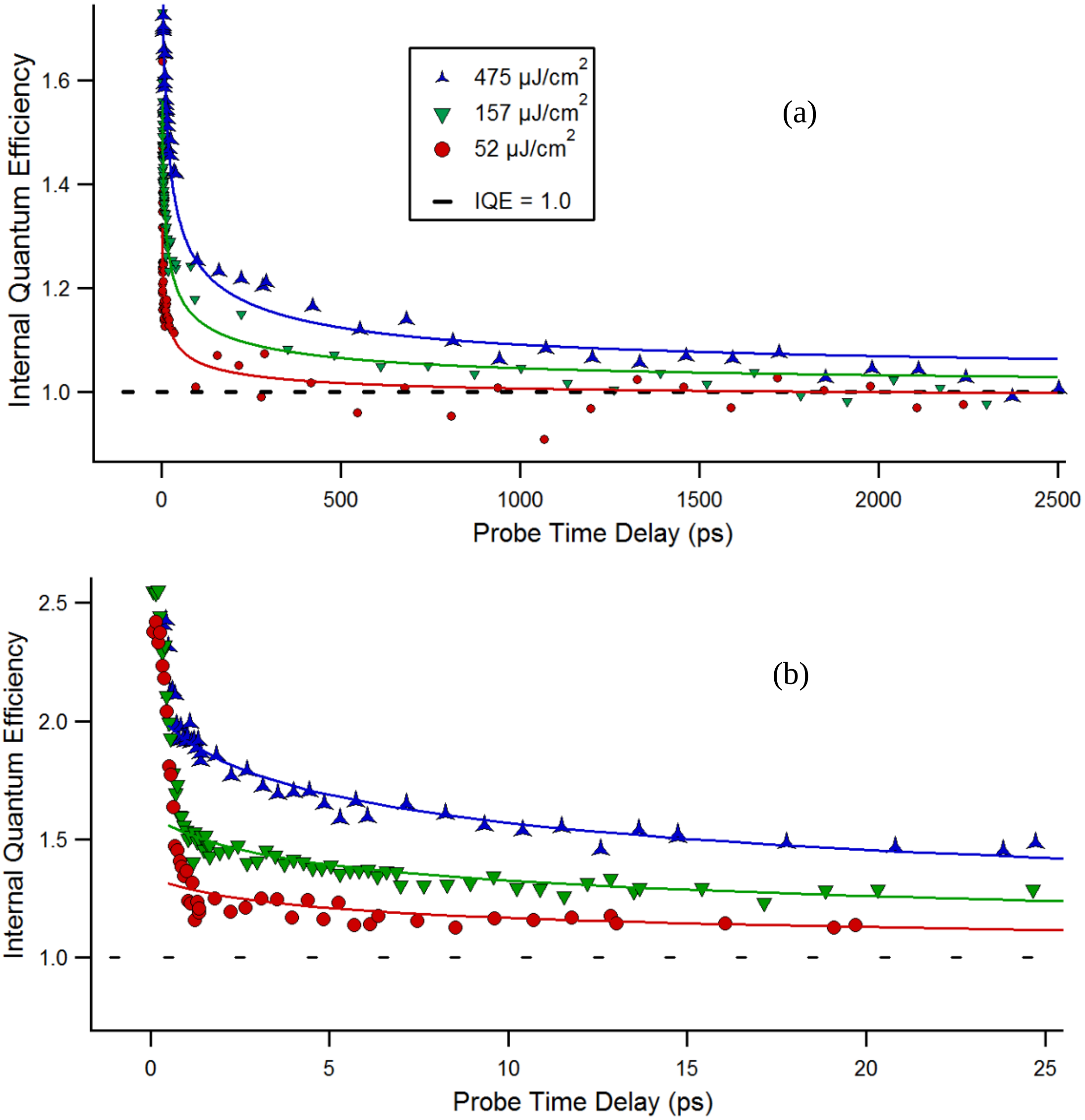

Figure 17. Excitation intensity dependence of the apparent decay in IQE for 400 nm excitation. Solid lines are fits to the data, where the N dependence of $\boldsymbol{\sigma_{FCA}}$ is taken into account. The full spectra are shown in (a), while (b) is zoomed in to short times.

amount that scales linearly with the number of photons absorbed (i.e. excitation intensity). Since σ_{FCA} scales linearly with temperature [45], this results in an initially increased value for σ_{FCA} that decays as the lattice equilibrates with room temperature. Using the specific heat capacity of silicon, excess photon energy, and excitation intensity, it is straight forward to calculate the temperature change associated with each excitation intensity. For the highest intensity of $475\frac{\mu J}{cm^2}$ a temperature increase of 18°C is calculated, which corresponds to an increase in σ_{FCA} of only 0.06 x 10^{-17} cm^2 (an increase by a factor of only 1.04). Thus, this explanation cannot account for the observed enhancements of nearly a factor of 2 at short times (see Figure 17b). Furthermore, this effect is small enough to be considered negligible when considering the following.

The other explanation is that σ_{FCA} increases with free carrier concentration due to increased intercarrier scattering (electron-electron, hole-hole, and electron-hole scattering) rates. Indeed, high carrier concentrations and the associated intercarrier scattering rates are responsible for many significant changes in free carrier dynamics including decreased conductivity mobility [46], decreased diffusion coefficient [47, 48], and increased absorption [49-51]. The effect of intercarrier scattering on absorption scales (in theory) with N^2, while phonon-assisted and impurity-assisted absorption scales with N [51]; The effect of intercarrier scattering becomes increasingly important with high N. The enhanced absorption arises because scattering events cause a net transfer of momentum which assists the indirect free carrier absorption transitions [46]. This phenomenon can occur in silicon for free carrier concentrations above about 2 x 10^{17} cm^{-3} [21, 52], which are easily reached with ultrafast laser pulses and high photon energies with short absorption depths. In the present case, the short absorption depths of 267 nm and 400 nm (3.7 nm and 160 nm, respectively) lead to high free carrier concentrations near the surface of the sample where light is incident. Using the total pulse energy and known absorption depths, we calculate initial (Δt=0 ps) near-surface carrier concentrations of 2.5 x 10^{20} cm^{-3} and 3.5 x 10^{19} cm^{-3} for traces (a) and (b) in Figure 16, respectively. As Δt increases, carriers diffuse toward the bulk, N decreases, and the value of σ_{FCA} approaches its constant value of $1.69*10^{-17}$ cm^2.

In order to quantify the enhancement in photogenerated FCA with increasing N, we consider the initial (Δt=0) distribution of free carriers, time-dependent diffusion toward the bulk, and the dependence of σ_{FCA} on N. Because N is a function of both time and position, σ_{FCA} must be determined by integrating though the (relevant) depth of the sample for each time point.

We begin with excitation and diffusion. The initial distribution of photocarriers is highest at the front surface and decays exponentially moving toward the bulk, as described by the absorption depth of the excitation light. We assume that the carriers diffuse in one dimension (on the z axis, which is normal to the plane of the interface and pointing into the bulk of the wafer) according to Fick's Law. Knowing the absorbed excitation photon flux (and therefore the total number of free carriers) and taking the diffusion coefficient to be 20 cm^2/s, this model provides N(z,t) [53] as

$$N(z,t) = \frac{N_0}{2L}\left\{exp\left[\frac{\sqrt{Dt}}{L}\left(\frac{\sqrt{Dt}}{L} - \frac{z}{\sqrt{Dt}}\right)\right] erfc\left(\frac{\sqrt{Dt}}{L} - \frac{z}{2\sqrt{Dt}}\right) + exp\left[\frac{\sqrt{Dt}}{L}\left(\frac{\sqrt{Dt}}{L} + \frac{z}{\sqrt{Dt}}\right)\right] erfc\left(\frac{\sqrt{Dt}}{L} + \frac{z}{2\sqrt{Dt}}\right)\right. \tag{10}$$

where L is the absorption depth of excitation light, D is the diffusion coefficient, t is time, N_0 is the free carrier sheet concentration, and erfc(z) is the complementary error function.

In order to extract the relationship between σ_{FCA} and N from the data in Figure 17, we use a fitting algorithm derived from the differential form of the Beer-Lambert relationship

$$\ln\left(\frac{I_o}{I}\right) = \int_0^{10\alpha} N(z,t)\sigma(z,t)dz \tag{11}$$

where $\sigma(z,t)$ now depends on both time and position, and the integral is over 10x the absorption depth of the excitation light. We allow the parameters of a sigmoid to vary as we perform a non-linear least squares global fit of the data in Figure 17. The parameters of the sigmoid define the relationship between free carrier concentration and the correction factor for σ_{FCA} (relative to the constant, low N, value).

Our determination of σ_{FCA} enhancement versus N for photocarriers is shown in Figure 18, along with Isenberg and Warta whose work applies to FCA in doped Si [54].

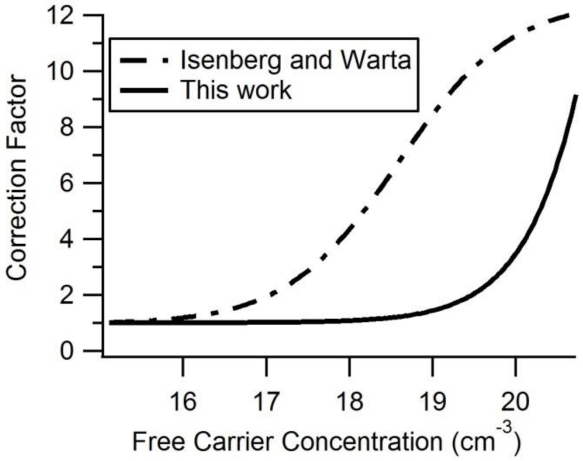

Figure 18. Correction factor for $\boldsymbol{\sigma_{FCA}}$ relative to the value at N = 10^{16} cm^{-3}. This work applies to FCA in photo-excited Si, while the curve from Isenberg and Warta applies to FCA in doped Si.

The difference between enhancement factors determined in this work and those determined by Isenberg and Warta can be explained by the difference between samples where free carriers are produced by photo-excitation versus those where free carriers are produced by doping. The enhancement of σ_{FCA} in doped samples is largely due to carrier-lattice scattering (phonon scattering) and scattering from ionized impurities, and is well predicted by the change in carrier mobility [46, 54, 55]. The onset of enhanced absorption is therefore at lower N values of approximately 3 x 10^{16} cm^{-3}. The enhancement of σ_{FCA} in this work is due to intercarrier scattering, as discussed earlier, which occurs at higher N. Our determination of the enhancement begins at approximately 10^{18} cm^{-3} and increases very quickly above 10^{19} cm^{-3}. This is in general agreement with previous studies, and with the theoretical prediction that enhanced absorption due to intercarrier scattering becomes increasingly important as N increases.

The quantification of $\sigma_{FCA}(N)$ allows us to remove the contribution of enhanced absorption from our spectra. This is demonstrated in Figure 19, which shows a trace for 400 nm excitation (blue, experimental data), where enhanced absorption at $\Delta t<500$ ps is apparent. The curve generated using our model is shown in green, and matches the experimental data very well. Subtracting the enhanced absorption as predicted by the model, we obtain the red trace, which is flat at IQE=1 as expected.

We note here that in general it is not necessary to measure the pump beam diameter in order to perform the excitation energy normalization described earlier. With knowledge of the IQE and σ_{FCA} in silicon, we extract the beam size from spectra (of silicon) by measuring the absorbed excitation photon flux and then setting the beam size such that the known value of IQE is reproduced. When analyzing other materials, we

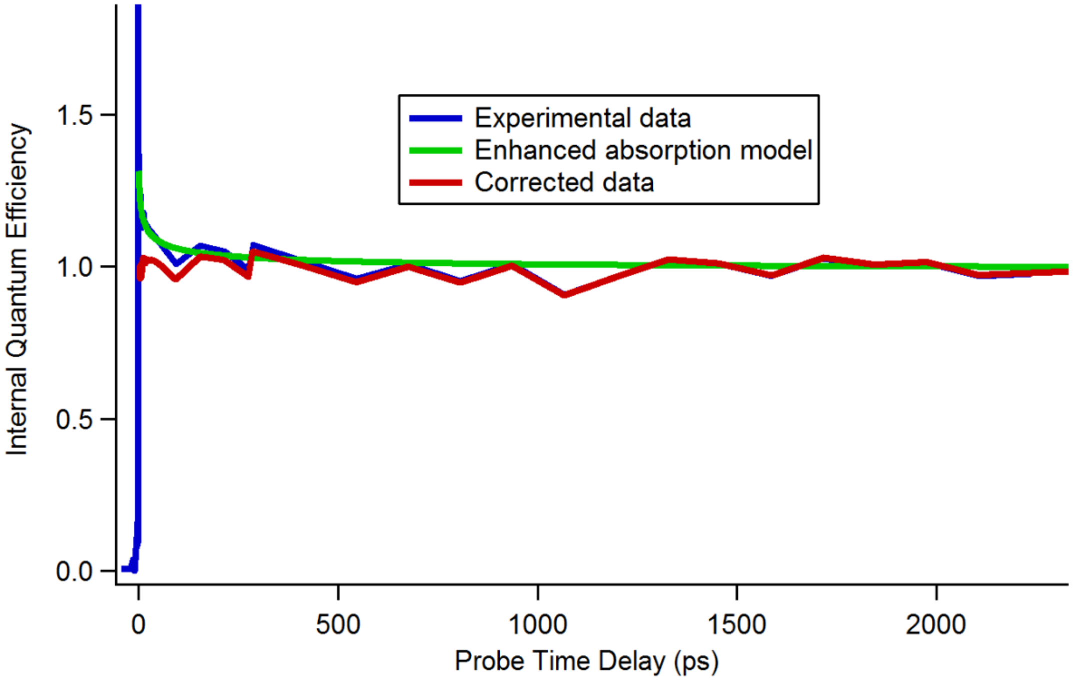

Figure 19. Demonstration of the utility of the model for removing the contribution of enhanced absorption, due to $\sigma_{FCA}(N)$, from spectra where free carriers are excited in silicon with high concentrations (>10^{18} cm^{-3}).

simply analyze silicon before and after the sample of interest and use the silicon spectra to extract the beam size. This also accounts for the effect of any day-to-day or even scan-to-scan changes in experimental conditions that might affect the results.

Applications

As demonstrated in the next chapter, this model is necessary for the analysis of spectra obtained from more complex materials (i.e. ZnS thin films on Si substrates). In many cases, when analyzing thin films on Si substrates, the spectrum contains a contribution from enhanced absorption, as described above, that is convoluted by a decay in IQE that is due to electron-hole recombination. This is also the case for plain Si that is not well-passivated (see Appendix A). It will be shown that, with a simple modification, this model is effective to remove the contribution of enhanced absorption from these spectra and allow quantification of interface recombination velocities.

CHAPTER V

HETEROJUNCTION-ASSISTED IMPACT IONIZATION AND OTHER FREE CARRIER DYNAMICS IN ZnS/Si AND ZnSe/Si

An analysis of ZnS/Si and ZnSe/Si samples is presented in this chapter. Fabrication and characterization of these materials was presented in Chapter III, and the technique for analysis of their electronic properties was presented in Chapters II and IV. ZnS and ZnSe thin films on Si substrates were chosen for analysis because they each have unique properties that make them attractive for this research. As discussed in this chapter, these materials are both likely to exhibit heterojunction-assisted impact ionization. The primary requirement for HAII to occur is that the energy of one of the harvest/host (ZnS/Si or ZnSe/Si) interfacial band offsets is equal to or greater than the bandgap energy of the host material (Si). This condition ensures that a free carrier traversing the band discontinuity gains enough energy to impact ionize. As known from work on avalanche photodiodes, a free carrier traversing a band discontinuity “sees” an impact ionization energy threshold energy that is reduced by the energy of the band discontinuity, and thus is likely to impact ionize at interfaces with sufficiently large band offsets (1.1 eV for electrons; 1.8 eV for holes) [56]. Other important considerations, which are discussed in more detail in this chapter, include factors contributing to free carrier recombination and the ability of the thin-film materials to absorb a significant portion of the solar spectrum. Recombination pathways introduced within the harvester or at the harvest/host interface would be detrimental to the performance of eventual PV devices and are quantified in this chapter. Indeed, the ZnS/Si interface does promote recombination (which annihilates free carriers) and thus it has been a key to challenge to quantify HAII (which generates additional free carriers) in the presence of this recombination. Finally, these two materials have different abilities to absorb the solar spectrum, due to the magnitude of their bandgap energies, which affects their applicability as PV devices. This chapter includes material that will be published with co-authors Frederick G. Moore, Christopher F. Reidy, Stephen D. Kevan, and Geraldine L. Richmond.

Thin Films of ZnS on Si Subtrates

Background

The ZnS/Si system has been well studied and (in theory) fits our material requirements very well. First, the large bandgap energy of the cubic form of ZnS (3.6 eV) ensures that at least one of the ZnS/Si band offsets (conduction or valence) is larger than the Si bandgap energy (1.1 eV). The band offsets of both the ZnS/Si(111) and ZnS/Si(100) interfaces have been measured, but there is considerable variability in the reported values. For the ZnS/Si(100) interface, a valence band offset energy (ΔE_{VB}) of 1.9±0.1 eV has been measured [57] and is in good agreement with a theoretical study [58]. For ZnS/Si(100) with an interfacial monolayer of As, a conduction band offset of 1.00±0.04 eV was measured [59], but the effect of interfacial As was not known. For the ZnS/Si(111) interface, valence band offsets of 0.7±0.2 eV [60] and 1.9±0.1 eV have been measured [57].

Considering the electron affinities of bulk ZnS (3.9 eV) and Si (4.01 eV), one might expect a large offset in the valence band [61] of about 2.4 eV at the ZnS/Si interface. The reason for the decrease in magnitude as well as variability in experimentally measured values of ΔE_{VB} is related to interfacial dipoles and generation of electronic states within bandgaps. For an ideal ZnS/Si(111) interface, there is an interfacial dipole resulting from Si-S bonds [62] as well as bulk Si states that fall within the ZnS bandgap [63], which cause a decrease in valence band offset [60]. In practice, there is some disorder at the interface that depends on synthesis conditions and reduces the interface dipole (and thus increases ΔE_{VB} relative to the ideal case) by a varying degree. The amount of disorder depends on many experimental parameters including temperature, substrate preparation, film growth rate, and concentration of impurities, and thus it is not surprising that the band offsets vary significantly, especially between different research groups.

For both the ZnS/Si(111) and ZnS/Si(100) interfaces, a theoretical study showed that the valence band offset has a bimodal distribution with peaks at $\Delta E_{VB} = 0.9$ eV and 2.1 eV [64]. This is consistent with the experimentally measured values, and considering the arguments presented in [60, 63] it suggests that very high quality (epitaxial growth), polar interfaces result in a smaller value of ΔE_{VB}. This is favorable for the HAII process for two reasons: the built-in field at the ZnS/Si interface is in the direction to move electrons into silicon [60], and electrons have a smaller impact ionization energy threshold (1.1 eV) than holes (1.8 eV) in bulk Si (though we note that the threshold energy for holes may be lower at an interface due to the break in crystal symmetry).

We were not able to measure band offsets in the materials studied in this dissertation. As shown in Chapter III, ZnS film and interface quality varies between samples and therefore it's likely that the band offsets vary as well. Based on the previous arguments, we expect that for high quality, epitaxially grown films, ΔE_{VB} is close to 0.9 eV (making ΔE_{CB} about 1.6 eV), while for lower quality films (polycrystalline) the valence band may be higher at around 1.9 eV (making ΔE_{CB} about 0.6 eV).

Another factor that makes the ZnS/Si an attractive material system is that these materials have lattice constants that differ by only 0.4% [61], and thus epitaxial growth of ZnS on Si should produce an interface with few defects. Interfacial defect states that trap free carriers and facilitate recombination are detrimental to eventual PV device performance. There are two groups of defect states to consider: those in the ZnS and within the ZnS bandgap at the interface, and those within the Si bandgap at the interface. Although we have not measured the densities of these defects, they affect our results differently and thus we can correlate defect densities to free carrier dynamics and then material properties. The former type (defects in the ZnS and within the ZnS bandgap at the interface) will decrease the probability that a free carrier generated in ZnS transfers successfully into silicon and impact ionizes to produce an additional electron-hole pair. The latter type (defects within the Si bandgap at the interface) increases the probability that a free carrier present in Si, but near to the ZnS/Si interface, will recombine. We can monitor the effects of these two types of defects somewhat independently by varying the photon energy of the excitation pulse such that it is absorbed in either the ZnS and Si, or just the Si.

Using photon energies between 1.55 eV (800 nm) and 3.23 eV (384 nm), we generate free carriers only in the Si. These photon energies are all significantly less than the ZnS bandgap energy (3.6 eV), and thus they pass through the film and are absorbed in the silicon. We use multiple wavelengths within this range because the absorption coefficient for these photons in Si increases with increasing photon energy [35]. Thus, by varying the excitation photon energy, we vary the average initial proximity of free carriers to the interface.

There are two processes of interest that depend on the initially generated free carrier distribution in silicon. The first is recombination, which on the timescale of this experiment (3 ns), occurs only at the ZnS/Si interface because the bulk lifetime in Si is relatively long (>10 µs). We will see that recombination rates at the ZnS/Si interface are higher when free carriers are generated closer to the interface, which contains interface states within the bandgap of Si. The other process is diffusion toward the silicon bulk, which occurs at a rate that depends on the gradient in carrier concentration, and thus on excitation photon energy. These two effects occur simultaneously and together they determine the shape of the observed decays in free carrier concentration.

Results and Discussion

In this analysis we consider the rate of decay of the normalized free carrier concentration in ZnS and/or Si. Figure 20 shows the IQE for 9 different excitation wavelengths on sample ai (see Table 1). Each trace represents a different excitation wavelength within the range 1.55 eV to 3.23 eV, which are listed in Table 2 along with the corresponding wavelengths, absorption depths, and IQEs. These photon energies are all below the bandgap energy of ZnS but above the bandgap energy of Si, and thus

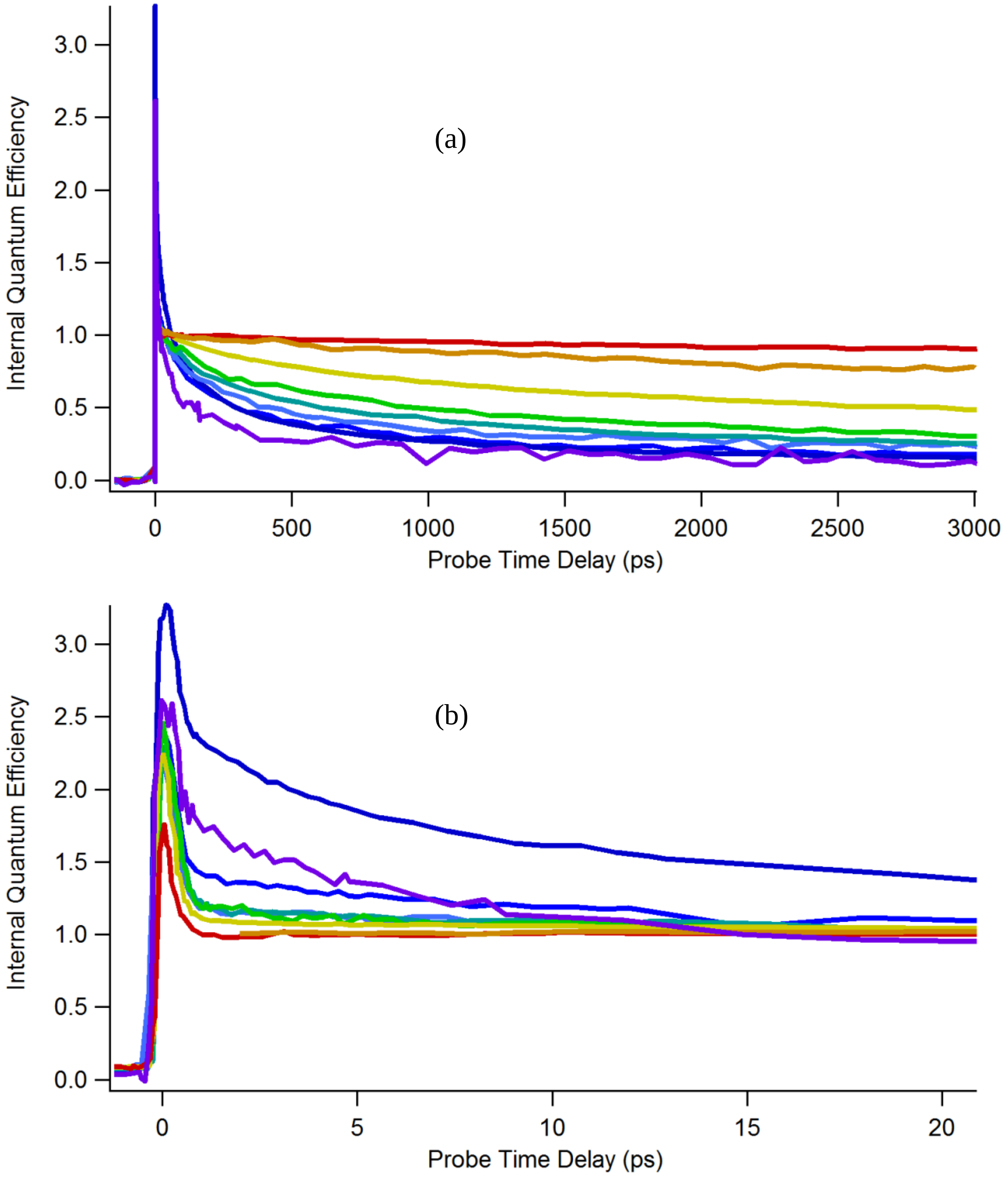

Figure 20. IQE versus Δt for sample ai. (a) shows the full spectra, while (b) is zoomed in around Δt=0. The excitation wavelengths in (b) are, from top to bottom: 400 nm, 384 nm, 420 nm, 449 nm, 472 nm, 500 nm, 565 nm, 690 nm, 800 nm. 400 nm and 384 nm are out of order due to the higher relative intensity of the 400 nm beam. At Δt=3000 ps in (a), the traces correspond, from bottom to top, to excitation wavelength increasing monotonically from 384 nm to 800 nm.

Table 1. Key properties of six ZnS thin films on Si substrates, deposited by pulsed laser deposition.

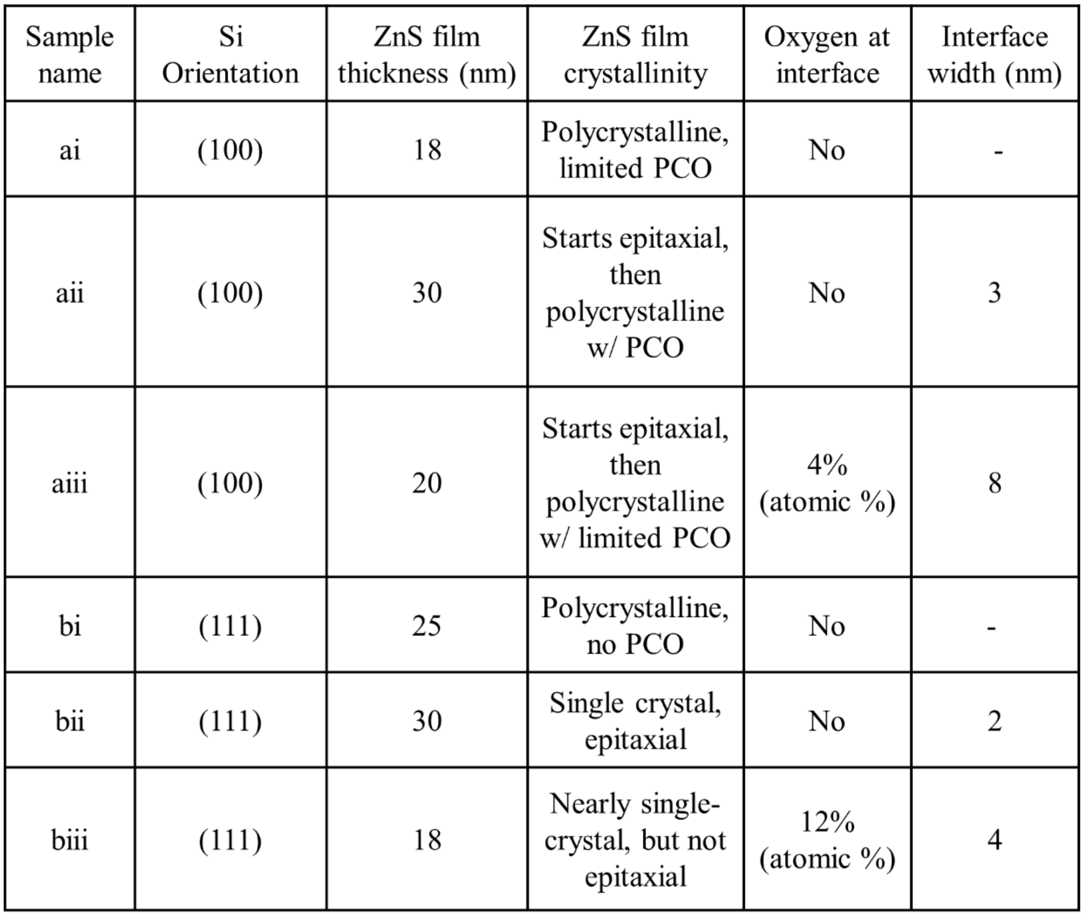

Sample name	Si Orientation	ZnS film thickness (nm)	ZnS film crystallinity	Oxygen at interface	Interface width (nm)
ai	(100)	18	Polycrystalline, limited PCO	No	-
aii	(100)	30	Starts epitaxial, then polycrystalline w/ PCO	No	3
aiii	(100)	20	Starts epitaxial, then polycrystalline w/ limited PCO	4% (atomic %)	8
bi	(111)	25	Polycrystalline, no PCO	No	-
bii	(111)	30	Single crystal, epitaxial	No	2
biii	(111)	18	Nearly single-crystal, but not epitaxial	12% (atomic %)	4

negligible absorption occurs in the ZnS layer and free carriers are generated only in Si. Given the expected band offsets for this system, both electrons and holes are restricted by an energy barrier that prevents them from moving from silicon into ZnS, and the free carriers stay in silicon, eventually recombining at an interface or in the bulk. On the timescale of this experiment, bulk recombination is negligible and all observed recombination must be at the ZnS/Si interface.

Table 2. Wavelength, photon energy, absorption depth, and internal quantum efficiency for each excitation beam used.

Wavelength (nm)	Photon Energy (eV)	Absorption Depth (*10^{-5} cm)	Internal Quantum Efficiency
800	1.55	70	1.00
690	1.80	31	1.00
565	2.19	12	1.00
500	2.48	7.1	1.00
472	2.63	5.3	1.00
449	2.76	3.9	1.00
420	2.95	2.5	1.00
400	3.10	1.6	1.00
384	3.23	0.97	1.00
320	3.87	0.063	1.05
267	4.64	0.037	1.25

Figure 20a shows the full spectra (out to 3 ns) while Figure 20b is zoomed in to short values of Δt. In the full spectra, it is clear that the traces decay to values of IQE less than one, which is due to electron-hole recombination at the ZnS/Si interface. In the zoomed spectra, we see that for excitation wavelengths ≤ 565 nm, the traces begin (Δt = 1 ps) at IQEs > 1, which is due to an enhancement in σ_{FCA} (as discussed in Chapter IV). In order to deconvolute the effects of interface recombination and enhanced absorption, we make a simple modification to the model developed in Chapter IV and apply it to these spectra.

The model, as previously presented, assumes that the carrier concentration is constant through the duration of the spectrum (which is a good assumption for passivated

Si, but is not for these ZnS/Si materials). Due to the presence of recombination, we make the modification of introducing a time-dependent free carrier concentration; we replace N_0 in equation (10) with a time-dependent value N(Δt), which is estimated from absorbed excitation photon flux (measured experimentally) and the IQE values in Figure 20. Ideally, the initial (Δt=1 ps) value of N_0 would be equal to the measured absorbed excitation photon flux multiplied by the IQE of that photon energy in Si. In some cases, the value used in the model is adjusted such that the model fits the observed IQE at short times (Δt=1-5 ps). For all following time points, the value of N_0 is multiplied by the ratio of IQE at time Δt to the initial IQE:

$$N(\Delta t) = N_0 \frac{IQE(\Delta t)}{IQE(\Delta t = 1ps)}\,. \tag{12}$$

This method of approximating N(Δt) retains the form of carrier distribution that is predicted by the model under the assumption of no recombination, but simply adjusts the total number of free carriers. This could lead to a slight over-estimation of $\sigma_{FCA}(z,t)$ because in reality the recombination occurs in the region of highest carrier concentration (near the interface). Conversely, the approximation in equation (12) may cause a slight under-estimation of $\sigma_{FCA}(z,t)$ because the decay in IQE is due to both recombination and the dependence of σ_{FCA} on N, whereas (12) assumes that it is due only to recombination. While neither of these assumptions is expected to cause significant deviations from ideal behavior, they produce opposing perturbations and therefore their combined effect should be inconsequential.

Figure 21 shows the same data as Figure 20 but with the contribution of enhanced absorption from $\sigma_{FCA}(N)$ removed. Each trace starts at IQE = 1 and decays due to

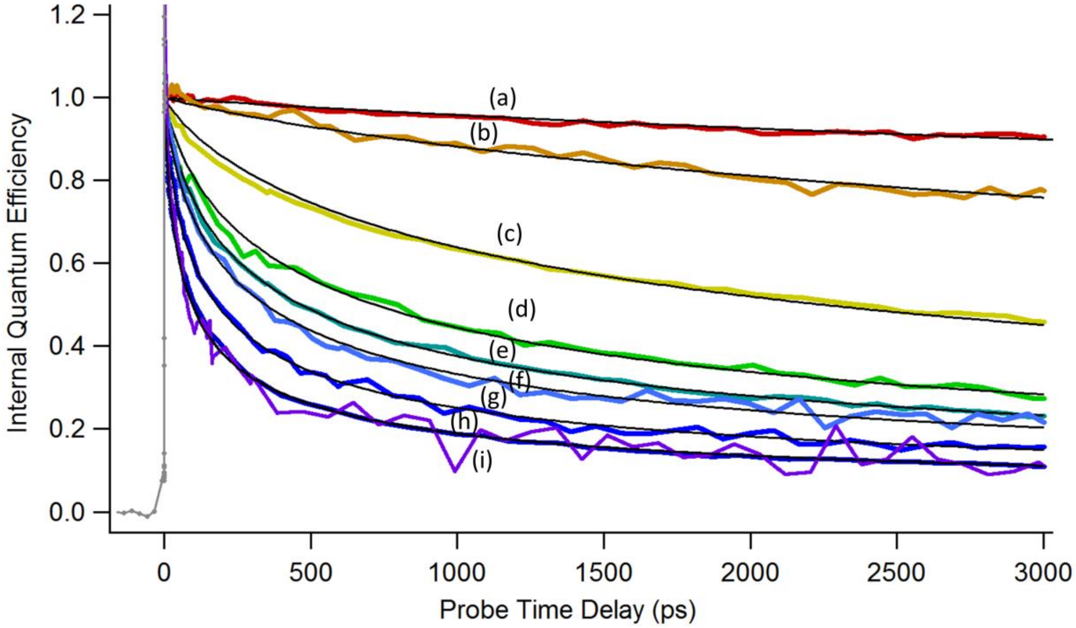

Figure 21. IQE vs Δt for sample ai. Same data as in Figure 20, but the contribution of enhanced absorption, due to $\boldsymbol{\sigma_{FCA}(N)}$, has been removed. Traces correspond to excitation wavelengths: (a) 800 nm, (b) 690 nm, (c) 565 nm, (d) 500 nm, (e) 472 nm, (f) 446 nm, (g) 420 nm, (h) 400 nm, and (i) 384 nm.

recombination at the ZnS/Si interface. It is clear that as the excitation pulse photon energy increases and absorption depth decreases (trace a → i), the IQE decays at a faster rate (i.e. the rate of recombination increases). The increased rate of recombination for shorter absorption depth occurs due to a closer initial proximity of free carriers to the ZnS/Si interface.

The variation in free carrier proximity to the interface with photon energy can be verified by looking at the reflectivity spectra from these analyses. Figure 22 shows ΔR/R, normalized by excitation photon flux, for each trace in Figure 21. The magnitude of ΔR/R (at Δt = 1 ps) increases monotonically with decreasing absorption depth (increasing photon energy) of excitation light due to the increasing number of free carriers within approximately 35 nm of the ZnS/Si interface (see Ch. II).

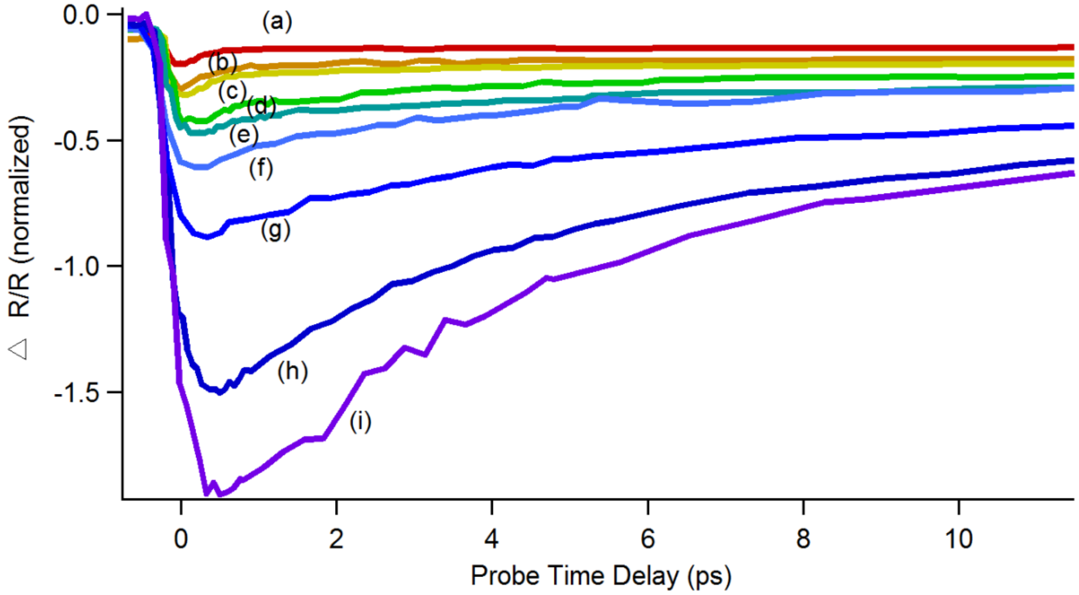

Figure 22. ΔR/R versus Δt for sample ai. Excitation wavelengths are (a) 800 nm, (b) 690 nm, (c) 565 nm, (d) 500 nm, (e) 472 nm, (f) 446 nm, (g) 420 nm, (h) 400 nm, and (i) 384 nm. The magnitude of ΔR/R is proportional to the number of free carriers in Si and within 35 nm of the ZnS/Si interface.

We quantify the ZnS/Si interface recombination velocity (IRV) by fitting the decays in Figure 21 to the analytical expression [65]

$$\frac{I(t)}{I(t=0)} = \left(\frac{1}{A}\exp(A^2T)\,\mathrm{erfc}\left[A\sqrt{(T)}\right] - \frac{1}{S}\exp(S^2T)\,\mathrm{erfc}\left[S\sqrt{(t)}\right]\right)\frac{SA}{(S-A)}\exp(-T), \tag{13}$$

where A, T, and S are the reduced absorption coefficient, time, and IRV, respectively, and we have used an approximation for the exp(x^2)erfc(x) function that is more accurate at extreme values of x [66].The reduced parameters are defined in terms of the absorption coefficient (α), the bulk luminescence lifetime (τ), the interface recombination velocity (s), and the ambipolar diffusion coefficient (D) as A=α(Dτ) $^{1/2}$, T= t/τ, and $S=s\left(\frac{\tau}{D}\right)^{1/2}$. In performing the fits, we have used D=20 cm^2/s [30, 47],τ=1*10^7 ps [24], α values corresponding to the wavelength of excitation light [35], and IRV as the fitting parameter. This expression was derived from the one-dimensional continuity equation, and describes the normalized free carrier concentration in a semi-infinite semiconductor slab after excitation with a delta-function light pulse. As shown by the solid black lines in Figure 21, it fits the experimental data very well throughout the range of time values. This additionally indicates that none of the parameters in the expression exhibit a time dependence. We have also performed experiments with varying excitation intensity, which verified that the results are independent of N. This suggests that the interfacial defect densities are, in every case, much greater than N.

As previously discussed, the IRV varies with excitation light absorption depth due to variation in initial proximity of free carriers to the interfacial defects. Thus we plot, in Figure 23, the absorption depth of excitation light versus IRV (extracted from fits such as those in Figure 21). The range of excitation wavelengths is from 384 nm to 800 nm (from left to right, with 384 nm corresponding to the shortest absorption depth). There are three sets of data in each plot, which in total correspond to the 6 samples in Table 1. The names of each sample correspond to the labels in Figure 23; for example, the data for the sample labeled aii in Table 1. is shown in Figure 23a, trace (ii). The three samples in each graph are ostensibly identical, but differ in key characteristics, as summarized in Table 1.

In general, the magnitude of IRV is expected to increase with increasing density of interfacial defect states [67], which produce electronic states within the Si bandgap. Interfacial defect states arise primarily due to Si-S and Si-Zn interactions, both of which produce electronic states within the Si bandgap. The electronic states associated with

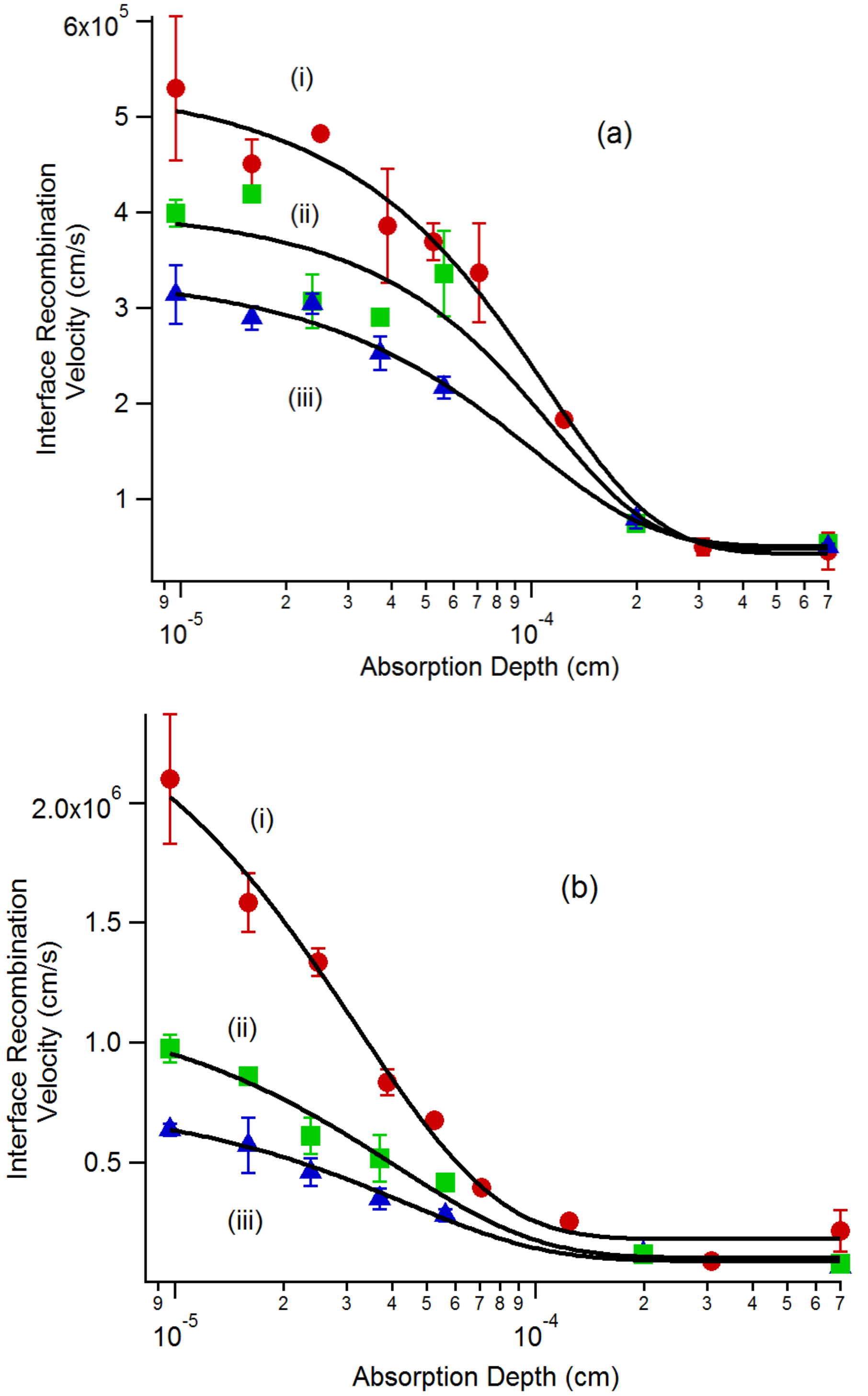

Figure 23. Interface recombination velocity versus absorption depth of excitation light for all 6 samples in Table 1. The relationships between absorption depth, photon energy, and photon wavelength are given in Table 2. (a) shows data for ZnS films on Si(100), while (b) shows data for ZnS films on Si(111). Solid lines are sigmoidal fits.

sulfur in silicon have been well-studied and are known to exist within the silicon bandgap. There are two primary states, with similar concentrations, at approximately 0.32 eV and 0.59 eV below the silicon conduction band edge. At least one of these states is a donor and thus has a positive charge when not occupied, which contributes to its high electron capture cross section of greater than 10^{-14} cm^2. One or more other states exist, though with much lower concentration, at energies even closer to the conduction band edge [68, 69]. A state associated with Si-Zn interactions is approximately 0.8 eV below the conduction band [69].

Comparing the IRVs in Figure 23 to the material properties summarized in Table 1, some correlations can be made. First, the lowest IRVs are observed for samples with the most interfacial oxygen content (samples aiii and biii have the highest % oxygen content and lowest IRVs, when compared with the other films in their sets). This is consistent with previous results demonstrating that ZnS/Si interfacial oxygen reduces the density of defect states [70, 71]. Second, higher IRVs are observed for samples with polycrystalline films compared to those with epitaxial film growth (samples ai and bi have higher IRVs compared to samples aii and bii, respectively).

It appears that these states not only trap free carriers but promote recombination on a picosecond time-scale. If free carriers became trapped but did not recombine, they would remain able to absorb the probe beam due to the probe beam photon energy which is, in almost every case, larger than the energy difference between the band edges and the trap states. It is also possible that carriers remain trapped, and able to absorb probe beam photons, but do so to a lesser extent than free carriers (i.e. trapped carriers have a lower absorption cross section than free carriers).

We observe that the data in Figure 23a and Figure 23b fit to sigmoidal curves, but the value of absorption depth at which the inflection of the sigmoid lies is different for films on Si(111) compared to Si(100). The higher magnitude of IRV for films grown on Si(111) was expected for two reasons. First, the surface-area-corrected surface recombination velocity (SRV) is significantly higher for (111) surfaces compared to (100), with the magnitude depending on a variety of factors including surface preparation and passivation. In general, the higher SRV is attributed to higher defect density, lower fixed charge in the passivation layer, different electron/hole capture cross sections, or some combination of these [72]. Second, the diffusion coefficient of O is higher in Si(111) compared to Si(100) [73], and the same is likely true for S (and possibly Zn) in Si as well. This would result in an increased amount of Si-S interactions, which produce recombination centers (electronic states within the Si bandgap).

All data sets in Figure 23 were fit to sigmoidal curves (solid black lines). This choice of fitting function was made empirically; however, the plateau of IRV at high and low values of absorption depth can be understood by considering the following. At long absorption depths ($>5*10^{-4}$ cm), the initial gradient in free carrier concentration near the ZnS/Si interface becomes small and approaches zero. Thus, the IRV becomes independent of absorption depth, and is limited by diffusion of free carriers toward the interface. The value of IRV at which each sigmoid plateaus, toward long absorption depth, is similar for all samples (between $4*10^4$ and $18*10^4$ cm/s). At short absorption depths, the IRV is proportional to the density of defect states that facilitate recombination. The recombination rate is limited, however, by the electron and hole capture cross sections as well as lifetimes of the trap states. As absorption depth decreases, free carriers are generated nearer to the interfacial defect states, but they are also generated with a larger gradient in FCC which causes an increased rate of diffusion toward the bulk [74]. Thus, there is a competition between recombination and diffusion that results in the plateau of IRV at short absorption depth.

The focus now shifts to free carrier dynamics occurring when absorption occurs in the ZnS films. In this case, free carriers are generated in the ZnS film and follow one of four pathways: (1) recombination in the ZnS film, (2) recombination at the ZnS/Si interface, (3) transfer into the silicon with heat generation, or (4) heterojunction-assisted impact ionization (HAII) at the ZnS/Si interface. Both (1) and (2) result in a decrease in experimentally measured IQE, while (3) results in an IQE of one and (4) results in an IQE > 1. In the event of (4), the primary carriers (photogenerated) as well as secondary carriers (generated by HAII) have the chance to either recombine at the ZnS/Si interface or diffuse toward the bulk (and persist through the timescale of the experiment). Because HAII occurs at the interface, the probability that the free carriers become trapped in interfacial defect states, and recombine, is significant. In the following, we show data from experiments where the excitation pulse photon energy is greater than the ZnS bandgap, and use simulations to de-convolute the contributions of recombination from those of HAII in order to extract the probability of HAII in each sample.

We start by using the information in Figure 23 to extrapolate the sigmoidal fits to values of shorter absorption depth. See Appendix B for the sigmoid fitting function and parameters. Figure 24 shows the sigmoidal fit for sample biii, which is extrapolated to shorter absorption depths of interest ($3.7*10^{-7}$ cm and $6.3*10^{-7}$ cm, which are denoted by vertical black dotted lines and correspond to photon energies of 4.64 eV (267 nm) and

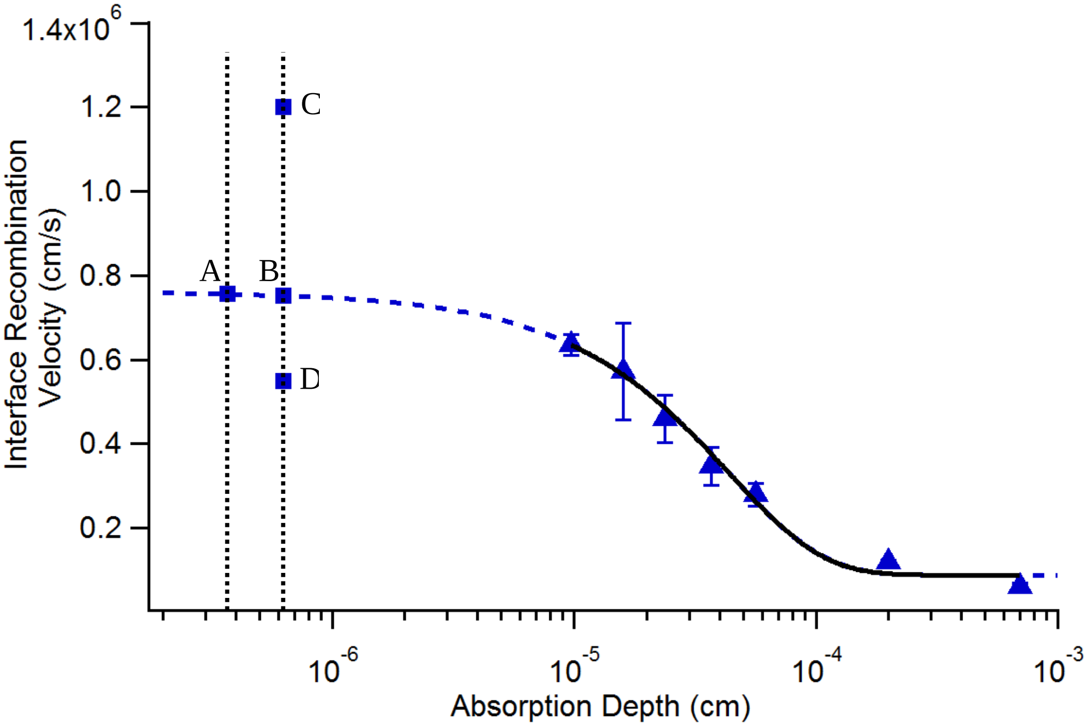

Figure 24. IRV versus absorption depth for sample biii. The sigmoidal fit (solid black line) is extrapolated to the absorption depths of 320 nm (point B) and 267 nm (point A) in silicon. Points C and D indicate the IRV at which the probability of HAII would be 100% and 0%, respectively, in order to explain the experimental data.

3.87 eV (320 nm), respectively). Using the extrapolated curve, we extract values of IRV at these absorption depths (points A and B) and use equation (13) to simulate a spectrum of IQE versus probe time delay. This simulation gives a result for the hypothetical case that the photons corresponding to those absorption depths are absorbed not in ZnS, but only in silicon (just as the rest of the excitation photons for the data in Figure 23 are). In practice, however, these photon energies are larger than the ZnS bandgap and therefore they *are* absorbed in ZnS. By comparing experimental and simulated results, the role of the ZnS absorber is isolated.

Figure 25 shows the simulated trace as well as experimental data for 320 nm excitation (absorption depth of $6.3*10^{-7}$ cm, point B) on sample biii. For clarity, the vertical axis is reduced to values of IQE between 0 and 0.5. The experimental data are clearly higher than the simulated result throughout all positive values of Δt, which indicates that absorption in the ZnS layer acts to enhance the IQE over the case where absorption occurs only in the Si. In fact, as discussed earlier, absorption in the ZnS layer introduces pathways for both free carrier annihilation (recombination) as well as generation (HAII). The observation of an enhancement in IQE due to the ZnS absorber indicates that the probability of HAII is greater than the combined probabilities of recombination in the ZnS layer and at the ZnS/Si interface.

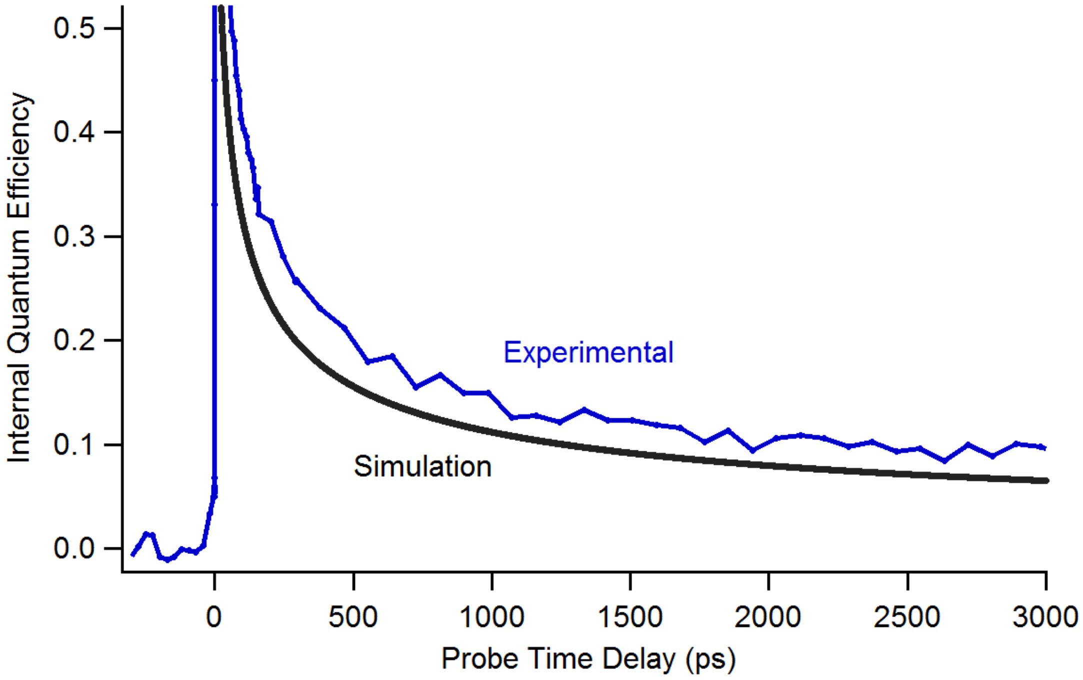

Figure 25. Internal quantum efficiency versus Δt for sample biii with 320 nm excitation. Experimental data are shown as well as the simulated result using the extrapolated value of IRV.

In order to quantify these conclusions, we calculate both a lower limit and a realistic estimate of the probability of HAII. The lower limit is calculated by quantifying the excess free carrier concentration (N_{ex}, the FCSC observed experimentally minus the simulated FCSC) present at long times. We use values from the probe time delay range of 2000 to 3000 ps ("long times") because at $\Delta t > 2000$ ps, free carriers are present only in Si and thus the calculated values of IQE are accurate (see Appendix C). At shorter Δt, free carriers are present in both ZnS and Si, and the calculated values of IQE may not be accurate due to a free carrier absorption cross section that is different for ZnS than for Si (we use $\sigma_{FCA,Si}$ for all calculations). The excess free carrier concentration, N_{ex}, is calculated from the simulated and experimental values of IQE as

$$N_{ex} = (IQE_{exp} - IQE_{sim}) * N_0 \tag{14}$$

where N_0 is the initial free carrier concentration and IQE_{exp} and IQE_{sim} are the experimental and simulated values of IQE between 2000 and 3000 ps, respectively. Taking the ratio of N_{ex} to N_0 and multiplying by 100% gives the percentage of initial free carriers that produced a secondary electron-hole pair through HAII. This is a lower limit because the calculation is performed using the long-time free carrier concentrations, after many of the carriers generated by HAII have presumably recombined. The results for each sample are summarized in Table 3.

The realistic estimate of the probability of HAII is calculated by scaling the simulated result by a multiplication factor such that it reproduces the long-time IQE of the experimental data. Figure 26 shows a log-log plot (for clarity) of the data in Figure 25

Table 3. Interface recombination velocities and probabilities of HAII for ZnS films deposited on Si via pulsed laser deposition.

Sample	Extrapolated IRV @ 320nm (*10^5 cm/s)	Probability of HAII		Limits of IRV	
		Lower Limit	Realistic Calculation	To obtain 0% HAII (*10^5 cm/s)	To obtain 100% HAII (*10^5 cm/s)
ai	5.35	3.5 %	30%	3.8	8.0
aii	4.05	4.3 %	35%	3.1	6.0
aiii	3.35	5.3 %	28%	2.4	5.0
bi	25.6	1.9 %	120%	12	24
bii	11.6	2.7 %	50%	7.2	15
biii	7.53	2.4 %	41%	5.6	11

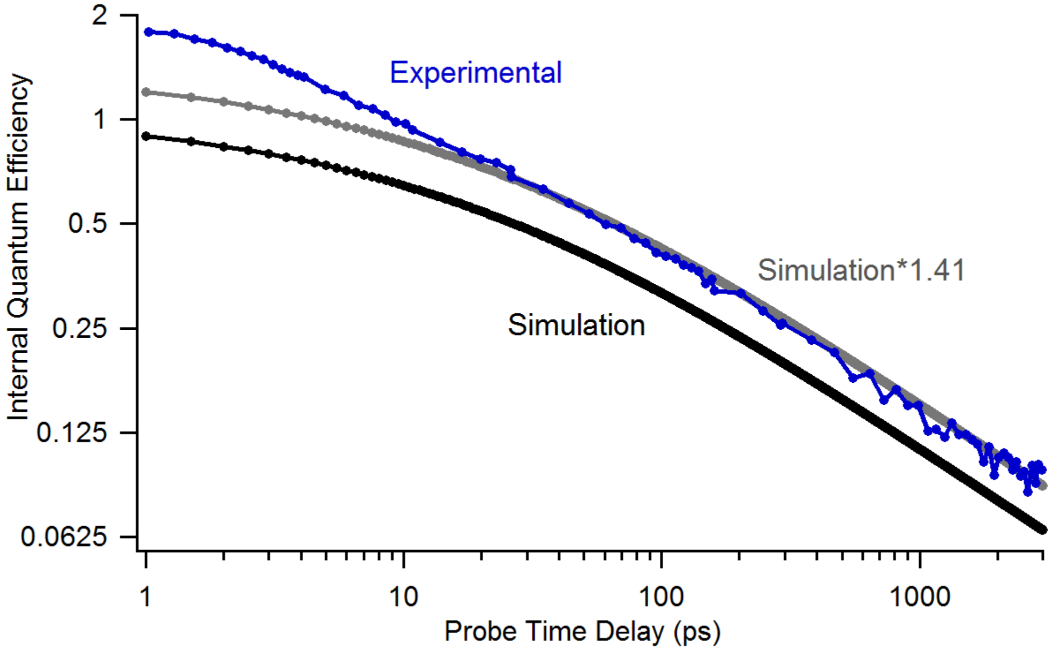

Figure 26. Log-log plot of IQE versus Δt for sample biii with 320 nm excitation. The simulated trace is scaled by a factor of 1.41 to reproduce the long-time IQE of the experimental data.

and includes a simulated trace which has been scaled by a factor of 1.41. Scaling the simulation by a multiplication factor is equivalent to simulating the result that would occur if the number of initial carriers was increased by the same factor. In other words, this process assumes that every free carrier generated by HAII is generated at Δt=0. The validity of this assumption is verified by calculating the amount of time it should take electrons generated in the ZnS film to transfer into the silicon substrate. The drift velocity of electrons is given by [75]

$$v_d = \mu_e * E \tag{15}$$

where v_d is the drift velocity, μ_e is the electron mobility, and E is the built-in electric field. If we assume a built-in field of 10 mV/nm [60] (assuming that half of the interfacial built-in field, 0.3 V, drops across the 30 nm of ZnS film) and an electron mobility of $100\,\frac{cm^2}{V*s}$ [76], we obtain a drift velocity of $1.0*10^7$ cm/s, and an electron would move 20 nm in about 200 fs. Even a built-in field lower by two orders of magnitude would result in a time of just 20 ps for electrons to move 20 nm. This suggests that electrons generated in the 20 nm ZnS films should quickly transfer into Si, and the above assumption is valid. The scaled simulated trace in Figure 26 is in good agreement with the experimental data at all times after about 30 ps, which provides further confidence in the assumption. There will additionally be diffusion that drives electrons and holes toward the silicon. This method also assumes that the free carriers generated by HAII are generated with a distribution given by the absorption depth of light. In practice, HAII-generated carriers exist initially at the ZnS/Si interface, and therefore have a higher chance to recombine than is assumed in this calculation. This could lead to an under-estimation of the probability of HAII.

Results of this analysis are summarized, for all six samples, in Table 3. We can now correlate material/interface properties (described in Chapter III and summarized in Table 1) to the probability of HAII. Of samples ai, aii, and aiii, we observe the highest probability of HAII for sample aii, which has a layer of epitaxial ZnS and contains no interfacial oxygen. Samples ai and aiii have similar HAII probabilities despite significant differences in interfacial oxygen content and film crystallinity. With similar HAII probabilities, the main difference between these samples is the magnitude of IRVs, which is higher for sample ai than sample aiii. For samples bi, bii, and biii, we observe the highest rate of HAII for sample bi, which is polycrystalline with no preferred crystal orientation (PCO) and no interfacial oxygen. The lowest rate of HAII is again observed on the sample with the highest interfacial oxygen content (sample biii). Comparing samples bi and bii, the main difference is a polycrystalline film with no PCO compared to a film grown epitaxially, respectively. The polycrystallinity of the film in sample bi leads to higher HAII, but higher IRV as well. We note that, although greater than 100% probability of HAII (observed for sample bi) is possible in this system ($E_{g,ZnS} > 3E_{g,Si}$), it would require either (1) a single band offset energy greater than twice the bandgap energy of silicon, or (2) both band offset energies equal to or greater than the bandgap energy of silicon. It is also possible that the probability of HAII was overestimated for this sample due to the high uncertainty in the data point in Figure 23b at the shortest absorption depth of $9.7*10^{-6}$ cm.

In general, it is unsurprising that interfacial oxygen leads to lower probabilities of HAII; if the oxygen exists as SiO_2 [71], then a potential barrier would exist as well (due to the large bandgap of SiO_2) and inhibit charge transfer from ZnS to Si (and thus inhibit

HAII). For thin layers of SiO_2 (< 2 nm), charge transfer could still occur via tunneling [77].

The rates of HAII are higher for films deposited on Si(111) compared to films on Si(100). This difference is attributed to the magnitudes of band offsets, as discussed earlier. For the ZnS/Si(111) interface, a large conduction band offset energy is expected, which is favorable compared to a large valence band offset energy due to the lower II energy threshold of electrons compared to holes. For the ZnS/Si(100) interface, a large valence band offset energy is predicted.

The largest source of error associated with these calculations lies in the extrapolation of the sigmoidal fits (IRV versus absorption depth). The range of extrapolation is significant; this was unavoidable due to the rapid increase in absorption coefficient (in Si) with photon energy in the range of photon energies near the ZnS bandgap (3.6 eV) [35]. We have calculated limits that demonstrate the sensitivity (or lack thereof) of our conclusions to the values of IRV extracted from the extrapolations. These limits are displayed for sample biii in Figure 24 by points C and D, and given for all samples in Table 3. If the actual value of IRV at the absorption depth of $6.3*10^{-7}$ cm was given by point C ($1.2*10^{6}$ cm/s), then the rate of HAII would have to be 100% in order to explain the experimental results. If the actual value of IRV was given by point D ($0.55*10^{6}$ cm/s), then the (unscaled) simulation would match the experimental results (at long times), and the rate of HAII would be zero. The predicted behavior in the extrapolated portion of the curves is qualitatively supported by the results in Appendix A, which demonstrate that, for unpassivated Si, slightly more surface recombination occurs with 267 nm excitation compared to 400 nm excitation.

Thin Films of ZnSe on Si Substrates

The ZnSe/Si material system is particularly attractive due to the bandgap of ZnSe (2.75 eV), which is large enough to promote HAII (with appropriate band offsets), and small enough to absorb a significant portion of the solar spectrum. For the ZnSe/Si(100) heterojunction, Xu et al. have measured a valence band offset energy (ΔE_{VB}) value of 1.55 ± 0.10 eV, with a small built-in field in the direction to move holes from ZnSe to Si [78]. Although ΔE_{VB} is smaller than the impact ionization threshold energy for holes in bulk silicon (1.8 eV), HAII occurs at an interface and thus the II threshold may be reduced due to the break in crystal symmetry.

ZnSe thin films (20 nm) deposited on Si(100) and Si(111) produced nearly identical results via the analysis presented earlier in this chapter. Therefore, Figure 27 shows data only for the 20 nm ZnSe film on Si(100). No interface recombination is observed for 626 nm excitation (this wavelength has photon energy below the ZnSe bandgap, and is absorbed exclusively in the silicon). For 400 nm excitation, which has photon energy above the ZnSe bandgap, a decrease in IQE is observed, suggesting recombination in the ZnSe film that annihilates more free carriers than the number produced via HAII. An exponential fit produces a time constant of 300 ps, which is consistent with previously reported values of the lifetime of free carriers in high quality ZnSe [79, 80].

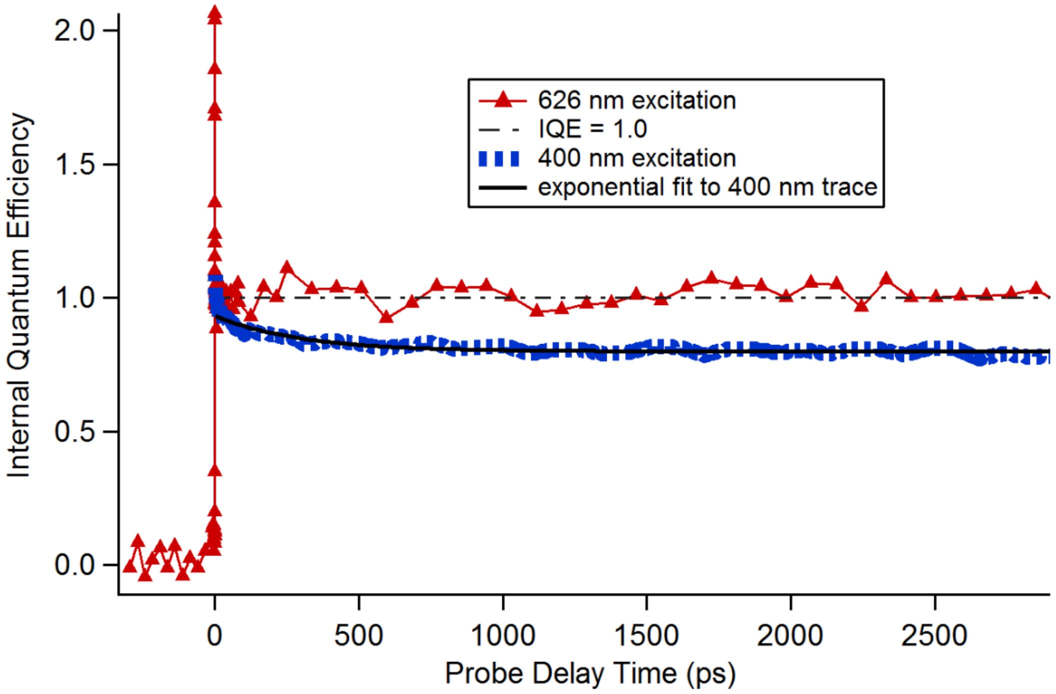

Figure 27. IQE versus Δt for a 20 nm ZnSe film on Si(100). The time constant of the exponential fit is 300 ps.

Conclusions

These results demonstrate that impact ionization occurs at the heterojunction between ZnS thin films and Si substrates for a variety of samples with different properties. The trends and magnitudes of IRV and HAII are consistent with theoretical expectations, and correlate to material properties in an intuitive way. The enhancement in probability of II for ZnS/Si samples compared to plain Si samples is attributed to control of the free carrier excess energy distribution via interfacial band offsets. With further optimization, some amount of interfacial oxygen may be useful for optimizing the IQE by balancing the effect on IRV with the effect on HAII.

The samples in this chapter were of very high quality, but their deposition was energy intensive due to the high temperatures and vacuum conditions required. Thus, the following chapter describes a method for depositing ZnS films that occurs near room temperature and pressure and requires a relatively simple experimental setup.

CHAPTER VI

O_2-FREE CHEMICAL BATH DEPOSITION OF ZINC SULFIDE THIN FILMS ON SILICON

In this chapter the chemical bath deposition (CBD) of ZnS thin films on Si substrates in an O_2-free environment is described. The CBD method is attractive due to the simplicity of the experimental setup combined with its ability to produce high quality films. The process was complicated by the fact that the materials are sensitive to O_2 dissolved in the chemical bath, as it causes a layer of SiO_2 to form at the ZnS/Si interface during deposition. As shown in Chapter V, interfacial oxygen decreases the probability of HAII and in the extreme case of >2 nm of interfacial SiO_2 it would likely prevent HAII completely. Degassing of solutions and an N_2 atmosphere were effective to minimize this oxidation, allowing deposition of ZnS films directly onto Si. Under these conditions, we examine film properties as they relate to reagent bath concentrations in order to obtain films with properties favorable for promoting HAII. The design of experiments as well as film deposition procedure was developed by myself, Brock Tillotson, and Frederick Moore. Films were deposited and characterized by myself, Brock Tillotson, and Amanda Siedschlag. Some material in this chapter will be published with co-authors Frederick G. Moore, Brock M. Tillotson, Amanda Siedschlag, Stephen D. Kevan, and Geraldine L. Richmond.

Introduction

The ZnS/Si materials analyzed in Chapter V were deposited by pulsed laser deposition, which produces high quality materials but is energy intensive due to the high temperature and vacuum conditions required during the deposition process. We therefore use the chemical bath deposition method, which requires a relatively simple experimental setup and occurs at near-room temperature and atmospheric pressure, to deposit ZnS thin films on Si substrates. This method is solution-based and can coat large surface areas with uniform, optically smooth thin films via the controlled reaction of precursors in a solution that contains a substrate [20].

The performance of CBD ZnS thin films depends predominantly on their morphological properties (e.g. crystallinity, texture, thickness, uniformity), which are challenging to control due to competing precipitation reactions in the bulk solution (homogeneous) and on the substrate surface (heterogeneous). These two precipitation reactions give rise to the two growth mechanisms commonly reported for CBD: cluster-by-cluster and ion-by-ion growth, respectively. In practice both mechanisms occur simultaneously, leading to compact films containing embedded colloidal particles [81].

Controlling which growth mechanism dominates (by altering growth parameters) is of primary interest, as it determines the structural and electronic properties of the films. This can be accomplished by controlling the rate of reaction, which depends on the effective concentrations of Zn^{2+} and S^{2-}. These can be controlled by adding a complexing agent and adjusting the solution pH, respectively. Zn^{2+} binds to ligands (e.g. hydrazine, citrate, ethylenediamine) which limit its reactivity according to the metal-ligand binding costant [82]. Similarly, thioacetamide decomposes to release S^{2-} at a rate that depends on the solution composition and pH [83, 84].

The growth of ZnS films by CBD is generally considered to proceed by the cluster-by-cluster mechanism, with colloidal ZnS aggregating both in solution and on the substrate [83, 85, 86]. Isolated ZnS nuclei (nanocrystallites) and aggregates of these nanocrystallites (clusters) both contribute to film growth. This mechanism was thoroughly reviewed and demonstrated by Bogush and Zukoski [87, 88] for the synthesis of silica particles, and has since been observed in the synthesis of ZnS powders and films [83, 85]. Though less common, there are also reports of ion-by-ion growth of ZnS films, which occurs upon direct interaction between surface sites and precursor species (containing Zn^{2+} and S^{2-}) [89, 90].

Experimental Details

Thin film depositions utilizing microwave heating were performed using chemical bath compositions adapted from the work by Nabiyouni et al. [20]. The bath contained a mixture of zinc acetate dihydrate (ZnAc), ethylenediamine (En), and thioacetamide (TAA) with the molar ratios 1:2:4, respectively. Each chemical bath maintained this molar ratio of reagents, while the absolute concentrations were varied. The highest bath concentration used was 0.042 M ZnAc, 0.084 M En, and 0.168 M TAA, and samples grown in this concentration were denoted type -1-. Samples deposited with concentrations reduced by two (0.021 M ZnAc, 0.042 M En, and 0.084 M TAA) were denoted type -1/2-, and so on. All depositions were performed at 80°C with stirring.

Prior to deposition, all solutions were degassed using the freeze-pump-thaw method. In order to prevent ZnS precipitation prior to film deposition, two solutions were prepared and degassed separately; one solution contained ZnAc and En, while the other contained TAA. Following degassing, the solutions were transferred to a glovebox with N_2 atmosphere. Degassed solutions and N_2 environments were used in order to minimize oxidation of the Si substrate surfaces. Indeed, the crystalline Si surfaces remained mostly un-oxidized throughout film deposition, as verified by time-of-flight secondary ion mass spectrometry (ToF-SIMS) and transmission electron microscopy (TEM).

The substrates utilized in this study were double-side polished <111> Si wafers (1 x 1.5 cm) of high purity (undoped, R > 15000 Ωcm). The wafers were subjected to the RCA standard clean [32] followed by etching in buffered oxide etch (BOE, 20:1) for 2 minutes, and finally oxidation in a tube furnace to grow a thermal oxide of approximately 100 nm. They were then transferred to a glovebox for further preparation in a N_2 atmosphere.

Immediately prior to deposition, the Si wafers were etched again in BOE, for 24 minutes, to remove the surface oxide layer. They were then placed in a 5 mL glass vial containing the ZnAc/En solution and stir bar. After adding the TAA solution, the vial was capped and transferred to the microwave heating apparatus. Each deposition consisted of 2 hours heating time. In order to increase the thickness of the films, subsequent depositions were performed using fresh chemical bath solutions.

Zinc acetate dihydrate (J.T. Baker, A.C.S. reagent grade), ethylenediamine (Fluka, puriss. grade), and thioacetamide (Sigma-Aldrich, reagent grade) were used as received. Reaction baths were heated using a Personal Chemistry Emrys Creator microwave with a maximum heating power of 90 W. Samples were imaged using a ZEISS Ultra-55 scanning electron microscope (SEM) with 5 kV accelerating voltage. Imaging and roughness analysis were performed using atomic force microscopy (AFM; Digital Instruments Veeco Multimode AFM with IIIa controller) in tapping mode. Elemental analyses were performed using a Cameca SX100 electron microprobe and an ION-TOF Model IV ToF-SIMS in depth profiling mode. A Titan 80-300 microscope operated at 300 kV was used for TEM cross section imaging. X-ray diffraction (XRD) measurements were performed in grazing incidence geometry using a Philips PANalytical X'Pert diffractometer with CuKα (1.54 Å) radiation. We have estimated the deformation of GI-XRD peaks by fitting the (111) diffraction peak to the sum of 3 Gaussian curves, and comparing the integrated area under each curve. This provides only an estimate of the magnitude of peak deformation. Colloidal ZnS particle sizes were determined by dynamic light scattering (DLS) measurements using a Malvern Zetasizer Nano ZS.

O_2-free Chemical Bath Depositions

All film depositions were performed with degassed solutions and under N_2 atmosphere (henceforth called 'air-free/degassed' conditions) to minimize oxidation of the silicon substrate. To investigate the effect that O_2 (dissolved in the chemical bath) has on the resulting ZnS films, we employ ToF-SIMS, TEM, and AFM. First, we investigate the composition of the ZnS/Si interface for films deposited in the air-free/degassed case as well as under standard atmospheric conditions. Using ToF-SIMS we have obtained an elemental analysis through the depth of each sample, and observe a reduction in ZnS/Si interfacial oxygen by a factor of 19 for the air-free/degassed case compared to the film deposited under atmospheric conditions (Figure 28). The quantity of SiO_2 remaining in the air-free/degassed case is observed in TEM cross sections of these films which show a thin, 1-2 nm SiO_2 layer between the silicon substrate and ZnS film in some areas, while in other areas little to no oxide is visible (Figure 29). Finally, we have deposited ZnS films under air-free/degassed conditions on both Si and SiO_2 substrates. It will be shown that there are significant differences due to the change in substrate composition.

Because the aqueous oxidation of silicon is catalyzed by dissolved O_2 [91], we expect that the N_2 atmosphere was contaminated with O_2, and that superior minimization of oxidation is possible. This could be important for the fabrication of devices utilizing the ZnS/Si hetero-interface, or of films that utilize the ZnS-Si lattice matching to achieve desired characteristics.

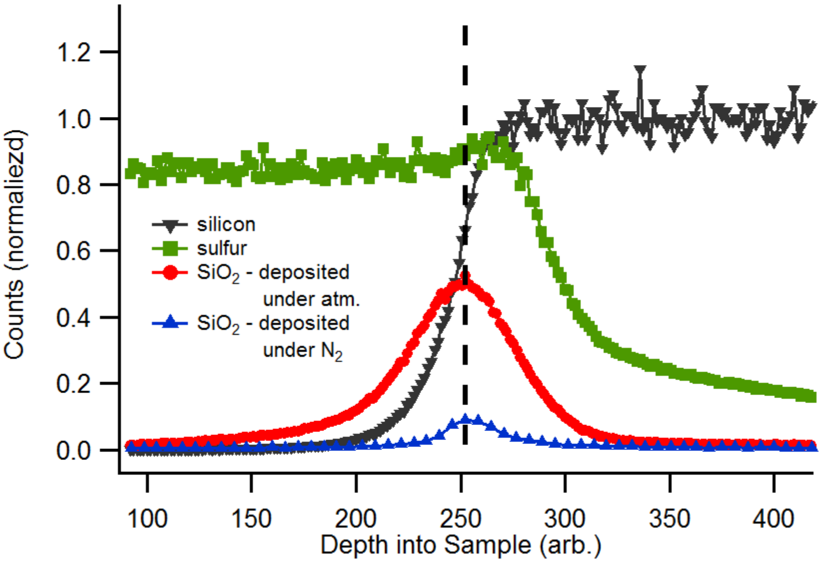

Figure 28. ToF-SIMS data showing SiO_2 levels at the ZnS/Si interface for samples grown under conditions identical in all ways except that one was deposited under atmospheric conditions (red circles) while the other was deposited under air-free/degassed conditions (under N_2, blue triangles). Reagent concentrations were 1/32 in both cases. The integrated area under the SiO_2 peak is 19 times larger for the film deposited under atmospheric compared to air-free/degassed conditions.

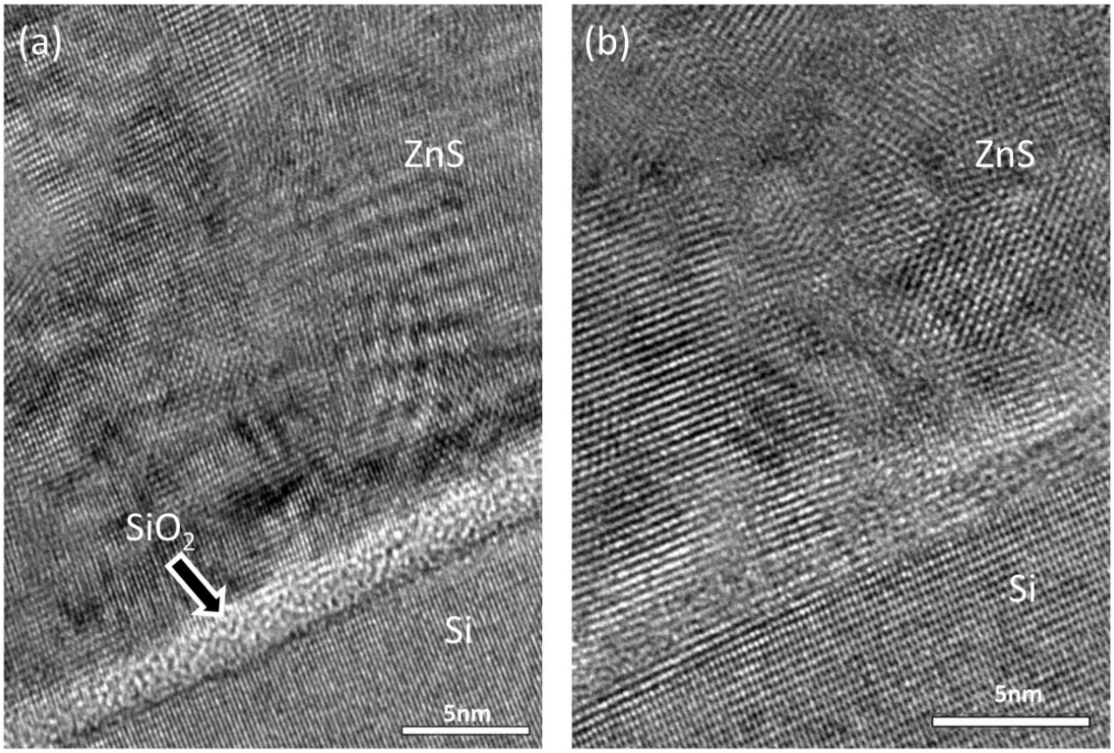

Figure 29. TEM cross section images of film -1/32- showing a 1-2 nm oxide layer between the silicon substrate and ZnS film in some areas (a), while in other areas little to no oxide is visible (b).

Structural Characteristics and Elemental Analysis

We have used grazing incidence x-ray diffraction (GI-XRD) to evaluate the structural characteristics of the ZnS thin films. Figure 30 shows the GI-XRD patterns for ZnS films deposited with different reagent concentrations. In each spectrum, three peaks are evident at 2θ values of approximately 28.6, 47.5, and 56.3 corresponding to the (111), (220), and (311) planes, respectively, of the cubic form of ZnS [92].

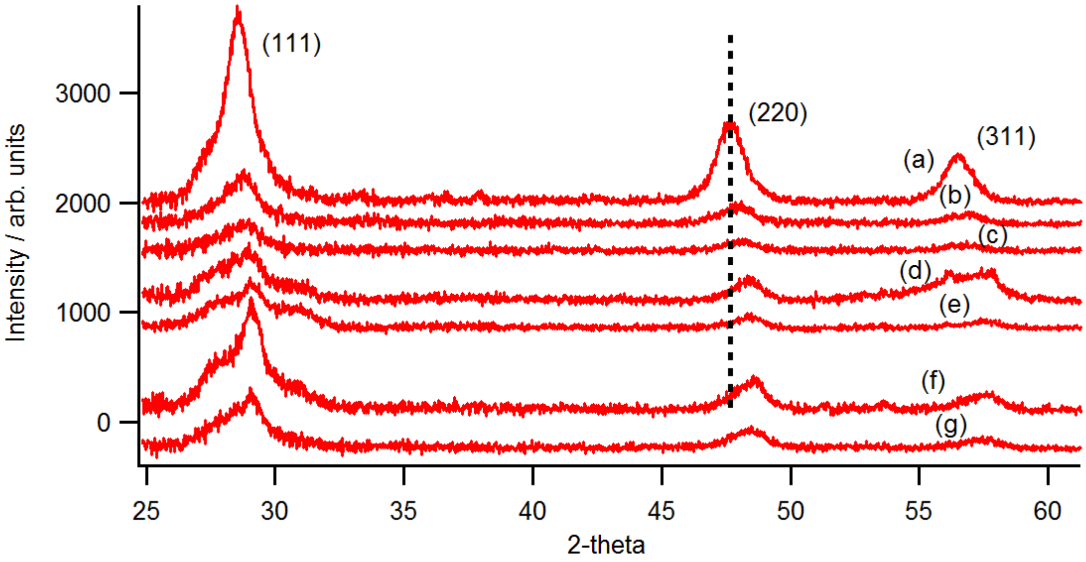

Figure 30. Grazing incidence x-ray diffractograms for samples (a) 1, (b) 1/2, (c) 1/4, (d) 1/8, (e) 1/16, (f) 1/32, and (g) 1/32 on thermally oxidized Si. The vertical dashed line is a guide to the eye, showing the shift in peak position.

Two trends emerge as the reagent bath concentrations are decreased (trace (a) → trace (f)): each peak shifts to higher values of 2θ, and also becomes irregularly shaped with increased intensity on the low-angle side of the peak (most obvious with the (111) peak). The shift in peak positions is caused by a compression of the crystal lattice, which can be explained by the partial substitution of oxygen for sulfur in the ZnS crystals [93]. Since O has a smaller van der Waals radius than S (152 pm vs 180 pm) [94], this substitution causes a contraction of the crystal lattice, and an increase in the diffraction angle 2θ. In order to determine elemental composition we have performed electron probe micro-analysis (EPMA) on each ZnS film, and summarize the results in Table 4. An increase in oxygen:sulfur and zinc:sulfur ratios with decreasing reagent concentrations is observed and consistent with this explanation. Assuming Vegard's law, which finds a

Table 4. Properties of ZnS thin films deposited at various reagent bath concentrations.

Sample	Zn:S ratio	O:S ratio	220 Peak Position	Fractional Peak Shift (arb.)	Grain Size (nm)	Thickness (nm)	Particle Size (nm)
-1-	1.05	0.11	47.66	0.36	4.5	200	40
-1/2-	1.14	0.20	47.91	0.34	3.8	100	35
-1/4-	1.13	0.40	48.04	0.46	4.0	50	30
-1/8-	1.23	0.42	48.33	0.86	4.3	50	30/coalesced
-1/16-	1.23	0.49	48.49	0.96	4.0	50	25/coalesced
-1/32-	1.22	0.59	48.60	0.95	4.0	50	coalesced
-1/32- on SiO_2	1.21	n/a	48.47	0.96	3.8	80	85

linear relationship between lattice parameters and composition [95], these findings account for the observed magnitudes of GI-XRD peak shifts.

The irregular peak shapes are characteristic of a deformation of the lattice near ZnS crystal grain interfaces. Atoms near grain interfaces experience a highly asymmetrical stress field relative to those in the core of the grain, and therefore we expect their spacing to be different as well. When the number of these interface atoms is comparable to the number of atoms in the core, their altered lattice spacing can affect the shape of XRD peaks [96]. In the present case, GI-XRD intensity is shifted to lower 2θ, relative to the center of the peak, indicating that the lattice near grain interfaces is expanded (tensile strain). We have estimated the magnitude of the shifted peak intensity, relative to the main peak intensity, for each film (Table 4, 'Fractional Peak Shift').

Since peak deformation is enhanced with lower reagent bath concentrations, we would expect a concurrent decrease in grain size due to the changing volume/surface ratio. However, the grain size within each film has been estimated using the Debye-Scherrer formula [97] and the properties of the 220 diffraction peak, revealing that grain size is relatively constant, within the range 3.8 - 4.5 nm, for each film (Table 4). Instead, the variation in grain interface stress is related to the film morphology and composition, as discussed below. There is also some GI-XRD intensity shifted to higher 2θ, however the integrated magnitude is small and fluctuates randomly. Thus, the reader is referred to previous reports of compressive stress in ZnS thin films [98, 99], and this is not discussed further.

We have observed that the identity of the substrate influences the morphological properties of ZnS films. Thus, we deposited a film on oxidized Si (SiO_2) using bath conditions identical to those used for a deposition on plain Si. This allowed us to observe a change in film morphology that was not due to different bath conditions (Figure 31). In the GI-XRD trace for the film deposited on SiO_2 (Figure 30g), we observe that the peak shift and deformation are similar to the film deposited on Si (Figure 30f). On the other hand, the film roughness and growth rate vary significantly from the film deposited on plain Si (Figure 31 and Figure 33). This indicates that the lattice strain is a result of either the change in reagent bath concentrations, or a change in morphology besides roughness. The following explanation suggests that both factors need to be considered.

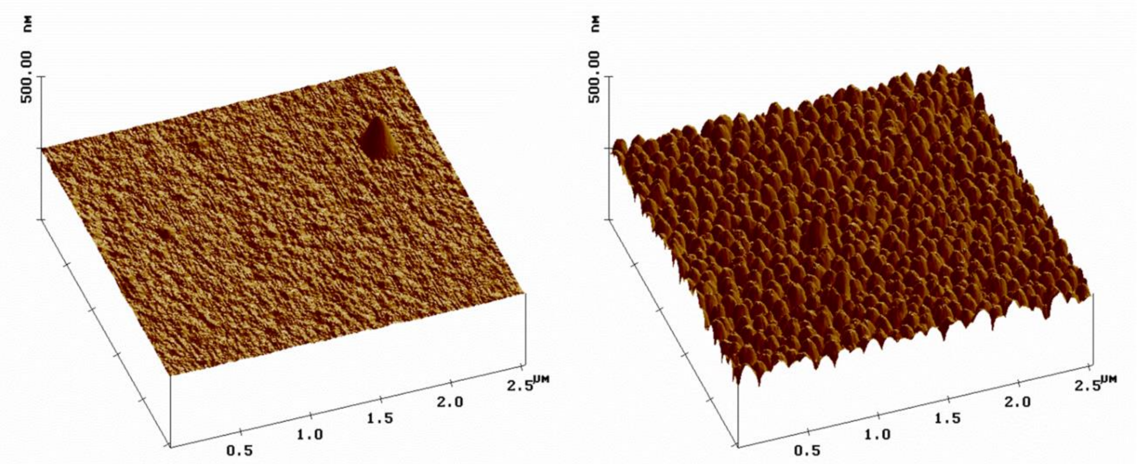

Figure 31. Atomic force micrographs of films deposited using 1/32 reagent bath concentrations on (a) silicon and (b) thermally oxidized silicon. All bath conditions were identical, thus the differences in morphology are due to the change of substrate.

According to a grain boundary model developed by Doljack [100] and extended to ZnS films [98], the close proximity of crystallite grains in a film results in tensile stress due to attractive interatomic forces between grains. Moreover, this effect is enhanced by the incorporation of oxygen impurities due to the smaller space requirement of O relative to S. It follows that the magnitude of stress depends on the inter-grain distance, and therefore on cluster size. By examining SEM images of each film (Figure 32), we have estimated the cluster size in each film (Table 4). We see that the peak deformation for the film deposited on SiO_2 is greater than for films with smaller cluster sizes, and similar to the films with coalesced clusters (infinite cluster size). Based on this we conclude that grains residing in the interior of a cluster or continuous film experience tensile stress due to close proximity with neighboring grains, whereas grains residing on the interface of a cluster do so to a lesser extent.

Due to the high oxygen content in the underlying SiO_2 layer, we could not measure the oxygen content in the film deposited on SiO_2. However, we note that the Zn:S ratio is similar to that of the film deposited on plain Si, suggesting a similar oxygen content as well.

Figure 32 (next 2 pages). SEM images of: sample -1- (a) top-down after 2 hours growth time, (b) top-down after 4 hours growth time, and (c) cross section image after 4 hours growth time; sample -1/2- (d) top-down after 2 hours growth time, (e) top-down after 4 hours growth time, and (f) cross section image after 4 hours growth time; sample -1/4- (g) top-down after 2 hours growth time, (h) top-down after 4 hours growth time, and (i) cross section image after 4 hours growth time; sample -1/8- (j) top-down after 2 hours growth time, (k) top-down after 8 hours growth time, and (l) cross section image after 8 hours growth time; sample -1/16- (m) top-down after 2 hours growth time, (n) top-down after 10 hours growth time, and (o) cross section image after 10 hours growth time; sample -1/32- (p) top-down after 2 hours growth time, (q) top-down after 12 hours growth time, and (r) cross section image after 12 hours growth time.

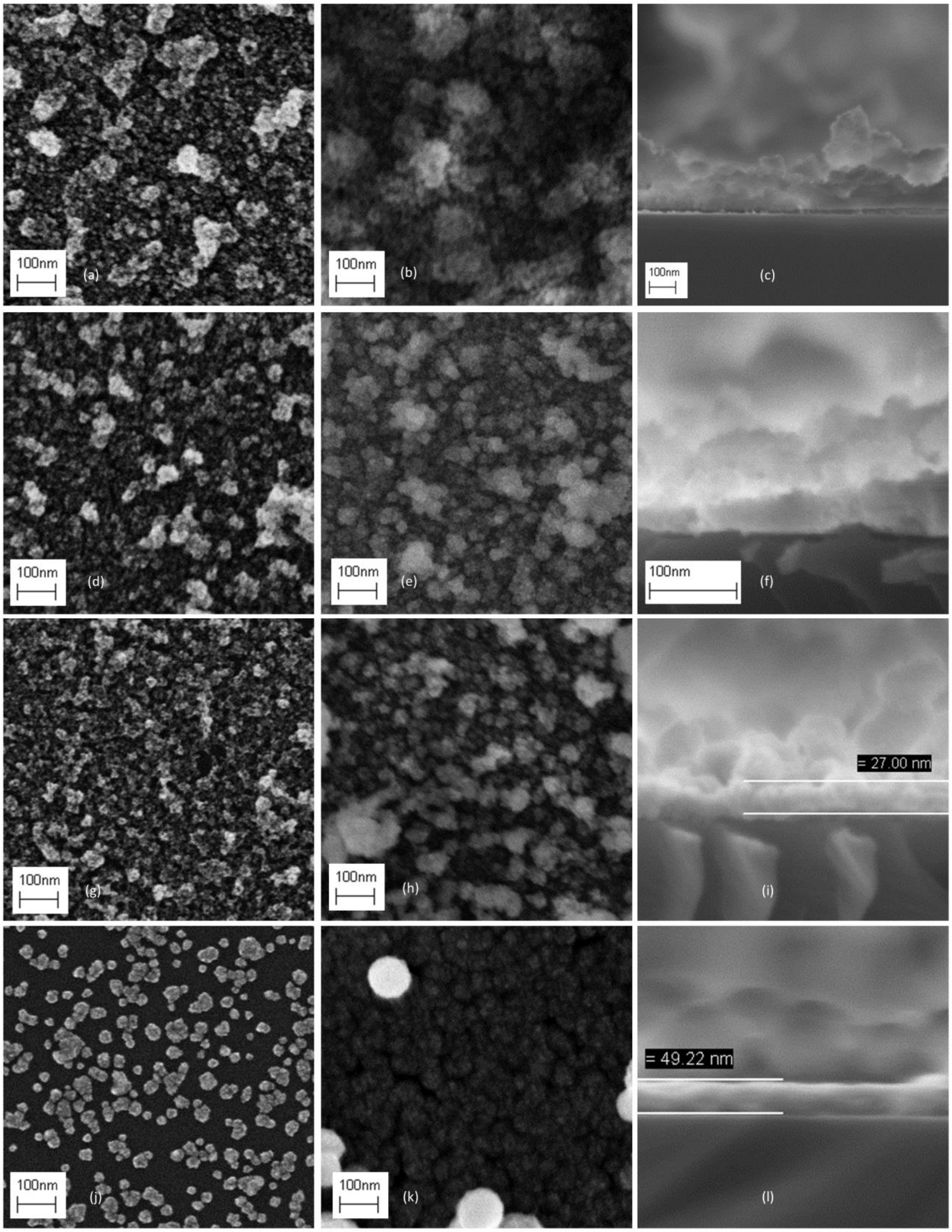
100nm
(a)
100nm
(b)
100nm
(c)
100nm
(d)
100nm
(e)
100nm
(f)
= 27.00 nm
100nm
(g)
100nm
(h)
(i)
= 49.22 nm
100nm
(j)
100nm
(k)
(l)

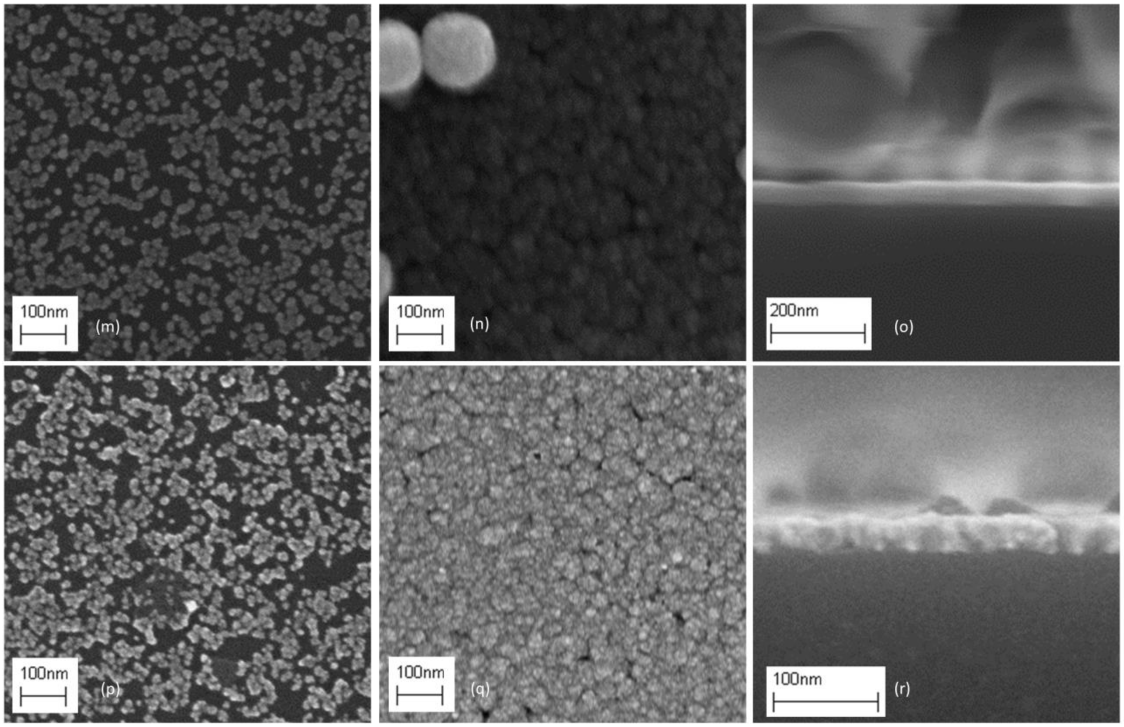

Morphology and Growth Behavior

We have used SEM to investigate the morphology and growth rate of ZnS films via surface and cross-sectional images. Figure 32 shows SEM surface and cross sectional images for each sample. For brevity the discussion focuses on samples -1/2- and -1/32-, since samples -1- and -1/4- are similar to -1/2-, and samples -1/8- and -1/16- are similar to -1/32-. For each film, we have imaged the surface after 2 hours of growth and again once the film has reached its final thickness (≥40 nm, Table 4). Figure 32d (sample -1/2-) shows a continuous film (full surface coverage) composed of 30-40 nm clusters after two hours, and little change in appearance with further growth time (Figure 32e). From the cross-sectional image (Figure 32f), the film appears granular with non-uniform thickness. In contrast, Figure 32p (sample -1/32-) shows a non-continuous layer of 15-25 nm clusters after two hours. With additional growth time, surface coverage increases and the clusters appear to grow together, producing the smooth yet somewhat granular surface morphology shown in Figure 32q. From the cross-sectional image (Figure 32r), the film appears homogeneous with uniform thickness.

Thickness values for each film have been estimated from the SEM cross-section images and used to calculate growth rates, which are plotted in Figure 33 Also plotted is film roughness, as determined by AFM, which follows the same trend: increasing linearly with reagent bath concentrations. The most striking result is the low roughness observed for films deposited at the lowest reagent bath concentration. Examining film -1/32-, we observe that growth begins with ~20 nm particles dispersed across the Si surface (Figure 32q). If the final film consisted of these 20 nm (spherical) particles stacked side-by-side, to form the smoothest film possible, the RMS roughness would be 3.1 nm. If instead we consider the constituent particles to be 4.0 nm (and again spherical), which is the grain size determined by GI-XRD, we calculate an RMS roughness of 0.63 nm, which is slightly below the actual value of 1.3 nm. These calculations suggest that at low bath reagent concentrations there exists a mixed growth mode, in which both clusters and individual ZnS nanocrystallites contribute to film growth. At higher reagent bath concentrations, however, the high roughness and granular appearance suggest film formation predominantly from clusters of nanocrystallites that have aggregated in solution before attaching to the substrate.

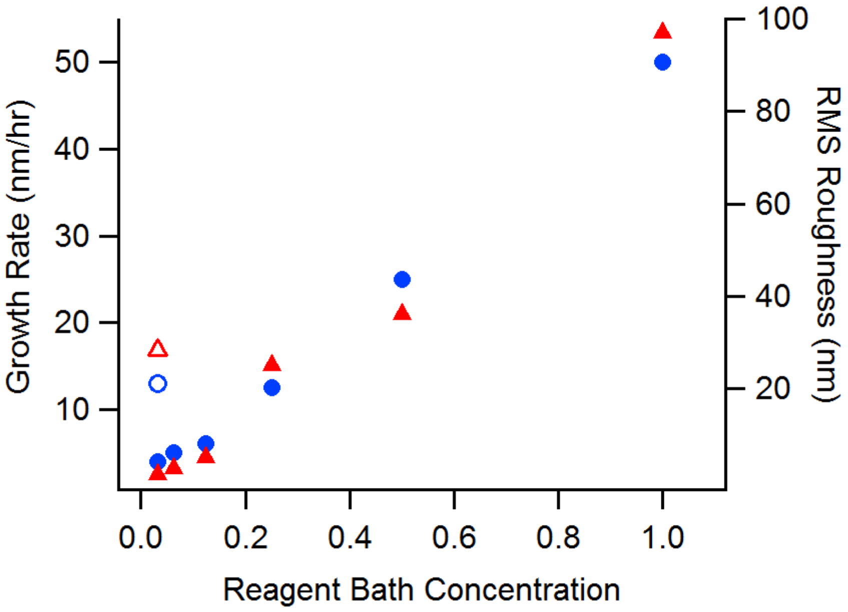

Figure 33. Film growth rate (circles) and RMS roughness (triangles) increase linearly with reagent bath concentrations. The shaded shapes are for films deposited on Si, while the open shapes are for the film deposited on SiO_2.

We have used dynamic light scattering (DLS) to investigate the size of colloidal particles in each chemical bath after 2 hours of film deposition. The results, summarized in Table 5, indicate an enhanced degree of aggregation for higher reagent bath concentrations. For the concentrations ≥ 1/4, we see particle sizes of 5-8 µm in solution, but these large particles were not observed in SEM imaging of the film surfaces. For relative concentrations ≤ 1/8, we see smaller particle sizes of 0.4-1.5 µm in solution, which *were* observed in SEM imaging of the film surfaces. In every case, some 0.1 – 1.5 µm particles have adhered to the substrate surface, and sit atop the compact film underneath. Thus, higher reagent bath concentrations result in larger colloidal particles, but the size adhered to film surfaces does not increase beyond about 1.5 µm. This is due

Table 5. Particle sizes in solution and within films.

Bath Concentration	Particle size in solution (μm)	Particle size in film (μm)
1	6.5	0.1 – 0.5
1/2	7.5	1.0 – 1.5
1/4	5.6	0.5 – 1.5
1/8	1.3	0.5 – 1.5
1/16	0.4	0.1 – 0.5
1/32	0.7	0.1 – 1.0

to the decreasing surface energy with increasing particle size, which limits the size of particle that will attach to the film [101].

Electronic Characterization

Studies of the electronic properties of these films, using the laser technique detailed previously, revealed low IRVs but no evidence of HAII. As representative samples, films -1/2- and -1/32- are discussed here. Due to the extremely low values of IRV in these samples, we cannot quantify IRV at most excitation wavelengths and therefore the analysis used on ZnS films in Chapter V is not applicable. Instead, we simply look for enhancement in the IQE for photon energies above the ZnS bandgap compared to photon energies below the ZnS bandgap. If absorption in the ZnS leads to HAII, then the experimentally observed enhancement in IQE between 267 nm and 400 nm will be greater than what would be observed in plain Si (a factor of 1.25; IQE(Si,267 nm)/IQE(Si,400 nm) = 1.25).

Zero IRV was measured for both samples at 800 nm excitation. With 400 nm excitation, both films exhibit some recombination, reducing the IQE to approximately 0.8 by Δt = 3000 ps (solid lines in Figure 34). With 267 nm excitation, the IQE is decreased for sample -1/32- (inverted triangles in Figure 34), but is enhanced for sample -1/2- (triangles). However, the IQE for sample -1/2- is enhanced by a factor of only 1.22, which is less than the enhancement in plain Si. Thus, we conclude that recombination in these ZnS films annihilates more free carriers than are produced by HAII.

The low IRVs in these samples probably results from the interfacial oxygen content as well as low temperature deposition conditions, which mitigate interdiffusion of Zn, S, and Si (thus also mitigating the number of electronic states within the Si bandgap). The high recombination rates within the ZnS films likely occur due to the small grain size

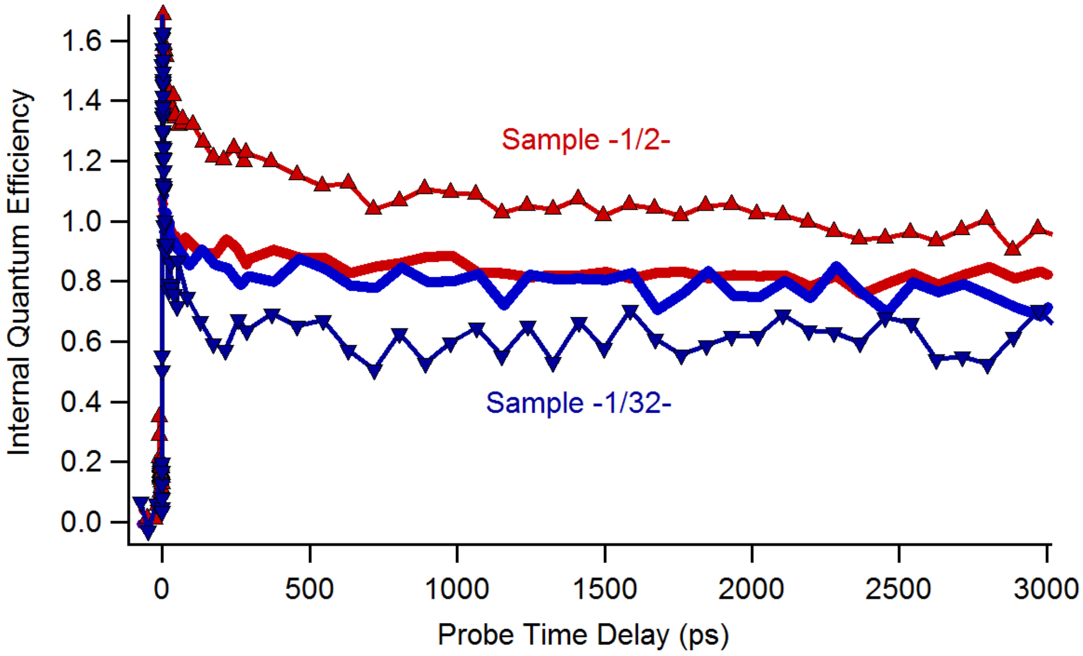

Figure 34. Internal quantum efficiency versus Δt for samples -1/2- and -1/32-, deposited by chemical bath deposition, with 400 nm (solid lines) and 267 nm (triangles) excitation.

(4 nm) of constituent crystallites, which produce a high density of ZnS surface states that promote non-radiative recombination.

Conclusions

We have documented the changes in growth behavior, morphology, composition, and interface stress that result from changing reagent concentrations in the O_2-free CBD of ZnS thin films. Degassing of the solutions and an N_2 environment was effective to minimize oxidation of the Si substrate, which could be crucial for the functioning of devices/processes utilizing the ZnS/Si interface, including HAII. Due to the low temperature growth conditions as well as some interfacial oxygen content, the IRVs measured on these samples were very low. However, due to significant recombination in the ZnS layers, there was no evidence for HAII. Nevertheless, this method demonstrates the utility of the O_2-free CBD method for minimizing oxidation of the silicon substrate, and producing materials at low cost that could be optimized for better performance.

CHAPTER VII

CONCLUSIONS

The laser technique detailed in this dissertation is a new and powerful tool for the analysis of free carrier dynamics in semiconductors. The experimental details and theoretical considerations of this technique, which combines free carrier absorption and reflection spectroscopies, were discussed in Chapter II. Chapter III includes synthesis details and structural characterization of the ZnS/Si and ZnSe/Si samples that were analyzed in Chapter V. Special attention was given to material parameters that were expected to affect the rate of free carrier recombination as well as heterojunction-assisted impact ionization (i.e. ZnS/Si interfacial oxygen content, film crystallinity, band offsets). In Chapter IV, the technique detailed in Chapter II was applied to the analysis of free carrier dynamics in silicon. Special attention was paid to the implementation of the experimental technique; specifically, the importance of detection of both the reflected and transmitted portions of the probe beam was emphasized and demonstrated. By normalizing the calculated free carrier concentrations to absorbed excitation photon flux, the internal quantum efficiency (in Si) for three different excitation wavelengths was calculated. By varying the excitation intensity, it was found that the free carrier absorption cross section in silicon is dependent upon free carrier concentration, and a model was developed to quantify this relationship. In Chapter V this model was used to de-convolute the contributions of recombination and enhanced absorption in spectra from ZnS/Si samples. It was found that ZnS/Si interface recombination velocity depended on the initial distribution of free carriers, which depended on excitation pulse photon energy.

Quantifying this relationship allowed the simulation of spectra, which were compared with experimental results in order to extract the probability of HAII in various ZnS/Si materials. The results showed that impact ionization occurs with significantly enhanced rates (versus plain Si) at the unbiased heterojunction of both ZnS/Si(111) and ZnS/Si(100). This demonstrates proof-of-principle that the heterojunction between two semiconductor absorbers can promote impact ionization, presumably due to control of the free carrier excess energy distribution via interfacial band offsets. The rates of both interfacial recombination and HAII depended on material properties including ZnS/Si interfacial oxygen content and film crystallinity. In Chapter VI, an O_2-free chemical bath deposition method was demonstrated for the deposition of ZnS films on Si. This method is attractive due to the simplicity of experimental setup and mild deposition conditions (near room temperature and pressure). Oxidation at the ZnS/Si interface, which is detrimental to the probability of HAII, was minimized by using degassed solutions and performing the depositions in a N_2 environment. Although there was no evidence of HAII in these samples, the study demonstrated the utility of the O_2-free CBD method for minimizing oxidation of the substrate and/or nucleating phases during film deposition.

This proof-of-principle demonstration of HAII at the unbiased ZnS/Si heterojunction paves the way for the development of PV materials that utilize this phenomenon to enhance photovoltaic efficiency. The bandgap energy of ZnS is too large to effectively absorb the solar spectrum; a suitable material system must be found which satisfies these requirements: (1) the harvester absorbs some portion of the solar spectrum, (2) at least one of the harvester/host band offset energies is equal to or greater than the host bandgap energy, and (3) harvester/host interface recombination is minimized. A system in which HAII outweighs recombination in the harvester and at the harvester/host interface would result in an increased photocurrent and an enhanced PV efficiency. For silicon solar cells, the increase in efficiency could be as large as about 11% (increase from 31% to 42% conversion efficiency), in the limit of no additional recombination. One promising material combination is thin films of ZnSe on Si substrates. The bandgap of ZnSe (2.7 eV) is small enough to absorb a significant portion of the solar spectrum, and large enough to provide suitable band offset energies with silicon. No evidence of HAII was detected in the ZnSe/Si samples studied in this dissertation; however, they demonstrated some attractive characteristics. The lifetime of free carriers in ZnSe was approximately 300 ps, which should allow free carriers time to diffuse/drift into the Si substrate. Moreover, ZnSe/Si interface recombination was below the detection limit, even for photon energies near (slightly below) the ZnSe bandgap energy. If the ZnSe/Si band offset energies were optimized to promote HAII (by δ -doping the interface to maximize ΔE_{CB}), this system could result in enhanced rates of IQE due to the lack of recombination at the ZnSe/Si interface. Finally, we note that the harvester need not be in the form of a thin film. A nanostructured film or embedded harvester may provide some advantages.

APPENDIX A

SURFACE RECOMBINATION IN ETCHED SILICON

Si(100) samples with thermal oxide passivation were compared to Si samples which had been freshly etched with an HF solution, leaving a surface passivated mostly by Si-H. Figure 35 shows the spectra for these samples with three different excitation wavelengths. In every case, we expect (based on previous results, see Chapter IV) no recombination in the thermally oxidized samples. For 800 nm excitation, no recombination is observed in the etched sample, due to the long absorption depth of 800 nm. For 400 nm and 267 nm excitation, some surface recombination is observed. The magnitude of decrease in IQE follows the trend 267 nm > 400 nm > 800 nm, as expected

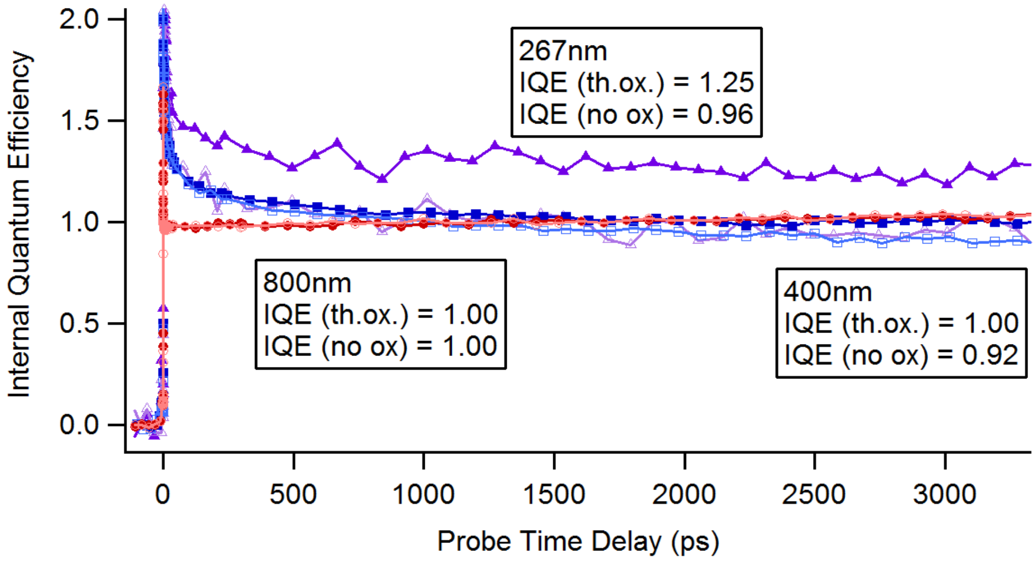

Figure 35. Internal quantum efficiency versus Δt for thermally oxidized and etched silicon at three different excitation wavelengths.

due to the absorption depths for these excitation wavelengths (see Table 2). This result verifies that more recombination occurs for 267 nm excitation than for 400 nm excitation, which lends support to the extrapolation of the sigmoidal fit in Chapter V.

APPENDIX B

SIGMOID FIT FUNCTION EQUATION AND PARAMETERS

Plots of interface recombination velocity versus excitation beam absorption depth were fit in IGOR Pro using the sigmoidal function

$$y = base + \left\{ max / \left(1 + exp\left(\frac{(half - x)}{rate} \right) \right) \right\}$$

Parameters from the fits of the data sets for each sample are presented in Table 6.

Table 6. Sigmoid fit parameters for each ZnS/Si sample analyzed in Chapter V.

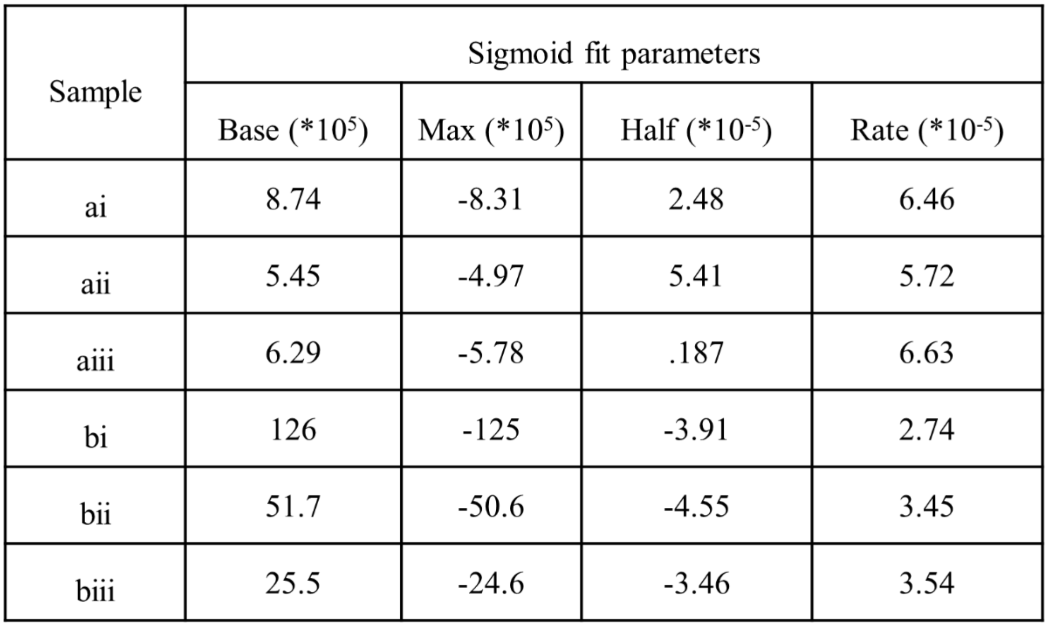

Sample	Sigmoid fit parameters			
	Base (*10^5)	Max (*10^5)	Half (*10^{-5})	Rate (*10^{-5})
ai	8.74	-8.31	2.48	6.46
aii	5.45	-4.97	5.41	5.72
aiii	6.29	-5.78	.187	6.63
bi	126	-125	-3.91	2.74
bii	51.7	-50.6	-4.55	3.45
biii	25.5	-24.6	-3.46	3.54

APPENDIX C

FREE CARRIER DYNAMICS IN ZINC SULFIDE

In order to characterize free carrier dynamics within (exclusively) the ZnS thin films, an 80 nm ZnS film on Si(100) was analyzed. The IRV versus absorption depth is shown in Figure 36. The trend is similar to the 20 nm films on Si(100), but the magnitudes of IRV are slightly lower. Besides the increased thickness compared to the 20 nm films, the 80 nm film also took 4x longer to deposit. This could have an effect similar to annealing, which has been found to reduce the density of interfacial defect states [70].

Figure 37 shows the IQE for 267 nm excitation on the 80 nm ZnS film on Si(100).

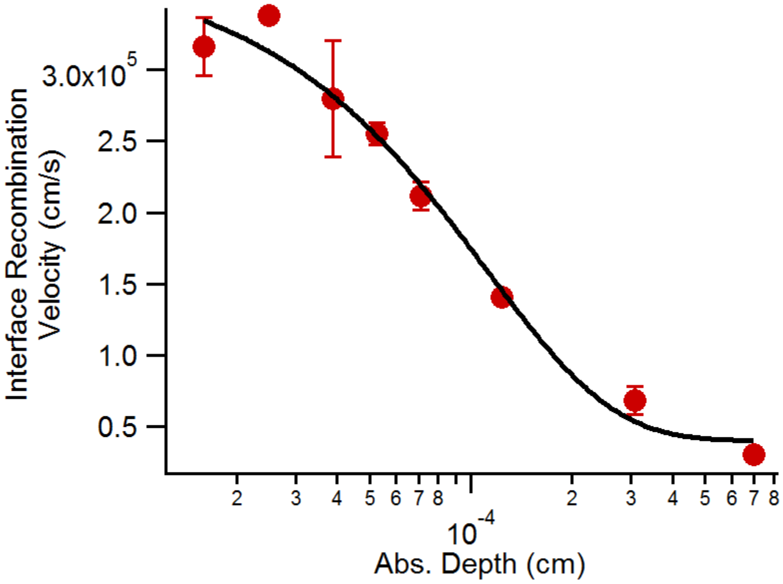

Figure 36. Interface recombination velocity versus absorption depth for an 80 nm ZnS film on Si(100). The solid black line is a sigmoidal fit.

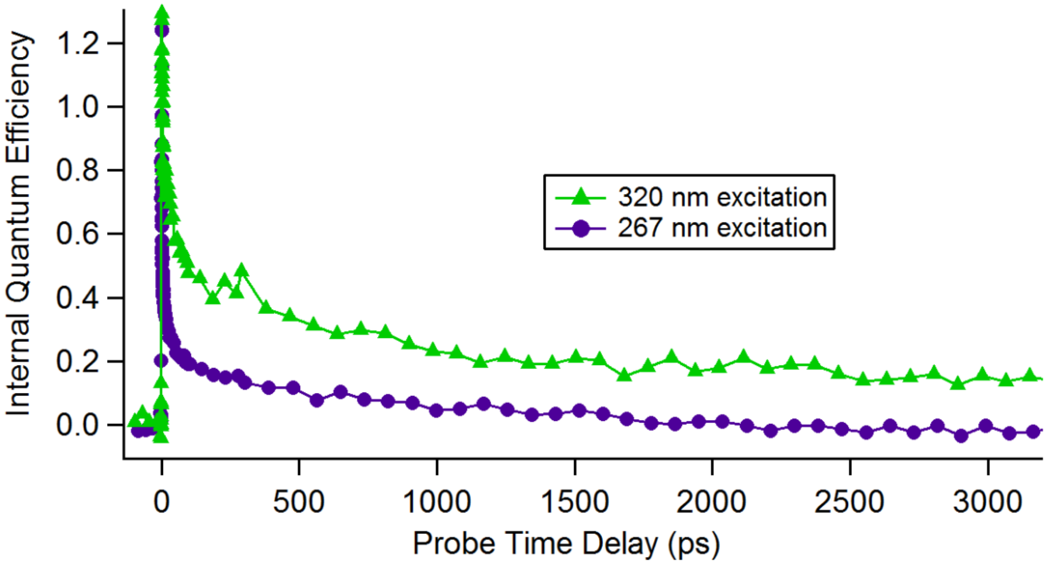

Figure 37. Internal quantum efficiency versus Δt for an 80 nm ZnS film on Si(100) with 320 nm and 267 nm excitation.

The IQE decays to zero by about 2000 ps and remains zero thereafter, which suggests that the absorption depth for 267 nm light in ZnS is much less than 80 nm and few or no free carriers reach the silicon before recombining. Moreover, this result indicates that no free carriers remain in the ZnS layer after 2000 ps, which is assumed true for the 20 nm films as well.

The effect of the difference in absorption depth (in ZnS) between 267 nm and 320 nm excitation is also demonstrated in Figure 37, which shows spectra for both excitation wavelengths on the 80 nm ZnS film. The longer absorption depth of 320 nm compared to 267 nm results in a higher long-time IQE due to excitation of free carriers in Si and in ZnS near to the ZnS/Si interface (where they are able to move from ZnS to Si and undergo HAII).

APPENDIX D

FIELD EFFECT PASSIVATION VIA SiO_2 OVERLAYERS

SiO_2 layers of two different thicknesses were deposited onto samples ai, aii, bi, and bii in an attempt to reduce ZnS/Si IRV via field effect passivation. The results of analysis of these four samples with 26 nm and 95 nm SiO_2 over-layers are summarized in Figure 38. For samples ai and aii, the SiO_2 layers slightly increased the IRV in all cases except for the 26 nm SiO_2 layer on sample ai. For samples bi and bii, the SiO_2 layers reduced IRVs in every case.

The effect of SiO_2 overlayer on ZnS/Si IRV must be through field effects because the SiO_2 is deposited on top of the ZnS film and thus is spatially separated from the ZnS/Si interface. Field-effect passivation affects the IRV by attracting one charge carrier while repelling the other. Recombination at the interface is maximized when the ratio of electron to hole concentrations at the interface is equal to the ratio of hole to electron capture cross sections, which makes the probability of capture of electrons and holes approximately equal [102, 103]. For SiO_2 layers, fixed negative charges (SiO^- groups) can develop at the SiO_2/air interface, and within the SiO_2 layers, due to deprotonation of SiOH groups and loss of H^+ via electron capture and atomic H evolution [104, 105]. This fixed negative charge would attract holes, which typically have lower capture cross sections than electrons, and increase the IRV. Positive fixed charge in SiO_2 layers, which would repel holes and attract electrons (thus reducing the IRV) has also been discussed [102, 106].

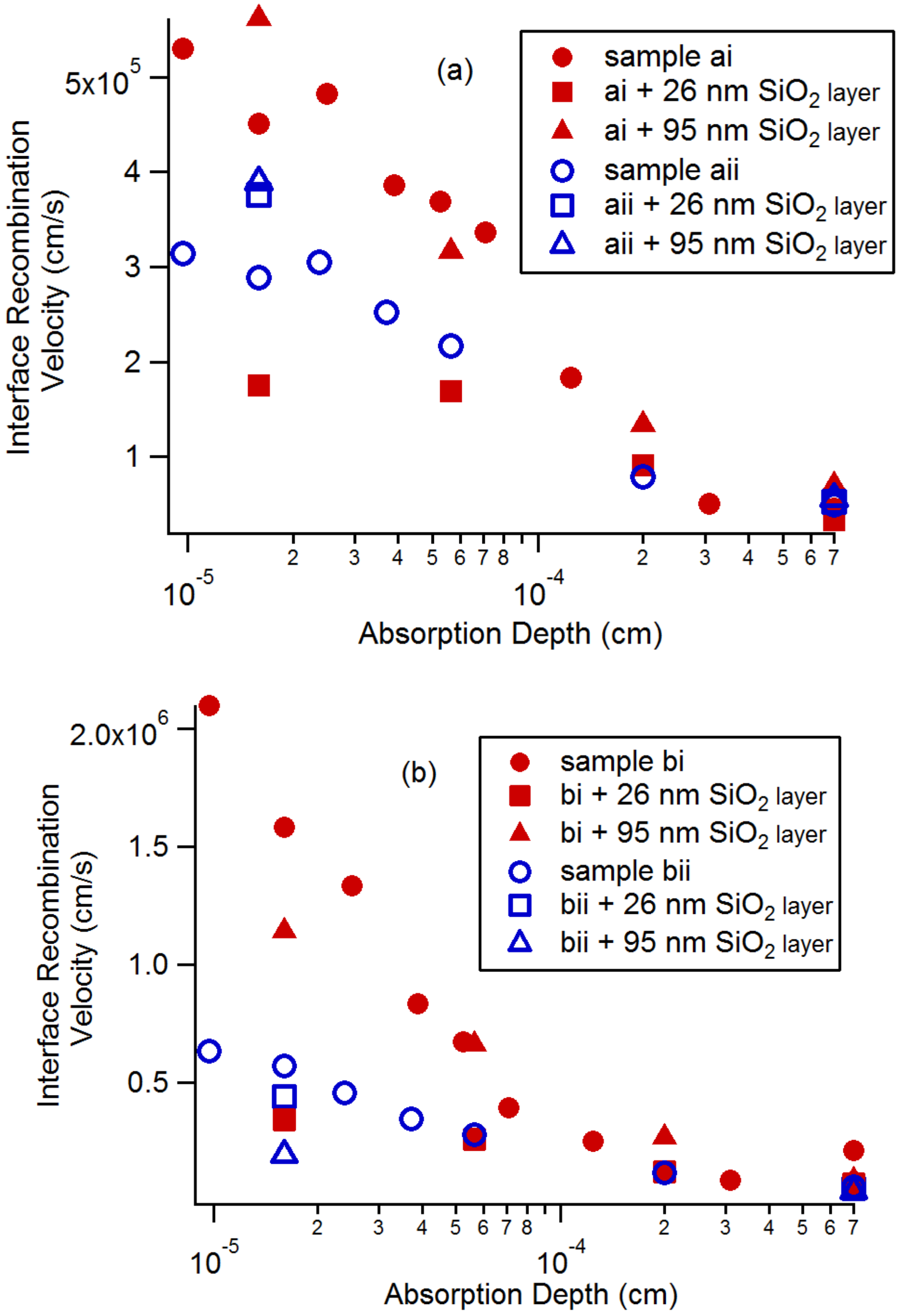

Figure 38. Interface recombination velocity versus absorption depth for ZnS/Si samples with SiO_2 overlayers. (a) shows samples ai and aii with 26 nm and 95 nm SiO2 overlayers. (b) shows samples bi and bii with 26 nm and 95 nm SiO2 overlayers.

The results shown here reveal either a small increase or significant decrease in IRV upon deposition of SiO_2 overlayers. Since the ratio of electron to hole capture cross sections for ZnS/Si interfacial defect states is high (>1) [71, 107], the decrease in IRV suggests a positive fixed charge either in the SiO_2 layer or at the ZnS/SiO_2 interface. With the exception of sample bii, the 26 nm SiO_2 layer always caused a greater decrease in IRV than the 95 nm layers, suggesting that the positive charge exists near the SiO_2/air interface (versus at the ZnS/SiO_2 interface).

REFERENCES CITED

[1] D. McCollum, V. Krey, K. Riahi, P. Kolp, A. Grubler, M. Makowski, N. Nakicenovic, Climate policies can help resolve energy security and air pollution challenges, Climatic Change, 119 (2013) 479-494.

[2] D.L. McCollum, V. Krey, K. Riahi, An integrated approach to energy sustainability, Nature Clim. Change, 1 (2011) 428-429.

[3] M. Meinshausen, N. Meinshausen, W. Hare, S.C.B. Raper, K. Frieler, R. Knutti, D.J. Frame, M.R. Allen, Greenhouse-gas emission targets for limiting global warming to 2 degrees C, Nature, 458 (2009) 1158-1162.

[4] Cubasch, U., D. Wuebbles, D. Chen, M.C. Facchini, D. Frame, N. Mahowald, and J.-G. Winther, 2013: Introduction. In: Climate Change 2013: The Physical Science Basis. Contribution of Working Group I to the Fifth Assessment Report of the Intergovernmental Panel on Climate Change [Stocker, T.F., D. Qin, G.-K. Plattner, M. Tignor, S.K. Allen, J. Boschung, A. Nauels, Y. Xia, V. Bex and P.M. Midgley (eds.)]. Cambridge University Press, Cambridge, United Kingdom and New York, NY, USA.

[5] M.Z. Jacobson, M.A. Delucchi, Providing all global energy with wind, water, and solar power, Part I: Technologies, energy resources, quantities and areas of infrastructure, and materials, Energy Policy, 39 (2011) 16.

[6] K. Solangi, M. Islam, R. Saidur, N. Rahim, H. Fayaz, A review on global solar energy policy, Renewable and sustainable energy reviews, 15 (2011) 2149-2163.

[7] E.H. Sargent, Colloidal quantum dot solar cells, Nat Photon, 6 (2012) 133-135.

[8] N. May, Eco-balance of a Solar Electricity Transmission from North Africa to Europe, in, University of Braunschweig, 2005.

[9] E.P.I. Association, Connecting the Sun: Solar photovoltaics on the road to large-scale grid integration, Online], Sept, (2012).

[10] World energy assessment : energy and the challenge of sustainability / United Nations Development Programme, United Nations Department of Economic and Social Affairs, World Energy Council ; [edited by Jose Goldemberg], United Nations Development Programme, New York, 2000.

[11] M.A. Green, Third generation photovoltaics: solar cells for 2020 and beyond, Physica E: Low-dimensional Systems and Nanostructures, 14 (2002) 65-70.

[12] M.C. Beard, R.J. Ellingson, Multiple exciton generation in semiconductor nanocrystals: Toward efficient solar energy conversion, Laser & Photonics Review, 2 (2008) 377-399.

[13] A. Sabbah, D. Riffe, Femtosecond pump-probe reflectivity study of silicon carrier dynamics, Physical Review B, 66 (2002) 165217.

[14] T. Ichibayashi, S. Tanaka, J. Kanasaki, K. Tanimura, T. Fauster, Ultrafast relaxation of highly excited hot electrons in Si: Roles of the L−X intervalley scattering, Physical Review B, 84 (2011) 235210.

[15] S. Kolodinski, J.H. Werner, T. Wittchen, H.J. Queisser, Quantum Efficiencies Exceeding Unity due to Impact Ionization in Silicon Solar-Cells, Appl. Phys. Lett., 63 (1993) 2405-2407.

[16] M. Wolf, R. Brendel, J.H. Werner, H.J. Queisser, Solar cell efficiency and carrier multiplication in Si[sub 1−x]Ge[sub x] alloys, J. Appl. Phys., 83 (1998) 4213.

[17] A.J. Nozik, Multiple exciton generation in semiconductor quantum dots, Chem. Phys. Lett., 457 (2008) 3-11.

[18] M.C. Hanna, A.J. Nozik, Solar conversion efficiency of photovoltaic and photoelectrolysis cells with carrier multiplication absorbers, J. Appl. Phys., 100 (2006) 074510.

[19] J. Tauc, Electron impact ionization in semiconductors, J. Phys. Chem. Solids, 8 (1959) 219-223.

[20] G. Nabiyouni, R. Sahraei, M. Toghiany, M.H.M. Ara, K. Hedayati, Preparation and characterization of nanostructured ZnS thin films grown on glass and n-type Si substrates using a new chemical bath deposition technique, Rev. Adv. Mater. Sci., 27 (2011) 52-57.

[21] V. Grivickas, A. Galeckas, V. Bikbajevas, J. Linnros, J.A. Tellefsen, Spatially and time-resolved infrared absorption for optical and electrical characterization of indirect band gap semiconductors, Thin Solid Films, 364 (2000) 181-185.

[22] Z.G. Ling, P.K. Ajmera, Measurement of bulk lifetime and surface recombination velocity by infrared absorption due to pulsed optical excitation, J. Appl. Phys., 69 (1991) 519-521.

[23] T. Tanaka, A. Harata, T. Sawada, Subpicosecond surface-restricted carrier and thermal dynamics by transient reflectivity measurements, J. Appl. Phys., 82 (1997) 4033-4038.

[24] J. Linnros, Carrier lifetime measurements using free carrier absorption transients. I. Principle and injection dependence, J. Appl. Phys., 84 (1998) 275-283.

[25] J. Kim, Effect of Free-carrier Absorption on the Carrier Dynamics of Quantum-dot Semiconductor Optical Amplifiers, Journal of the Korean Physical Society, 55 (2009) 512-516.

[26] E. Hecht, Optics, Addison-Wesley, Reading, Mass., 2002.

[27] A.J. Sabbah, D.M. Riffe, Measurement of silicon surface recombination velocity using ultrafast pump-probe reflectivity in the near infrared, J. Appl. Phys., 88 (2000) 6954-6956.

[28] C.M. Li, Z.C. Ying, T. Sjodin, H.L. Dai, Measuring photocarrier diffusivity near a Si(111) surface by reflective two-color transient grating scattering, Appl. Phys. Lett., 66 (1995) 3501-3503.

[29] J. Waldmeyer, A contactless method for determination of carrier lifetime, surface recombination velocity, and diffusion constant in semiconductors, J. Appl. Phys., 63 (1988) 1977-1983.

[30] C.M. Li, T. Sjodin, Z.C. Ying, H.L. Dai, Photoexcited carrier diffusion near a Si(111) surface and in the Si bulk, Appl. Surf. Sci., 104 (1996) 57-60.

[31] V. Bikbajevas, V. Grivickas, J. Linnros, J.A. Tellefsen, Injection-level Dependent Surface Recombination Velocities at the SiO2-Si interface, Phys. Scr., T79 (1999) 5.

[32] W. Kern, The Evolution of Silicon Wafer Cleaning Technology, J. Electrochem. Soc., 137 (1990) 1887-1892.

[33] K.A. Reinhardt, W. Kern, Handbook of Silicon Wafer Cleaning Technology (2nd Edition), William Andrew Inc., Norwich, NY, 2008.

[34] C.P.J. Heimdal, Pulsed Laser Deposition of Zinc Sulfide Thin Films on Silicon, in: Department of Physics Norwegian University of Science and Technology, 2014.

[35] S.M. Sze, Physics of Semiconductor Devices, John Wiley & Sons, 1981.

[36] D.M. Gates, Spectral Distribution of Solar Radiation at the Earth's Surface, Science, 151 (1966) 523-529.

[37] C. Anderson, C. Crowell, Threshold Energies for Electron-Hole Pair Production by Impact Ionization in Semiconductors, Physical Review B, 5 (1972) 2267-2272.

[38] C. Lee, R. Logan, R. Batdorf, J. Kleimack, W. Wiegmann, Ionization Rates of Holes and Electrons in Silicon, Physical Review, 134 (1964) A761-A773.

[39] A. Chynoweth, Ionization Rates for Electrons and Holes in Silicon, Physical Review, 109 (1958) 1537-1540.

[40] W.B. Gauster, Laser-Induced Infrared Absorption in Silicon, J. Appl. Phys., 41 (1970) 3850.

[41] H. Rogne, P.J. Timans, H. Ahmed, Infrared absorption in silicon at elevated temperatures, Appl. Phys. Lett., 69 (1996) 2190.

[42] W. Spitzer, H. Fan, Infrared Absorption in n-Type Silicon, Physical Review, 108 (1957) 268-271.

[43] F.J. Wilkinson, A.J.D. Farmer, J. Geist, The near ultraviolet quantum yield of silicon, J. Appl. Phys., 54 (1983) 1172.

[44] J. Geist, E.F. Zalewski, The quantum yield of silicon in the visible, Appl. Phys. Lett., 35 (1979) 503-505.

[45] K.G. Svantesson, N.G. Nilsson, Determination of the temperature dependence of the free carrier and interband absorption in silicon at 1.06 um, Journal of Physics C-Solid State Physics, 12 (1979) 3837-3842.

[46] V. Grivitskas, M. Willander, J. Vaitkus, The Role of Intercarrier Scattering in Excited Silicon, Solid-State Electron., 27 (1984) 565-572.

[47] M. Rosling, H. Bleichner, P. Jonsson, E. Nordlander, The ambipolar diffusion coefficient in silicon: Dependence on excess-carrier concentration and temperature, J. Appl. Phys., 76 (1994) 2855.

[48] M. Rosling, H. Bleichner, M. Lundqvist, E. Nordlander, A Novel Technique for the Simultaneous Measurement of Ambipolar Carrier Lifetime and Diffusion-Coefficient in Silicon, Solid-State Electron., 35 (1992) 1223-1227.

[49] J. Meitzner, F.G. Moore, B.M. Tillotson, S.D. Kevan, G.L. Richmond, Time-resolved measurement of free carrier absorption, diffusivity, and internal quantum efficiency in silicon, Appl. Phys. Lett., 103 (2013) 092101.

[50] C.M. Horwitz, R.M. Swanson, The Optical (Free-Carrier) Absorption of a Hole-Electron Plasma in Silicon, Solid-State Electron., 23 (1980) 1191-1194.

[51] B.E. Sernelius, Optical Free-Carrier Absorption of an Electron-Hole Plasma in Silicon, Physical Review B, 39 (1989) 10825-10830.

[52] V. Grivickas, An accurate method for determining intrinsic optical absorption in indirect band gap semiconductors, Solid State Commun., 108 (1998) 561-566.

[53] G.J. Willems, H.E. Maes, Analytical model for the out-diffusion of an exponentially decaying impurity profile. Application to nitrogen in silicon, J. Appl. Phys., 73 (1993) 3256.

[54] J. Isenberg, W. Warta, Free carrier absorption in heavily doped silicon layers, Appl. Phys. Lett., 84 (2004) 2265.

[55] R.A. Smith, Semiconductors, 2d ed. ed., Cambridge University Press, Cambridge, New York, 1978.

[56] K.F. Brennan, I.I.J. Haralson, Superlattice and multiquantum well avalanche photodetectors: physics, concepts and performance, Superlattices Microstruct., 28 (2000) 77-104.

[57] F.R.-C. Ban Da-Yan, Xue Jian-Geng, Lu Er-Dong, Xu Shi-Hong, Xu Peng-Shou, Valence Band Offsets of Si/ZnS Polar Interfaces: A Synchrotron Radiation Photoemission Study, Physics, 46 (1997) 1817-1825.

[58] M. Cardona, N.E. Christensen, Band offsets in tetrahedral semiconductors, Journal of Vacuum Science & Technology B, 6 (1988) 1285-1289.

[59] B. Brar, R. Steinhoff, A. Seabaugh, X. Zhou, S. Jiang, W.P. Kirk, Band offset measurement of the ZnS/Si(001) heterojunction, in: M. Melloch, M.A. Reed (Eds.) Compound Semiconductors 1997, Iop Publishing Ltd, Bristol, 1998, pp. 167-170.

[60] C. Maierhofer, S. Kulkarni, M. Alonso, T. Reich, K. Horn, Valence Band Offset in ZnS Layers on Si(111) Grown by Molecular-Beam Epitaxy, Journal of Vacuum Science & Technology B, 9 (1991) 2238-2243.

[61] I. Tapan, M.A. Afrailov, A ZnS–Si hetero-junction photodiode for short wavelength photon detection, Nuclear Instruments and Methods in Physics Research Section A: Accelerators, Spectrometers, Detectors and Associated Equipment, 510 (2003) 92-96.

[62] X. Zhou, S. Jiang, W.P. Kirk, Epitaxial growth of ZnS on bare and arsenic-passivated vicinal Si(100) surfaces, J. Appl. Phys., 82 (1997) 2251-2262.

[63] J. Tersoff, Theory of semiconductor heterojunctions: The role of quantum dipoles, Physical Review B, 30 (1984) 4874-4877.

[64] D.H. Foster, G. Schneider, Band alignment and directional stability in abrupt and polar-compensated Si/ZnS interface calculations, arXiv preprint arXiv:1403.5230, (2014).

[65] G.W. ‘t Hooft, C. van Opdorp, Determination of bulk minority-carrier lifetime and surface/interface recombination velocity from photoluminescence decay of a semi-infinite semiconductor slab, J. Appl. Phys., 60 (1986) 1065-1070.

[66] K. Oldham, Approximations for the x exp x2 erfc x function, Mathematics of Computation, 22 (1968) 454-454.

[67] F.E. Doany, D. Grischkowsky, C.C. Chi, Carrier lifetime versus ion-implantation dose in silicon on sapphire, Appl. Phys. Lett., 50 (1987) 460-462.

[68] H.G. Grimmeiss, E. Janzén, B. Skarstam, Deep sulfur-related centers in silicon, J. Appl. Phys., 51 (1980) 4212-4217.

[69] L.-A. Ledebo, Hole photoionisation cross sections for deep level impurities in silicon, Journal of Physics C: Solid State Physics, 14 (1981) 3279.

[70] P. Hazdra, D.J. Reeve, D. Sands, Origin of the defect states at ZnS/Si interfaces, Applied Physics A, 61 (1995) 637-641.

[71] A.J. Simons, M.H. Tayarani-Najaran, C.B. Thomas, Conductance technique measurements of the density of interface states between ZnS:Mn and p-silicon, J. Appl. Phys., 70 (1991) 4950-4957.

[72] S.C. Baker-Finch, K.R. McIntosh, The Contribution of Planes, Vertices, and Edges to Recombination at Pyramidally Textured Surfaces, Photovoltaics, IEEE Journal of, 1 (2011) 59-65.

[73] S.T. Lee, P. Fellinger, S. Chen, Enhanced and wafer-dependent oxygen diffusion in CZ-Si at 500–700 °C, J. Appl. Phys., 63 (1988) 1924-1927.

[74] J. Bisquert, Theory of the impedance of electron diffusion and recombination in a thin layer, The Journal of Physical Chemistry B, 106 (2002) 325-333.

[75] J. Becker, E. Fretwurst, R. Klanner, Measurements of charge carrier mobilities and drift velocity saturation in bulk silicon of 〈111〉 and 〈100〉 crystal orientation at high electric fields, Solid-State Electron., 56 (2011) 104-110.

[76] C.G. Rodrigues, Influence of the concentration, temperature and electric field intensity on the electron mobility in n-doped zinc sulphide, The European Physical Journal B, 72 (2009) 405-408.

[77] J. Mizsei, Ultra-thin insulator covered silicon: potential barriers and tunnel currents, Solid-State Electron., 46 (2002) 235-241.

[78] F. Xu, M. Vos, J.P. Sullivan, L. Atanasoska, S.G. Anderson, J.H. Weaver, H. Cheng, Band-gap discontinuities for Ge/ZnSe(100) and Si/ZnSe(100): A photoemission study, Physical Review B, 38 (1988) 7832-7835.

[79] J. Massa, G. Buller, A. Walker, J. Simpson, K. Prior, B. Cavenett, Photoluminescence decay measurements of n-and p-type doped ZnSe grown by molecular beam epitaxy, Appl. Phys. Lett., 64 (1994) 589-591.

[80] J.Z. Zheng, J.W. Allen, D.E. Spence, W.E. Sleat, W. Sibbett, Decay time of the blue luminescence in ZnSe at room temperature, Appl. Phys. Lett., 62 (1993) 63-65.

[81] P. O'Brien, J. McAleese, Developing an understanding of the processes controlling the chemical bath deposition of ZnS and CdS, J. Mater. Chem., 8 (1998) 2309-2314.

[82] P. O'Brien, D.J. Otway, D. Smith-Boyle, The importance of ternary complexes in defining basic conditions for the deposition of ZnS by aqueous chemical bath deposition, Thin Solid Films, 361 (2000) 17-21.

[83] K. Yamaguchi, T. Yoshida, D. Lincot, H. Minoura, Mechanistic Study of Chemical Deposition of ZnS Thin Films from Aqueous Solutions Containing Zinc Acetate and Thioacetamide by Comparison with Homogeneous Precipitation, J. Phys. Chem. B, 107 (2002) 387-397.

[84] O.M. Peeters, N.M. Blaton, C.J. De Ranter, Kinetics and mechanisms of the reaction between thioacetamide and lead(II), cadmium(II), and cobalt(II) ions in acetate buffered solution, Journal of the Chemical Society, Perkin Transactions 2, (1978) 23-26.

[85] A. Eshuis, G.R.A. van Elderen, C.A.J. Koning, A descriptive model for the homogeneous precipitation of zinc sulfide from acidic zinc salt solutions, Colloids Surf., A, 151 (1999) 505-512.

[86] A. Goudarzi, G.M. Aval, R. Sahraei, H. Ahmadpoor, Ammonia-free chemical bath deposition of nanocrystalline ZnS thin film buffer layer for solar cells, Thin Solid Films, 516 (2008) 4953-4957.

[87] G.H. Bogush, C.F. Zukoski Iv, Studies of the kinetics of the precipitation of uniform silica particles through the hydrolysis and condensation of silicon alkoxides, J. Colloid Interface Sci., 142 (1991) 1-18.

[88] G.H. Bogush, C.F. Zukoski Iv, Uniform silica particle precipitation: An aggregative growth model, J. Colloid Interface Sci., 142 (1991) 19-34.

[89] G.L. Agawane, S.W. Shin, A.V. Moholkar, K.V. Gurav, J.H. Yun, J.Y. Lee, J.H. Kim, Non-toxic complexing agent Tri-sodium citrate's effect on chemical bath deposited ZnS thin films and its growth mechanism, J. Alloys Compd., 535 (2012) 53-61.

[90] A. Bayer, D.S. Boyle, P. O'Brien, In situ kinetic studies of the chemical bath deposition of zinc sulfide from acidic solutions, J. Mater. Chem., 12 (2002) 2940-2944.

[91] Y.J. Chabal, G.S. Higashi, R.J. Small, Surface Chemical Composition and Morphology, in: K. A. Reinhardt, W. Kern (Eds.), Handbook of Silicon Wafer Cleaning Technology, 2nd edition, William Andrew Publishing, Norwich, NY, 2008, pp. 523-618.

[92] H.E. Swanson, R.K. Fuyat, Standard x-ray diffraction powder patterns, National Bureau of Standards, [Washington, DC], 1953.

[93] B.J. Skinner, P.B. Barton Jr., The Substitution of Oxygen for Sulfur in Wurtzite and Sphalerite, Am. Mineral., 45 (1960) 612-625.

[94] A. Bondi, van der Waals Volumes and Radii, J. Phys. Chem., 68 (1964) 441-451.

[95] L. Vegard, Die Konstitution der Mischkristalle und die Raumfüllung der Atome, Zeitschrift für Physik, 5 (1921) 17-26.

[96] B. Palosz, E. Grzanka, S. Gierlotka, S. Stel'makh, R. Pielaszek, W. Lojkowski, U. Bismayer, J. Neuefeind, H.P. Weber, W. Palosz, Application of X-ray Powder Diffraction to Nano-materials - Determination of the Atomic Structure of Nanocrystals with Relaxed and Strained Surfaces, Phase Transitions, 76 (2003) 171-185.

[97] S.M. Salim, A.H. Eid, A.M. Salem, H.M. Abou El-khair, Nanocrystalline ZnS thin films by chemical bath deposition method and its characterization, Surf. Interface Anal., 44 (2012) 1214-1218.

[98] H. Pulker, J. Maser, The origin of mechanical stress in vacuum-deposited MgF2 and ZnS films, Thin Solid Films, 59 (1979) 65-76.

[99] J.A. Ruffner, M.D. Himel, V. Mizrahi, G.L. Stegeman, U.J. Gibson, Effects of low substrate temperature and ion assisted deposition on composition, optical properties, and stress of ZnS thin films, Appl. Opt., 28 (1989) 5209-5214.

[100] F.A. Doljack, The Origins of Stress in Thin Nickel Films. AEC Technical Rep. No. 76, Case Western Reserve University, Cleveland, OH, 1971.

[101] S. Gorer, G. Hodes, Quantum size effects in the study of chemical solution deposition mechanisms of semiconductor films, J. Phys. Chem., 98 (1994) 5338-5346.

[102] S.W. Glunz, D. Biro, S. Rein, W. Warta, Field-effect passivation of the SiO2Si interface, J. Appl. Phys., 86 (1999) 683-691.

[103] F.-J. Ma, B. Hoex, G.S. Samudra, A.G. Aberle, Modelling and Simulation of Field-effect Surface Passivation of Crystalline Silicon-based Solar Cells, Energy Procedia, 15 (2012) 155-161.

[104] W. Olthuis, P. Bergveld, On the charge storage and decay mechanism in silicon dioxide electrets, Electrical Insulation, IEEE Transactions on, 27 (1992) 691-697.

[105] E.H. Nicollian, C.N. Berglund, P.F. Schmidt, J.M. Andrews, Electrochemical Charging of Thermal SiO2 Films by Injected Electron Currents, J. Appl. Phys., 42 (1971) 5654-5664.

[106] E.M. Moreno, M. Kunst, The influence of the silicon/silicon oxide space charge region on excess charge carrier kinetics in silicon, physica status solidi (b), 248 (2011) 352-360.

[107] S.D. Brotherton, M.J. King, G.J. Parker, The electrical properties of sulphur in silicon, J. Appl. Phys., 52 (1981) 4649-4658.